

ADDRESSING PROTECTION CHALLENGES IN ELECTRIC POWER GRIDS
WITH DISTRIBUTED GENERATION: A FOCUS ON DIRECTIONAL
OVERCURRENT RELAYS

by

Oluwatimilehin Damilare Adeosun

A dissertation submitted to the faculty of
The University of North Carolina at Charlotte
in partial fulfillment of the requirements
for the degree of Doctor of Philosophy in
Electrical Engineering

Charlotte

2024

Approved by:

Dr. Valentina Cecchi

Dr. Madhav Manjrekar

Dr. Linqun Bai

Dr. Ian Marriott

ABSTRACT

OLUWATIMILEHIN DAMILARE ADEOSUN. Addressing Protection Challenges in Electric Power Grids with Distributed Generation: A Focus on Directional Overcurrent Relays. (Under the direction of DR. VALENTINA CECCHI)

The dissertation explores the challenges and transformations in modernizing the electrical grid, characterized by increased electric power grid interconnectivity, the widespread integration of Distributed Generation (DG), and frequent network reconfigurations. These transformations pose significant challenges to traditional grid technologies and operations, including power quality issues, protection scheme challenges, and complications in energy market dynamics. This study delves into the challenges of power system protection schemes from two perspectives: the misoperation of directional elements and the miscoordination of directional overcurrent elements. The proper operation of the protection system is critical to ensuring grid reliability.

The first perspective investigates the misoperation of directional elements; we model and analyze the fault behaviors of various generators, including Synchronous and Inverter-Based Generators (IBDGs) with differing control architecture, to comprehensively understand their fault characteristics. Furthermore, we explore the misoperation of negative sequence directional elements, proposing and validating a prevention strategy using Real-Time Hardware-in-the-Loop (RT-HIL) setups.

The second perspective addresses the coordination issues of Directional Overcurrent Relays (DOCRs) and aims to minimize their operating times. The dissertation illustrates the advantages of employing optimization algorithms over numerical iteration methods for relay coordination. It examines the coordination performance using Genetic Algorithms (GA) and Particle Swarm Optimization (PSO), presenting an enhanced variation of PSO that yields improved performance validated through virtual HIL setups.

Additionally, the dissertation investigates the issue of DOCR miscoordination due

to variations in fault current during fault isolation. It introduces a dynamic Time-Current Characteristic (TCC) formulation adapted to these variations, validated using IEEE test systems. It also investigates DG instability and miscoordination stemming from changes in network topology and generation short circuit capacity. A prevention strategy that combines clustering and optimization algorithms is proposed and validated. Moreover, a co-optimization strategy is presented and validated to prevent DOCR miscoordination while maintaining DG stability, ensuring that the Critical Clearing Time (CCT) associated with a fault is greater than the operating time of the relays assigned to isolate the fault.

This work significantly advances the understanding of how grid modernization impacts power system protection and lays the groundwork for future research in this evolving field. It highlights the need for a collaborative approach between inverter manufacturers and protection engineers to facilitate a seamless and reliable grid transformation.

DEDICATION

This dissertation is dedicated to Almighty God, my source of wisdom and strength, who has guided me through this journey with grace. To my parents, whose love, sacrifice, and belief in me have shaped who I am, and to my siblings, Sefunmi and Tolu, whose support has been a source of encouragement. Your collective belief in me has turned dreams into reality.

ACKNOWLEDGEMENTS

Drawing inspiration from the African Proverb, "We stand tall because we stand on the backs of those who lifted us."

I commence this acknowledgment with a heart full of gratitude. This journey to completing my Ph.D. has been a testament to the strength and support I've received from a constellation of remarkable individuals who have lifted and guided me through the rigors and triumphs of academic pursuit.

First and foremost, my deepest appreciation is extended to my supervisor, Dr. Valentina Cecchi, whose unwavering support, insightful guidance, and understanding have been the cornerstone of my Ph.D. journey. Your mentorship has shaped my academic endeavors and profoundly influenced my professional development. I am also immensely thankful to my committee members, Dr. Madhav Manjrekar, Dr. Linqua Bai, and Dr. Ian Marriott, for their contributions, advice, and time.

My special gratitude goes to my late friend Andrew Amuna, with whom I've had insightful discussions that significantly influenced my research direction.

To my colleagues and friends I made during these doctoral years - Tumininu Mbanisi, Abhijith Ravi, Raheem Ariwoola, Sumit Kumar, Mariann Thomas, Kiran Ravikumar, Sagar Kanade, Sathish Kumar, Muhammad Foyazur, Akintunde Abass, Olalekan Ogundairo, Michael Uduebor, Cory Brown, Idrissa Alassane, and Khadijah Green; I am grateful for your contributions, support, and memorable moments we've shared. Your presence has added immeasurable value to my experience.

My heartfelt thanks to my esteemed confidante, Valerie Anne, and my dear friends Oluchi Oba, Adebola Olowookere, Kolawole Segun, Ayodeji Babajide, Francis Adereti, and Adepoju Michael for your unwavering support, inspiration, and companionship. You have brightened my days and bolstered my spirit through the most challenging times; your listening ear to my jargon was not in vain.

I extend my appreciation to the UNCC Graduate School and the UNCC Energy

Production and Infrastructure Center for their financial support of my work. Your backing has been instrumental in my research and academic development.

Lastly, but most importantly, I deeply thank my Dad, Mum, Sefunmi, Tolulope, and my extended family. Your love, encouragement, and belief in me have been my guiding light. This achievement is not mine alone; it belongs to all of you.

I am eternally grateful to everyone who has been a part of this journey. Thank you for lifting me higher and helping me stand tall.

TABLE OF CONTENTS

LIST OF TABLES	xii
LIST OF FIGURES	xv
LIST OF ABBREVIATIONS	xx
CHAPTER 1: INTRODUCTION	1
1.1. Overview and Motivation	1
1.2. Main Contribution of this Dissertation	3
1.3. Dissertation Outline	4
CHAPTER 2: BACKGROUND AND LITERATURE REVIEW	6
2.1. A Survey of Impact of Distributed Generations	6
2.1.1. Benefit of Decentralizing the Grid	7
2.1.2. Challenges of Decentralizing the Grid	8
2.2. Overview of Power System Protection	16
2.2.1. Power System Protection Sequence of Event	17
2.2.2. Power System Protection Principle	18
2.2.3. Power System Protection Performance Metrics	19
CHAPTER 3: FAULT CHARACTERISTICS OF INVERTER BASED GENERATORS	21
3.1. Main Contribution	22
3.2. Fault Characteristics of Synchronous Generator	23
3.3. Fault Characteristics of Double Fed Induction Generators (DFIG)	24

3.4. Fault Characteristics of Full-Scale Converters (FSC) Genertors	28
3.4.1. Coupled Sequence Control (CSC) Architecture	30
3.4.2. Decoupled Positive Sequence Control (DPSC) Architecture	30
3.4.3. Decoupled Positive and Negative Sequence Control (DPNSC) Architecture	32
3.4.4. Modified-Decoupled Positive and Negative Sequence Control (M-DPNSC) Architecture	33
3.5. Summary of Investigation and Future Direction	36
CHAPTER 4: NEGATIVE SEQUENCE VOLTAGE POLARISED (NSVP) DIRECTIONAL SCHEME MIS-OPERATION IN THE PRESENCE OF IBDG: INSIGHTS AND PREVENTION	39
4.1. Main Contribution	42
4.2. Problem Formulation: Misoperation of NSVP Directional Element in the Presence of IBDG	42
4.3. Simulation Setup and Case study	45
4.3.1. Virtual Setup	45
4.3.2. HIL Setup	47
4.3.3. Description of Test System	48
4.4. Results and Analysis	49
4.4.1. Virtual Simulation: NSVP Misoperation	50
4.4.2. HIL Simulation: NSVP Misoperation	52
4.4.3. NSVP prevention Approach (Virtual and HIL Simulation)	57
4.5. Conclusion	59

CHAPTER 5: ENHANCED PROTECTION COORDINATION APPROACH: A COMPARATIVE ANALYSIS	61
5.1. Main Contribution	61
5.2. Overview and Methodology	62
5.2.1. Protection Coordination Formulation	62
5.2.2. Numerical Iteration Method	64
5.2.3. Optimization Algorithms	67
5.3. Result and Analysis	71
5.3.1. Description of Test System	71
5.3.2. Result and Analysis for 9-Bus System	74
5.3.3. Result and Analysis for the IEEE 33-Bus System	77
5.4. Conclusion	79
CHAPTER 6: ADDRESSING OVERCURRENT RELAY MISCOORDINATION CAUSED BY CHANGES IN FAULT CURRENT DURING FAULT ISOLATION	81
6.1. Main Contribution	81
6.2. Problem Statement and Formulation	83
6.3. Proposed Dynamic Formulation	84
6.4. Case Study and Simulation Results	88
6.4.1. Description of Test System	89
6.4.2. IEEE 8-Bus: Coordination Simulation Results and Analysis	94
6.4.3. IEEE 33-Bus Coordination Simulation Results and Analysis	96
6.5. Conclusion and Future Work	98

CHAPTER 7: A ROBUST DIRECTIONAL OVERCURRENT RELAY COORDINATION STRATEGY: IMMUNE TO NETWORK OP- ERATION AND TOPOLOGY RECONFIGURATION, ENSURING DISTRIBUTED GENERATION STABILITY	100
7.1. Main Contribution	100
7.2. Stability of Distributed Generator	101
7.2.1. Solution Approach to Prevent Generator Instability	103
7.3. Network Topology and Operational Changes	104
7.3.1. Solution Approach to Prevent Miscoordination due to Changes in Network Topology and Operational Changes	104
7.4. Case Study and Simulation Results	108
7.4.1. Description of Test System	108
7.4.2. Stability of Distributed Generator	111
7.4.3. Network Topology and Operational Changes	115
7.5. Conclusion and Future Work	121
CHAPTER 8: CONCLUSIONS AND RECOMMENDATIONS	123
8.1. Overview	123
8.2. Summary of Research Contributions	123
8.3. Recommendations and Future Directions	125
REFERENCES	127
APPENDIX A: Chapter 5 Data and Results	138
APPENDIX B: Chapter 6 Data and Results	148
APPENDIX C: Chapter 7 Data and Results	156

LIST OF TABLES

TABLE 3.1: SG Scenario: Magnitude of the Fault Current and Voltage Sequence Component	25
TABLE 3.2: DFIG Scenario: Magnitude of the Fault Current and Voltage Sequence Component	28
TABLE 3.3: FSC-CSC Scenario: Magnitude of the Fault Current and Voltage Sequence Component	31
TABLE 3.4: FSC-DPNSC Scenario: Magnitude of the Fault Current and Voltage Sequence Component	34
TABLE 3.5: FSC-M-DPNSC Scenario: Magnitude of the Fault Current and Voltage Sequence Component	36
TABLE 5.1: IEC Inverse-Time Current Curve (TCC) Equation Parameters	63
TABLE 5.2: U.S. Inverse-Time Current Curve (TCC) equation parameters	63
TABLE 5.3: 9-Bus System: Relay Coordination Pairs and Fault Current Characteristics	73
TABLE 5.4: IEEE-33-Bus System: Relay Coordination Pairs and Fault Current Characteristics	75
TABLE 5.5: 9-Bus System: Performance Summary of the Numerical Iteration, GA, CIW-PSO Variation	76
TABLE 5.6: 9-Bus System: Performance Summary of the CIW-PSO, LIW-PSO, and EIW-PSO variation	77
TABLE 5.7: IEEE 33-Bus System: Performance Summary of the Numerical Iteration, GA, CIW-PSO Variation	78
TABLE 5.8: IEEE 33-Bus System: Performance Summary of the CIW-PSO, LIW-PSO, and EIW-PSO Variation	78
TABLE 6.1: IEEE 8-Bus System: Relay Coordination Pairs	90

TABLE 6.2: Modified IEEE 33-Bus System: Relay Coordination Pairs	92
TABLE 6.3: IEEE 8-bus System: Fault Current Considering Adjacent Breaker Status	93
TABLE 6.4: IEEE 8-bus System: Coordination Time Interval	94
TABLE 6.5: IEEE 8-Bus System: Summary of Total Operating Time and Coordination Time Interval (CTI)	95
TABLE 6.6: Modified IEEE 33-bus system: Summary of Total Operating Time and Coordination Time Interval (CTI)	96
TABLE 7.1: IEEE 14-bus system: Network Operation and Topology Configuration Cases	110
TABLE 7.2: Modified IEEE 33-bus System: Network Operation and Topology Configuration Cases	110
TABLE 7.3: Modified IEEE 33-Bus System: Critical Clearing Time and Relay Operating Time (Without CCT Constraint)	112
TABLE 7.4: IEEE 33-Bus System: Relay Operating Time Considering CCT Constraint	114
TABLE 7.5: Summary of Clustering Performance	116
TABLE 7.6: Modified IEEE 14-Bus System: Overview of the Coordination Time Interval Violations in Cases across Setting Groups	119
TABLE 7.7: Modified IEEE 33-Bus System: Overview of the Coordination Time Interval Violations in Cases across Setting Groups	120
TABLE 7.8: Total Operating Time of each Clustering Approach	120
TABLE A.1: 9-Bus System: Nominal Current	138
TABLE A.2: 9-Bus System: Relay Settings (Time Dial Setting (TDS) and Pickup (I_p)) obtained from Numerical Iteration, GA, and CIW-PSO	138
TABLE A.3: 9-Bus System: Relay Settings (Time Dial Setting (TDS) and Pickup (I_p)) obtained from LIW-PSO and EIW-PSO (9-Bus System)	139

TABLE A.4: 9-Bus System: Relay Operating Time and CTI obtained from Numerical Iteration Approach	140
TABLE A.5: 9-Bus System: Relay Operating Time and CTI obtained from Genetic Algorithm and CIW-PSO	142
TABLE A.6: IEEE-33-Bus System: Nominal Current	143
TABLE A.7: IEEE 33-Bus System: Relay Settings (Time Dial Setting (TDS) and Pickup (I_p)) obtained from CIW-PSO, LIW-PSO, and EIW-PSO	144
TABLE A.8: IEEE 33-Bus System: Relay Operating Time and CTI obtained from Numerical Iteration Approach	145
TABLE A.9: IEEE 33-Bus System: Relay Operating Time and CTI obtained from Genetic Algorithm (GA) and CIW-PSO	146
TABLE A.10: IEEE 33-Bus System: Relay Operating Time and CTI obtained from LIW-PSO and EIW-PSO	147
TABLE B.1: IEEE 8-Bus System: Relay Operating Time from the Three Formulation Approach	148
TABLE B.2: Modified IEEE 33-Bus Relay: Fault Current Characteristics Considering Adjacent Breaker Status	149
TABLE B.3: Modified IEEE 33-Bus Relay: Coordination Time Interval from the Three Formulation Approach	152
TABLE B.4: Modified IEEE 33-Bus Relay: Relay Operating Time from the Three Formulation Approach	155
TABLE C.1: IEEE 14-bus system: Total Operating Time of Each Clustering Approach	156
TABLE C.2: IEEE 33-bus system: Total Operating Time of Each Clustering	158

LIST OF FIGURES

FIGURE 2.1: A Simple radial single line drawing	11
FIGURE 2.2: A Simple circuit illustrating the underreach of distance element	13
FIGURE 2.3: Western interconnection misoperation between 2016 and 2022 [1]	16
FIGURE 3.1: 33kV Test System	22
FIGURE 3.2: SG scenario: Phasor representation of the fault current and voltage sequence component (a) ABC-G Fault (b) AB-G Fault (c) A-G Fault	24
FIGURE 3.3: Block diagram of a DFIG showing the control blocks	26
FIGURE 3.4: DFIG Scenario: Phasor representation of the fault current and voltage sequence component (a) ABC-G Fault (b) AB-G Fault (c) A-G Fault	28
FIGURE 3.5: A simplified block diagram for an FSC-based generator	29
FIGURE 3.6: A simplified block diagram of the CSC section of a GSC	30
FIGURE 3.7: FSC-CSC Scenario: Phasor representation of the fault current and voltage sequence component (a) ABC-G Fault (b) AB-G Fault (c) A-G Fault	31
FIGURE 3.8: A simplified block diagram of the DPSC section of the GSC architecture	32
FIGURE 3.9: Phasor representation of the fault current and voltage sequence component for FSC with DPSC architecture (a): ABC-G Fault, (b): AB-G Fault, (c) A-G Fault	32
FIGURE 3.10: A simplified block diagram of the DPNSC section of the GSC architecture	33
FIGURE 3.11: FSC-DPNSC Scenario: Phasor representation of the fault current and voltage sequence component (a) ABC-G Fault (b) AB-G Fault (c) A-G Fault	34

FIGURE 3.12: Plot of the relationship between POI voltage and current negative sequence component	35
FIGURE 3.13: Implementation of German grid code in the GSC control [2]	35
FIGURE 3.14: FSC-M-DPNSC Scenario: Phasor representation of the fault current and voltage sequence component (a) ABC-G Fault (b) AB-G Fault (c) A-G Fault	36
FIGURE 4.1: Forward direction SLG fault: Negative sequence component	44
FIGURE 4.2: Reverse direction SLG fault: Negative sequence component	45
FIGURE 4.3: A flow chart of the NSVP directional element logic	46
FIGURE 4.4: Block diagram of the enable logic (32QE)	46
FIGURE 4.5: Block diagram of the fault direction determination	47
FIGURE 4.6: A simplified representation of the HIL real-time setup	47
FIGURE 4.7: Modified IEEE 13-bus system	48
FIGURE 4.8: A simplified block diagram of IBDG grid side control	49
FIGURE 4.9: Detailed diagram of the inverter control block	50
FIGURE 4.10: Dynamic volt-var curve	50
FIGURE 4.11: Virtual simulation SCADA interface for an SDG scenario: Normal operating condition	51
FIGURE 4.12: Virtual simulation SCADA interface for an SDG Scenario: (a) Forward fault condition, (b) Reverse fault condition	51
FIGURE 4.13: Virtual simulation SCADA Interface for an IBDG Scenario: (a) Forward fault condition, (b) Reverse fault condition	52
FIGURE 4.14: Front panel display: Forward directional element setting during forward fault - SDG scenario	53
FIGURE 4.15: Event record display: Forward directional element setting during forward fault - SDG scenario	53

FIGURE 4.16: Front panel display: Reverse directional element setting during forward fault - SDG scenario	53
FIGURE 4.17: Event record display: Reverse directional element setting during forward fault - SDG scenario	54
FIGURE 4.18: Front panel display: Reverse directional element setting during reverse fault - SDG scenario	54
FIGURE 4.19: Event record display: Reverse directional element setting during reverse fault - SDG scenario	55
FIGURE 4.20: Front panel display: Forward directional element setting during reverse fault - SDG scenario	55
FIGURE 4.21: Event record display: Forward directional element setting during reverse fault - SDG scenario	55
FIGURE 4.22: Front panel display: Reverse directional element setting during reverse fault - IBDG scenario	56
FIGURE 4.23: Event record display: Reverse directional element setting during reverse fault - IBDG scenario	56
FIGURE 4.24: prevention approach validation: Virtual simulation SCADA interface for an IBDG scenario: (a) Forward fault condition, (b) Reverse fault condition	58
FIGURE 4.25: prevention approach validation: Event record display for forward directional element setting during forward fault - IBDG scenario	59
FIGURE 4.26: prevention approach validation: Event record display for reverse directional element setting during reverse fault - IBDG scenario	59
FIGURE 5.1: A flowchart of genetic algorithm	68
FIGURE 5.2: A flowchart of particle swarm optimization	69
FIGURE 5.3: Plot of three variations of inertia weight	71
FIGURE 5.4: 9-bus system: A single line diagram	72

FIGURE 5.5: Modified IEEE 33-bus system: A single line diagram	74
FIGURE 5.6: Simulation of the fault Isolation by the branch primary protection relays	79
FIGURE 5.7: 9-bus system: Total operating time of the optimization approaches for 25 executions	80
FIGURE 5.8: Modified IEEE 33-bus system: Total operating time of the optimization approaches for 25 executions	80
FIGURE 6.1: A simple mesh network showing ZOP and relays	84
FIGURE 6.2: Two levels of fault current during fault isolation	84
FIGURE 6.3: Overcurrent TCC for R1 and R2 showing CTI changes during fault isolation	84
FIGURE 6.4: IEEE 8-bus system: Single line diagram	90
FIGURE 6.5: Modified IEEE 33-bus system: Single line diagram	91
FIGURE 6.6: IEEE 8-bus system: Statistics of the total operating time from each formulation approach across 23 executions	96
FIGURE 6.7: Modified IEEE 33-Bus System: Statistics of the total operating time from each formulation approach across 23 executions	98
FIGURE 7.1: A simplified equivalent circuit of a synchronous machine	102
FIGURE 7.2: Modified IEEE 14-bus system: Single line diagram	109
FIGURE 7.3: Statistics of the CCT violation of the four scenarios across 23 executions	113
FIGURE 7.4: DG1 instability due to CCT violation (Before implementing CCT constraint in relay coordination)	114
FIGURE 7.5: Stable DG1 after relay operation (After implementing CCT constraint in relay coordination)	115
FIGURE 7.6: IEEE 14-bus Clustering Result: (a) Clustering Approach 1 (b) Clustering Approach 2 and (c) Clustering Approach 3	116

FIGURE 7.7: IEEE 33-bus Clustering Result: (a) Clustering Approach 1 (b) Clustering Approach 2 and (c) Clustering Approach 3	117
FIGURE 7.8: Modified IEEE 14-bus system: Total operating time of the three clustering approach considering 25 executions	121
FIGURE 7.9: Modified IEEE 33-bus system: Total operating time of the three clustering approach considering 25 executions	121

LIST OF ABBREVIATIONS

ABCG Phase A, B and C to Ground Fault

AG Phase A to Ground Fault

BCG Phase B and C to Ground Fault

CCT Critical Clearing Time

CIW Constant Inertia Weight

CSC Coupled Sequence Control

CTI Coordination Time Interval

DER Distributed Energy Resources

DFIG Doubly Fed Induction Generator

DG Distributed Generator

DOCR Directional Overcurrent Relay

DPNSC Decoupled Positive and Negative Sequence Control

DPSC Decoupled Positive Sequence Control

DSC Decoupled Sequence Control

DUT Device Under Test

EIW Exponential Inertia Weight

FSC Full-Scale Converters

GA Generic Algorithm

IBDG Inverter Based Distributed Generator

LIW Linear Inertia Weight

LVRT Low Voltage Ride Through

MTA Minimum Torque Angle

NSVP Negative Sequence Voltage Polarized

PCC Point of Common Coupling

PSO Particle Swarm Optimization

PSVP Positive Sequence Voltage Polarized

RT-HIL Real-Time Hardware In the Loop

SAIDI System Average Interruption Duration Index

SDG Synchronous Distributed Generator

SG Setting Group

SLG Single Line to Ground

TCC Time Current Curve

TDS Time Dial Setting

WTG Wind Turbine Generator

ZOP Zone of Protection

CHAPTER 1: INTRODUCTION

1.1 Overview and Motivation

In recent decades, the world has experienced a considerable increase in reliance on electrical energy. According to the U.S. Energy Information Administration (EIA) 2022 report [3], despite advancements in energy efficiency technology, energy consumption has surged by a factor of 14 between 1950 and 2022. This trend is anticipated to persist due to increased electrification, high population growth, increased regional manufacturing, and elevated living standards. These factors are driving energy consumption growth, surpassing advancements in energy efficiency. The impact of heightened energy consumption on greenhouse gas emissions is prompting two transformations to the traditional grid; the first is the shift from current carbon-emitting generation units to cleaner generating sources, while the second is decentralizing the grid for improved resilience and reliability. These two transformations require adequate grid modernization to meet future energy demands. According to McKinsey & Company [4], despite the increase in investment to modernize the grid, the System Average Interruption Duration Index (SAIDI) did not improve over the years. The primary reason is the increased frequency of extreme weather conditions and the demand for electric energy.

One of the strategies to improve SAIDI involves decentralizing the conventional grid and transitioning it into a network of microgrids. This consists of integrating clean energy resources, introducing distributed energy resources, and enhancing automation and control. However, integrating clean energy sources and distributed generation encounters notable challenges that require changes to energy market operations, electric power system planning, and power quality issues such as voltage instability, frequency

fluctuations, harmonic presence, and flickers and misoperation of traditional protection schemes. Addressing these challenges has become a prominent area of research to ensure the smooth and reliable operation of the grid network.

Electric grids worldwide are swiftly evolving regarding generation resource mix, incorporating larger quantities of renewable generation like wind and solar photovoltaic power plants. Consequently, numerous policies aimed at grid modernization, such as FERC orders 841 and 222, are in place to transform traditional energy markets to accommodate the growing Distributed Energy Resources (DERs). Various standards include FERC orders 661, 845, 842, 827, IEEE 1547, VDE-AR-N 4120, and specific NERC PRC standards provide guidelines to standardize operational and technical requirements, facilitating the connection of DERs to the grid and offering support during voltage or frequency disturbances.

This dissertation delves into the challenges of modernizing the grid, including integrating renewable energy resources, decentralizing generation units, and increasing connectivity, specifically focusing on their impact on traditional protection schemes. Protection scheme malfunctions can be categorized into two areas: protection element misoperation and protection device miscoordination.

1. Protection Element Misoperation:

- Relays failing to operate accurately when necessary during fault conditions.
- Relays operating unnecessarily in non-fault conditions, leading to false tripping.

2. Protection Device Miscoordination:

- Lack of proper coordination between primary and backup protective devices within designated protection zones.

1.2 Main Contribution of this Dissertation

The dissertation's primary contributions encompass investigations and innovative strategies addressing crucial aspects of power system protection in the presence of distributed generators, including Inverter-Based Distributed Generators (IBDGs). These contributions are elucidated through the following critical research endeavors:

1. Investigation of the Impact of IBDG on Protection Schemes: We investigate the effect of IBDGs on existing protection schemes within the electrical power system. The analysis focused on understanding the fault characteristics of different generator types.
2. A Strategy to Prevent the Misoperation of Negative Sequence Directional Element in the Presence of IBDG: We demonstrate the misoperation of negative sequence directional element in the presence of IBDG and offer a strategy to prevent the identified misoperation. The aim is to ensure that IBDG does not negatively impact the negative sequence of the voltage-polarized element.
3. An Analysis of the Benefit of Optimization Algorithms over Numerical Iteration in Relay Coordination: We highlight the benefits and superiority of utilizing optimization algorithms, such as metaheuristic techniques like Particle Swarm Optimization (PSO), in coordinating protective relays compared to numerical iteration approach. This demonstration clarifies how optimization algorithms enhance the efficiency and effectiveness of relay coordination.
4. A Novel Dynamic Relay Coordination Formulation and Approach to Prevent Miscoordination Caused by Transient Changes in Fault Current during Fault Isolation: We demonstrated the miscoordination of overcurrent protection devices caused by a temporary and transient change in fault current during fault isolation, and our proposed solution is a dynamic coordination formulation.

The aim is to create a formulation that allows relays to adapt dynamically to transient changes in fault current during fault isolation.

5. A Coordination Approach to Prevent Network Operational and Topological Changes: We devise a coordination strategy to address the impacts of operational and topological alterations within the grid network. This strategy established an approach for relays to maintain effective coordination amid network operation and topology changes.

1.3 Dissertation Outline

The chapter outline of the specific areas of study and contributions within this dissertation is organized as follows:

Chapter 2 comprehensively reviews existing literature on Distributed Generators (DG) and power system protection, the main areas explored in this dissertation. Relevant research findings are presented to provide an understanding of the current knowledge in these areas.

Chapter 3 delves into the effects of IBDG on existing protection schemes within the electrical power system. The analysis focuses on understanding the fault characteristics of different generator types, aiming to identify and comprehend how IBDGs influence protective schemes.

Chapter 4 demonstrates the misoperation of the negative sequence directional element in the presence of IBDG and proposes a strategy to prevent the misoperation. The primary objective is to ensure that IBDGs do not adversely affect the functionality of the protective scheme's negative sequence voltage-polarized element.

Chapter 5 shows the advantages of employing optimization algorithms instead of numerical iteration approaches in coordinating protective relays. It specifically focuses on metaheuristic techniques like Particle Swarm Optimization (PSO) and Genetic Algorithm (GA), emphasizing how optimization algorithms enhance the effi-

ciency and effectiveness of relay coordination.

Chapter 6 demonstrates miscoordination issues with overcurrent protection devices caused by temporary and transient changes in fault current during fault isolation. It introduces a dynamic formulation approach designed to address and prevent coordination violations. It ensures optimal protection coordination and immunity to transient changes during fault isolation in a mesh network.

Chapter 7 demonstrates the miscoordination of overcurrent protection schemes caused by operational and topological changes. It presents a coordination strategy to ensure optimal relay coordination immune to network topology changes and changes in the short circuit capacity of fault-generating sources.

In Chapter 8, the dissertation concludes by summarizing its main contributions, reviewing critical findings, and presenting potential avenues for future research.

CHAPTER 2: BACKGROUND AND LITERATURE REVIEW

This chapter offers a technical background emphasizing the two key areas addressed within this dissertation: distribution generation and power system protection.

2.1 A Survey of Impact of Distributed Generations

The traditional grid exhibits a radial and centralized structure, with power generation located remotely from the loads. It is imperative to acknowledge the escalating frequency of extreme weather events in recent years, which frequently disrupts electric power supply, resulting in considerable hardships and, regrettably, fatalities [5, 6]. In addition, heightened political and social awareness regarding the imperative to diminish carbon footprints and achieve net-zero electricity, driven by global warming concerns, has prompted a shift toward adopting distributed generation. The decentralization of the grid is a strategy to prevent global warming and address power outages during extreme weather conditions. This approach concurrently serves dual purposes: it curtails the emission of greenhouse gases by fostering the adoption of clean energy resources and improves grid resilience through integrating distributed generators [7, 8].

In summary, the decentralization of the grid emerges as a pivotal aspect of the energy transition, promising to bolster resiliency, efficiency, and sustainability. Consequently, substantial investments have been directed towards grid decentralization, with projections estimating a staggering \$3 trillion expenditure by the United States over the next two decades [9, 10].

2.1.1 Benefit of Decentralizing the Grid

- **Decarbonized Grid:** Unlike the traditional large rotating generators that emit pollutants and greenhouse gases, clean Inverter-Based Distributed Generators (IBDG) offer greater flexibility, and decentralization enables the seamless integration of a diverse array of clean, renewable sources such as solar PV, wind, and biomass into the grid [11, 9, 10].
- **Enhanced Resilience and Reliability:** As highlighted in [12, 13, 14], the decentralization approach reduces outages during extreme weather conditions, disasters, or cyber-attacks by establishing microgrids capable of island operation during disruptions. This reduces the vulnerability inherent in a traditional centralized grid.
- **Ancillary Services:** Distributed Energy Resources (DERs) can fulfill various ancillary service functions, including frequency regulation, reactive power/voltage control, active loss balancing, and demand response services [15, 16, 17].
- **Minimized Transmission Losses:** In a decentralized system, the generation units are situated close to the loads, resulting in reduced transmission distance compared to the conventional centralized grid. Numerous studies have demonstrated the enhancement of line loss and voltage profiles in decentralized systems [18, 19, 20]. The authors illustrated the reduction of line losses on North American distribution feeders by introducing Distributed Generators (DGs) in [18]. However, It is worth noting that power loss in the network exhibits a parabolic relationship with DG size, reaching a minimum before increasing with further size increments [21, 22].

2.1.2 Challenges of Decentralizing the Grid

Despite the advantage of the decentralized grid, it comes with notable challenges because of its complexity. The decentralization of the grid increases its interconnectivity and causes a bi-directional power flow. Below are some challenges and solution approaches:

- **Power Quality Issue:** Power quality challenges emerge when different types of distributed generators' are integrated into the distribution network. The main concerns encompass voltage deviations, voltage flicker, and harmonics, with the primary power quality issues stemming from inverter-based sources.
 - **Grid Stability:** While a Synchronous Generator (SG) has a comparatively milder impact on grid stability because of its rotating mass, the increasing penetration of IBDGs introduces a greater threat due to their low inertial and low damping effects, potentially leading to frequency instability [23, 24, 25, 26, 27]. To address these challenges, various literatures propose the incorporation of virtual inertial systems to emulate synchronous generators and the implementation of damping control concepts [25, 26, 27, 28, 29, 30]. It's crucial to note that optimizing damping parameters based on aggregated systems might not yield identical stability performance when applied to the complete power grid, as outlined in [29]. Consequently, it becomes imperative to consider the full system dynamics when devising control strategies for frequency stability in low-inertia systems.
 - **Harmonic Distortion and Voltage Deviations:** These include overvoltage, undervoltage, and frequency distortions. A solution lies in effectively addressing these complex problems through strategic siting and sizing of DG. While DGs seldom cause over-voltage, precautions must also be taken to prevent under-voltage situations when disconnecting DGs. Optimization

approaches, detailed in [31, 32, 33, 21, 22, 34], have been employed to effectively prevent harmonic distortions and voltage deviation issues, optimizing DG siting, sizing, and filter configurations.

- **Changes to Traditional Electric Market:** In conventional markets, actual generation quantities are known, with the load being the only uncertain factor requiring forecasting. However, the proliferation of IBDGs has reshaped the traditional electricity market dynamics, introducing increased pricing dynamism to account for uncertainties and intermittencies associated with these DGs [35, 36]. Discussions in [37, 38] delve into pricing models considering the uncertainties and intermittencies of solar and wind generating systems. Additionally, they present contract and pricing models that incorporate the utilization of DGs for ancillary services, such as frequency and voltage regulation support.
- **Misoperation of Protection Scheme:** Traditionally, protection schemes were tailored for the conventional grid structure, characterized by centralized synchronous generators. However, the recent appeal for grid decentralization results in bidirectional power flows and an increased fault current magnitude. Additionally, the status of line switches determines the fault magnitude and direction [39, 40, 41, 42] as a result of network reconfiguration in modern grids. The consequence of this DG penetration is the miscoordination of protection devices and the misoperation of protection elements, leading to issues such as sympathetic tripping, blinding of protection elements, and nuisance tripping [43, 44, 45, 46, 47, 48]. The miscoordination of protection devices in the presence of DG is discussed by authors [49, 50, 51, 52].

A common remedy for misoperation involves disconnecting the DG during a fault to maintain traditional fault characteristics familiar to conventional protection schemes, preventing misoperations. However, this solution becomes imprac-

tical due to the introduction of standards such as IEEE 1547 and IEEE 2800. These standards mandate DGs to remain connected to the grid during fault conditions, ensuring they ride through faults without disconnection [53, 54].

- Sympathetic Tripping A sympathetic trip occurs when a protection device operates incorrectly or undesirably during a fault, resulting in the disconnection and de-energization of the healthy section of the network. This issue may arise due to inaccuracies in protection relay settings or unanticipated/non-conventional characteristics of network faults.

To illustrate, The sympathetic tripping of the overcurrent element is discussed in [55, 56, 57, 58, 59, 60] and can be described using the simple circuit depicted in Fig. 2.1. Assuming relays R1, R2, and R3 are configured and coordinated with time overcurrent reclosing elements (ANSI 51X and 79). The fault current observed downstream of relay R2 increases when a Distributed Generator (DG) is introduced at either location x or y . Furthermore, the fault current direction sensed by R3 differs when DG is integrated at location y compared to location x .

For instance, if DG is integrated at location y , recloser R2 may operate permanently for a temporary fault at it's downstream; this occurs because the fault current seen by R2 increases while the contribution seen by R1 diminishes. Additionally, if DG is integrated at location y , R3 may operate faster than R2 because R2 is not coordinated with R3, leading to unintentional islanding and causing an outage in the healthy zone (Load 2 and Load 3). These false trips can be prevented by incorporating directional elements to supervise the operation of the overcurrent element [56, 57, 59, 60]. Adaptive relay settings were adopted by [58, 61, 62, 63, 51, 52] to accommodate varying network scenarios. Another solution approach is using current limiters, which can be employed to minimize the fault contribution [64, 65].

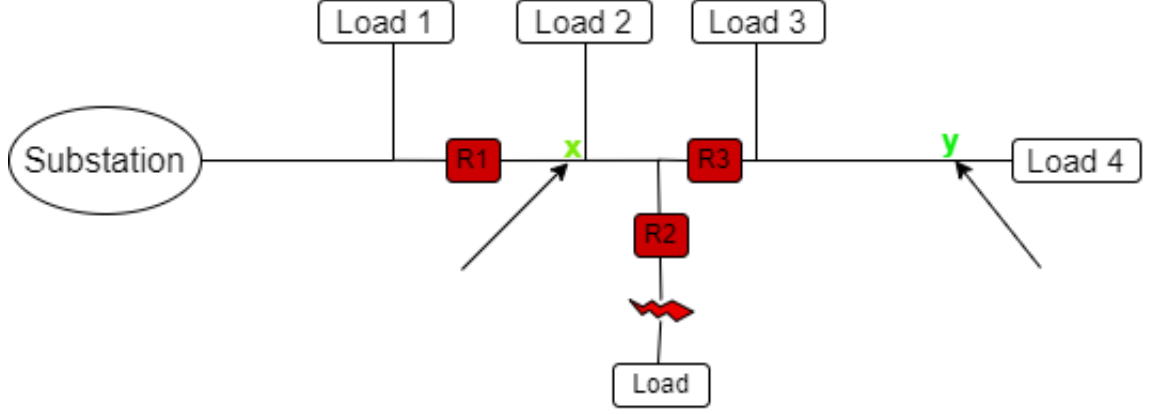


Figure 2.1: A Simple radial single line drawing

The investigation into the occurrence of false tripping in frequency-based elements (ANSI 81) when Distributed Generators (DG) are present was explored by authors in [66, 67]. In their study, the proposed solution by [67] involves determining the rate of change of frequency measuring time window by using the natural resonance frequency of the DG system. Another suggested solution is supervising the fluctuation's direction by modifying the element's logic.

An example of false tripping of distance element is the overreach of the distance element after unintentional tripping of DGs has also been investigated [68, 69, 70, 71], communication assisted schemes were introduced as a viable solution in [68], while an alternative approach was proposed in [69], employing a machine learning technique to detect DG tripping and implementing a blocking scheme to oversee the distance element.

The false tripping of the directional element has been investigated in [59, 60, 72]; this misoperation is primarily attributed to the fault characteristics of Inverter-based generators during fault ride-through conditions. The authors suggested a high-frequency impedance-based protection scheme in [60], while an alternative approach using superimposed impedance-based logic is proposed in [72]. In our work in [73], we've presented a solution

based on adjusting conventional settings, detailed in this dissertation.

- **Blinding of Protection Element** Blinding of the protection element can be described as the failure of the protection element to detect and/or respond appropriately to a fault or abnormal condition within the system. The failure of protection elements to detect and isolate faults due to DG integration has been discussed in several literature [39, 40, 42, 44, 45, 46, 47, 63, 70]. An instance of blinding in an overcurrent element is depicted in Fig. 2.1. After integrating a DG at location x , the fault current observed by relay R1 diminishes. This reduction in fault current may hinder relay R1 from operating within the expected time frame, effectively causing blinding. In this scenario, the DG integrated at location x blinds relay R1. The authors in [39, 74, 75, 44, 46, 63] describe the blinding of protection impacting the coordination of overcurrent protection devices; proposed solutions encompass adaptable protection coordination schemes.

A typical occurrence of blinding in a distance element is the underreach of the distance element [76, 77, 78, 79]. The distance element operates based on impedance and defines its reach as the impedance value at which the element is triggered. In the provided diagram 2.2, the zone of reach encompasses Line 1 and Line 3, with the configured impedance on the relay settings being the sum of impedances in Line 1 and 3. The element responds if the fault falls within its zone of reach, i.e., when the impedance seen by the relay is less than the configured impedance.

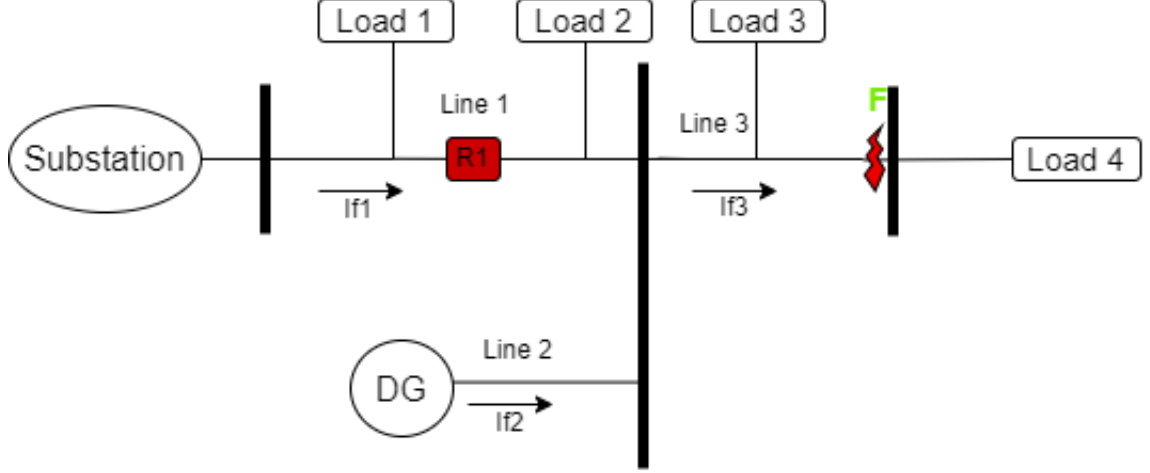


Figure 2.2: A Simple circuit illustrating the underreach of distance element

To illustrate underreach in the presence of a remotely fed DG, let's consider a case where the configured reach of the distance relay is Line 1 and Line 3. In the event of a fault at Line 3, the fault current is supplied by both Line 1 and the DG in Line 2, with the DG contributing a remote infeed. Equation 2.1 represents the relay impedance setting (Z_{reach}), assuming no DG. However, after integrating the DG, the impedance measured by the relay (Z_{meas}) increases, effectively blinding the relay from operating. This increase in impedance is a consequence of the fault current contribution by the DG, as detailed in equations 2.2 through 2.5.

To address this issue, an improved scheme based on delay and zero-sequence impedance was introduced by [79]. Additionally, a communication-assisted scheme was put forth by [80], and an alternative solution was presented by [81, 82], which involved a traveling wave-based distance element to prevent the misoperation.

$$Z_{reach} = (Z_1 + Z_3) \quad (2.1)$$

$$V_{meas} = I_1 \times Z_1 + \mu Z_3 (I_1 + I_2) \quad (2.2)$$

$$I_3 = I_1 + I_2 \quad (2.3)$$

$$Z_{meas} = \frac{I_1 \times Z_1 + \mu Z_3 (I_1 + I_2)}{I_1} \quad (2.4)$$

$$Z_{meas} = (Z_1 + Z_3) + \left(\frac{I_2}{I_1}\right) Z_3 \quad (2.5)$$

Underreach phenomena: $Z_{meas} > Z_{reach}$

where:

Z_{reach} : Relay impedance setting or reach

Z_1 : Impedance associated with line1

Z_3 : Impedance of line3 up to the point of fault F

V_{meas} : Voltage measured by relay during fault

Z_{meas} : Actual Impedance measured by relay during fault

I_1 : Fault current flowing through impedance Z_1

I_2 : Fault current contribution by DG from Line2

I_3 : Fault current flowing through line3 after the fault at point F

It's crucial to recognize that sympathetic tripping and blinding of protection elements can result in the misoperation of protection devices or lead to protection miscoordination. The solutions explored in the existing literature can be summarized as follows:

1. Disconnecting DG: This involves isolating the Distributed Generator (DG) during faults [39, 40, 41, 42, 43, 44].
2. Fault Current Limiters (FCL): Utilizing FCL to diminish the contribution of faults [64, 65, 58].
3. Communication-Assisted Protection Scheme: Implementing schemes that use communication for enhanced protection [62, 63, 68, 80].
4. Adaptable Protection Scheme: Employing protection schemes that can

adapt to varying network conditions [61, 62, 63, 75].

5. Modification of Traditional Relay Settings: Adjusting conventional relay settings to improve performance [60, 72, 79, 82, 73].
6. Modification of Inverter Controller: Modifying the controller of inverters to enhance protection [83, 84, 85, 86].

According to NERC, The misoperation of the power system protection system is a result of the following eight types of causes [87]:

- AC and DCs system: This includes misoperations caused by Current Transformer (CT) Saturation, Potential Transformer (PT) transient responses, DC noise, wiring problems, or wiring damage
- Personnel Error: This includes misoperation mistakes caused by technicians during commissioning or maintenance activities
- Relay Settings: This cause includes misoperations due to errors in the issued setting, including setting errors caused by inaccurate modeling
- Communication Failures: This cause includes misoperations due to failures in the communication systems associated with protection schemes, including misoperations caused by loss of carrier, spurious transfer trips associated with noise, communications provider errors resulting in poor performance of communications, loss of fiber optic communication equipment, or microwave problems associated with signal loss or degradation
- Relay Malfunction: This includes situations where correct relay settings without error are configured, but the relay fails to operate during fault or is unnecessarily operated. To resolve this, the utility will always work with the relay manufacturers to find a solution

- **Unknown/Unexplainable Cause:** This includes misoperation that the root cause has not been known and is still under technical investigation

In Fig. 2.3 [1], the data illustrates the frequency of misoperations in the western interconnection over the past seven years. These misoperations are categorized into two groups: those attributed to settings and relay malfunctions and those caused by other factors.

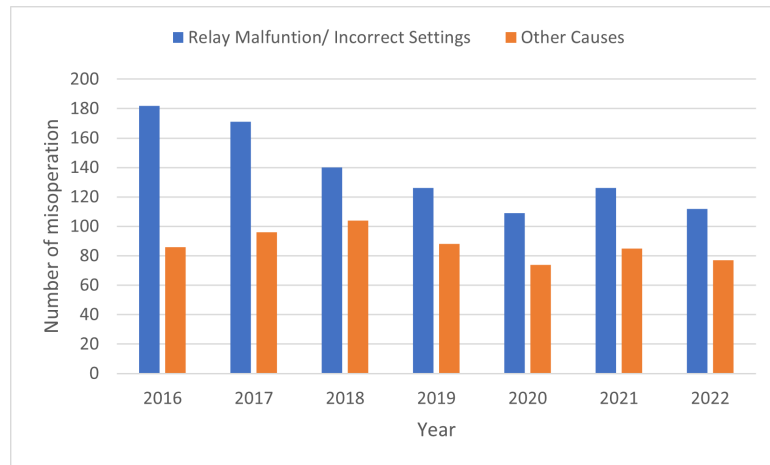


Figure 2.3: Western interconnection misoperation between 2016 and 2022 [1]

Despite a gradual reduction in misoperations over the last seven years, approximately 60% of protection system misoperations can be attributed to relay malfunctions and incorrect settings [1]. However, considering the implementation of IEEE 1547 and IEEE 2800 in 2022, the number of misoperations is expected to increase. Given that the central theme of this dissertation revolves around power system protection, the subsequent section will delve into a comprehensive exploration of power system protection.

2.2 Overview of Power System Protection

The primary goal of power system protection is to detect faults in an electrical power system and isolate them as quickly as possible to ensure the rest of the system can continue to operate safely. Faults are any abnormal flow of electric

current caused by insulation breakdown, which can be due to lightning strikes, snowstorms, falling trees, aging insulation, etc. The power system protection operation is based on principles and guided performance criteria highlighted below.

2.2.1 Power System Protection Sequence of Event

The sequence of events in power system protection is a series of steps to detect faults or abnormalities within an electrical power network and take necessary actions to safeguard the system. Here's a generalized sequence of events in power system protection:

1. **Fault Incidence:** An abnormal condition, such as a fault, occurs somewhere within the power system due to reasons like insulation breakdown, equipment failure, lightning strikes, or other disturbances.
2. **Sensor Detection:** Current Transformers (CTs) and Potential Transformers (PTs) detect variations in current and voltage parameters across the system.
3. **Fault Identification and Relay Operation:** Protection relays monitor system parameters and analyze sensor outputs. They utilize predefined logic or protection algorithms based on the protection principles to determine the presence and type of fault before sending a trip signal to the affected area's associated circuit breakers or switching devices.
4. **Circuit Breaker Operation:** The circuit breakers, upon receiving the trip signal, swiftly disconnect the faulty section or equipment from the rest of the system. This action isolates the fault, preventing its propagation and minimizing potential damage to the network.
5. **Fault Clearance:** Once the faulty section is isolated from the grid, the

maintenance personnel can investigate and repair the affected equipment before the system is restored to normal operation.

The research work in this dissertation is focused on fault identification and relay operation.

2.2.2 Power System Protection Principle

Protection principles are the specific fundamentals required for the design and operation of protective relays and devices within electrical power systems; the principles include:

1. Differential Protection: Differential relaying compares currents entering and leaving a protected zone. It detects internal faults by identifying any imbalance between these currents, signaling the presence of a fault within the protected zone.
2. Distance Protection: Typically, Distance relays operate based on impedance measurement to determine the distance to a fault from the relay location. They operate when the measured impedance surpasses a predetermined threshold, indicating a fault.
3. Overcurrent Protection: Overcurrent relays detect abnormal current levels in a protected zone, indicating a fault. They operate when the current exceeds a predefined threshold,
4. Overflux Protection: Overflux relays safeguard transformers from excessive magnetic flux, which can lead to core saturation and overheating. These relays detect and prevent high flux levels within the transformer core.
5. Frequency Protection: Frequency relays operate when the system frequency deviates from the acceptable range, signaling a deviation from normal operating conditions. They may trigger actions such as load shedding

to stabilize the system.

6. Voltage Protection: Voltage relays operate when the system voltage deviates from the acceptable range, indicating potential system faults or abnormalities.
7. Directional Protection: Directional relays operate based on the direction of fault current flow

The research work in this dissertation encompasses directional and overcurrent protection principles.

2.2.3 Power System Protection Performance Metrics

The performance criteria collectively guide the design, implementation, and maintenance of protective systems within electrical power networks, aiming to ensure the power system's safety, reliability, and stability under normal and abnormal operating conditions. Some essential power system protection criteria include:

1. Selectivity: Protective devices should isolate only the affected part of the system during a fault while maintaining the rest of the network operational. The aim is to ensure maximum continuity of service with minimum system disconnection.
2. Reliability: Protective devices must operate accurately by detecting in-zone and out-zone faults
3. Sensitivity: Protection devices should be able to identify fault regardless of level of severity
4. Speed: Protective devices should operate swiftly to isolate faults and minimize the impact on the rest of the system; however, an intentional delay is

required to coordinate the primary and backup protection device or avoid tripping temporary faults

5. Cost and Simplicity: The protection system's design should be simple and at a reduced cost while ensuring that other performance criteria are met.

CHAPTER 3: FAULT CHARACTERISTICS OF INVERTER BASED GENERATORS

The impact of inverter-based generation on power system protection has been a predominant research area because the proper operation of the protection schemes is critical to the reliability of the power system and also important for the safety of public and electrical grid equipment. The increased modernization of the grid and the need to generate clean energy resources have led to the increased adoption of Inverter-Based Distributed Generators (IBDG). Hence, it is important to understand the fault behavior of the different types of generators, this will help to adapt the traditional protection scheme to operate seamlessly. The misoperation of traditional schemes as a result of IBDG integration was identified in Chapter 2, including false tripping, blinding of protection devices, etc.

To maximize the full benefit of IBDG, it is imperative to develop protection schemes that are compatible and adaptable to the increased integration of IB-DGs. However, to develop this protection scheme, detailed knowledge of the behavior of the distributed generator needs to be investigated. This chapter solely focuses on this investigation. The simulations were done on EMTP-RV to illustrate the fault characteristics. A 33kV radial test system shown in Fig. 3.1 is used for this study. The point of interconnection (POI) of the DG is bus 1, the substation is located at bus 2, the current and voltage are measured at bus X, and faults are applied at bus 3 in the different scenarios. The three types of faults simulated are Three phase-to-ground faults, double phase-to-ground

faults, and single phase-to-ground faults. The sequence and phase components for current and voltage are analyzed for fault types and generators.

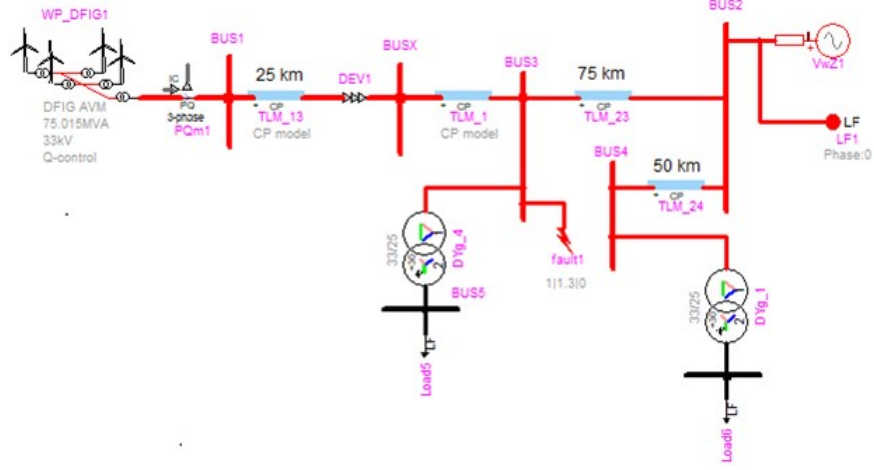


Figure 3.1: 33kV Test System

3.1 Main Contribution

This chapter aims to fully understand distributed generators' fault behaviors, including synchronous and inverter-based generators. As such, the following contributions are achieved

- Modeled inverter-based generator with a different control architecture
- Presented and compared the fault characteristics of synchronous generators and inverter-based generators with the different control architecture

The parameters compared are the phase and sequence component for voltage and current; the magnitude and angle of the phase and sequence component are considered.

The investigation considers inverter generators, including a Doubly Fed Induction Generator (DFIG) and four types of Full-Scale Converters (FSC) with different control schemes. The investigation and result of this work were published in 2022 [88]

3.2 Fault Characteristics of Synchronous Generator

The type of generator used in a traditional grid is the synchronous generator; the fault characteristic is well established and can be modeled by an R-L circuit and a voltage source behind an impedance. The fault current ($i_f(t)$) contribution of the synchronous generator can be estimated using (3.1). It comprises a transient and steady-state component. The transient component is the DC component, which determines the maximum magnitude at fault time $t=0$. The fault current decreases from (3.2) to (3.3).

$$i_f(t) = \sqrt{2}V_t \left[\left(\frac{1}{X_d''} - \frac{1}{X_d'} \right) e^{\frac{t}{T_d''}} + \left(\frac{1}{X_d'} - \frac{1}{X_d} \right) e^{\frac{t}{T_d'}} + \frac{1}{X_d} \right] \sin(\omega t + \alpha - 90) \quad (3.1)$$

$$i_f(t) = \frac{\sqrt{2}V_t}{X_d''} \quad (3.2)$$

$$i_f(t) = \frac{\sqrt{2}V_t}{X_d} \sin(\omega t + \alpha - 90) \quad (3.3)$$

Where:

$i_f(t)$: Fault Current Contribution of Synchronous Generator at time (t)

V_t : Terminal Voltage of Synchronous Generator at time (t)

X_d : Synchronous Reactance

X_d' : Transient Reactance

X_d'' : Subtransient Reactance

T_d' : Short – Circuit Transient Time Constant

T_d'' : Short – Circuit Subtransient Time Constant

The fault current of a conventional distribution or transmission line is determined by the power system impedance, including the generator's short circuit impedance and line impedance. The low values of system impedance readily result in high fault currents in alignment with Ohm's law. The test system in Fig. 3.1 is used, and the DFIG is replaced with a synchronous generator; the result from three fault cases: Three-phase to ground fault, double phase to ground fault, and single phase to ground fault is analyzed. The phasor representation of the sequence component of the fault voltage and current are illustrated in Fig. 3.2 while the magnitude of the phase and sequence component is shown in Table 3.1; from the phasor plots, it can be seen that the positive sequence and negative sequence fault characteristics are inductive and capacitive respectively, for three phases to ground fault, the negative sequence and zero sequence current is zero; while for single phase to ground fault, the positive, negative, and zero sequences are approximately the same value, this aligns with the theoretical calculation.

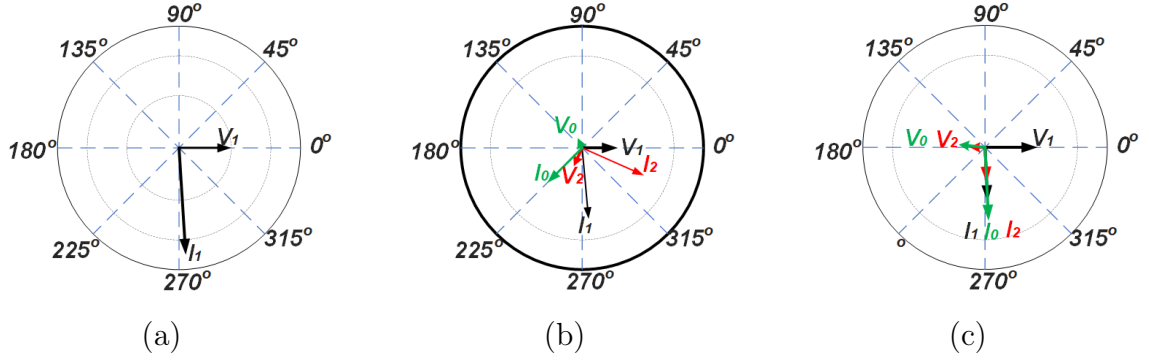


Figure 3.2: SG scenario: Phasor representation of the fault current and voltage sequence component (a) ABC-G Fault (b) AB-G Fault (c) A-G Fault

3.3 Fault Characteristics of Double Fed Induction Generators (DFIG)

The DFIG is an inverter-based generator with two converters (the rotor side controller and grid side controllers). Authors in [89, 90, 91] describe the impact

Table 3.1: SG Scenario: Magnitude of the Fault Current and Voltage Sequence Component

	ABCG (P.U.)	ABG (P.U.)	AG (P.U.)
Imag (faulty phase)	5.5	5.5	3.8
Vmag (faulty phase)	0.38	0.38	0.38
I (positive sequence)	5.5	3.1	1.2
I (negative sequence)	0	0.8	1.3
I (zero sequence)	0	2.3	1.19
V (positive sequence)	0.38	0.6	0.82
V (negative sequence)	0	0.3	0.12
V (zero sequence)	0	0.2	0.3

of DFIG on power systems. The stator of the induction generator is directly connected to the grid, and the rotor is connected to the grid through a rotor-side converter (AC-DC) and grid-side converter (DC-AC); both converters have independent two-level controller; the dq-frame current controller and the ac voltage reference controller. A large current is expected to flow through the stator loop during fault events. This will induce a high voltage in the rotor side, causing a high current flow. The rotor current is limited by the Rotor Side Control (RSC); the RSC will disconnect if the current goes beyond the converter rating to avoid damage. At this period, the GSC cannot transmit rotor power to the grid because the POI voltage is less than the rotor voltage. However, Low Voltage Real Time (LVRT) can be implemented on DFIGs using auxiliary hardware or modifying the control strategy. The common auxiliary hardware solution is the introduction of a crowbar to reduce the rotor's current, which also allows the GSC to operate as a static VAR compensator. Other auxiliary hardware solutions include the use of a dynamic voltage restorer, which is a voltage source inverter [92]; it incorporates a Passive Resistance Network (PRN) in series with the stator side to damp synchronous frame stator flux oscillations. The authors in [93, 94] proposed the modification of the control architecture: [92] presented a feedforward transient compensation control method

to limit transient rotor current, while [93] implemented a virtual impedance to control the stator current during fault the virtual impedance was implemented in the rotor side current control loop.

To illustrate the fault characteristics of DFIGs, Figure 3.3 is the block diagram of the DFIG model that was integrated with the single line diagram in Fig. 3.1; it is a common type of DFIG with crowbar implementation. This DFIG model is described in [95]. During a fault, the GSC operates as a static VAR compensator to satisfy the LVRT requirement. Typically, the fault behavior of a DFIG is determined by both the control system and the electrical parameters of the machine. Equations (3.4) and (3.5) are used to compute an approximation of the negative-sequence impedance Z_{WTG}^- [96].

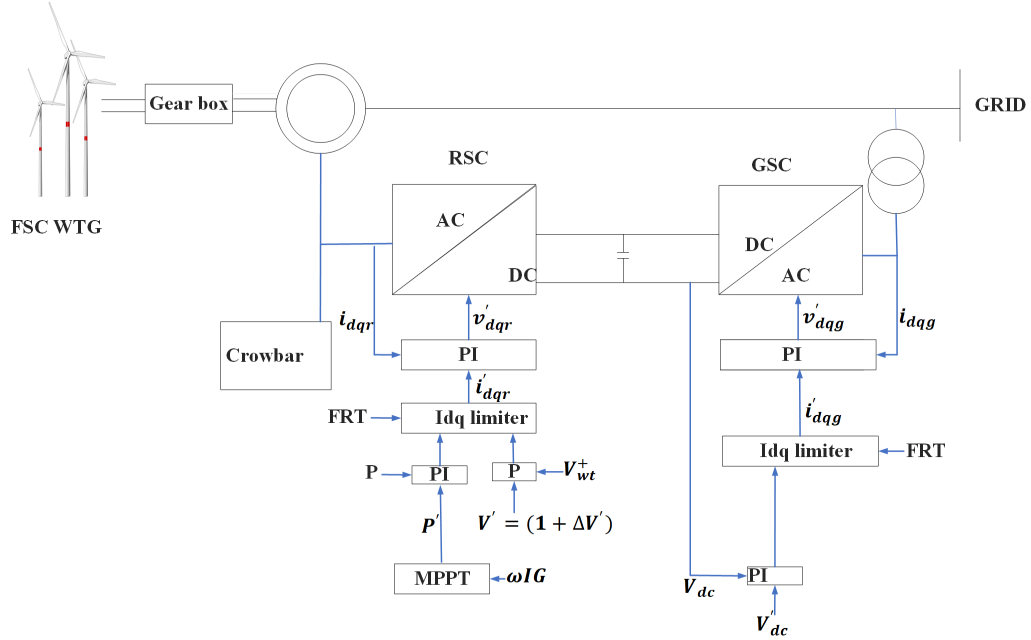


Figure 3.3: Block diagram of a DFIG showing the control blocks

$$|Z_{WTG}^-| = \frac{2}{\sqrt{|Y_{ds}^{SFR}|^2 + |Y_{qs}^{SFR}|^2 - 2|Y_{ds}^{SFR}||Y_{qs}^{SFR}|\sin(\phi_{Y_{ds}^{SFR}} - \phi_{Y_{qs}^{SFR}})}} \quad (3.4)$$

$$\angle \phi_{Z_{WTG}^-} \approx \frac{|Y_{qs}^{SFR}| \sin(\phi_{Y_{qs}^{SFR}}) + |Y_{ds}^{SFR}| \sin(\phi_{Y_{ds}^{SFR}})}{|Y_{ds}^{SFR}| \sin(\phi_{Y_{ds}^{SFR}}) + |Y_{qs}^{SFR}| \sin(\phi_{Y_{qs}^{SFR}})} \quad (3.5)$$

Where:

Z_{WTG}^- : *Negative sequence component impedance of the DFIG*

$\phi_{Z_{WTG}^-}$: *Phase angle of Z_{WTG}^-*

Y^{SFR} : *A function of the machine electrical parameters, the RSC parameters, and the measurement filter parameters*

ϕ^{SFR} : *Phase angle of Y^{SFR}*

Y_{ds}^{SFR} : *d component of Y^{SFR}*

Y_{qs}^{SFR} : *q component of Y^{SFR}*

$\phi_{Y_{ds}^{SFR}}$: *d component of ϕ^{SFR}*

$\phi_{Y_{qs}^{SFR}}$: *q component of ϕ^{SFR}*

Table 3.2 shows the magnitude of the phase current, phase voltage, and the magnitude of its sequence component during AG, BCG, and ABCG fault conditions. Figure 3.4 displays the phasor representation of the sequence components. The fault characteristics of a DFIG are similarly inductive to an SG, but the current amplitude is much lower, and the post-fault voltage phase and frequency deviate more from pre-fault when compared to SG. The magnitude of the negative and zero sequence components is smaller than SG but significant during an unbalanced ground fault; the relative phase angle between the voltage and current sequence component is like SG.

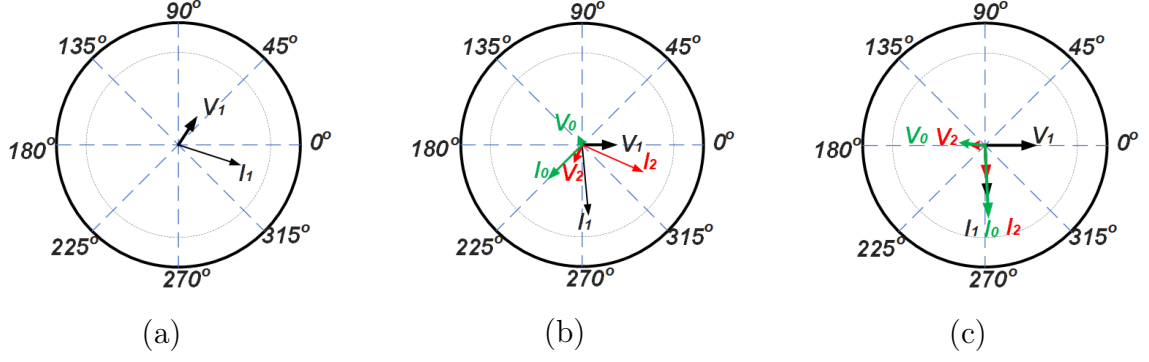


Figure 3.4: DFIG Scenario: Phasor representation of the fault current and voltage sequence component (a) ABC-G Fault (b) AB-G Fault (c) A-G Fault

Table 3.2: DFIG Scenario: Magnitude of the Fault Current and Voltage Sequence Component

	ABCG (P.U.)	ABG (P.U.)	AG (P.U.)
Imag (faulty phase)	1	1.05	1.6
Vmag (faulty phase)	0.05	0.2	0.25
Ipos (I_1)	1	1.18	1.2
Ineg (I_2)	0	0.55	0.39
Izero (I_0)	0	0.6	0.8
Vpos (V_1)	0.05	0.3	0.7
Vneg (V_2)	0	0.28	0.2
Vzero (V_0)	0	0.2	0.3

3.4 Fault Characteristics of Full-Scale Converters (FSC) Genertors

Typically, the type-IV Wind Turbine Generator (WTG) and PV/battery inverter-based generator are similar setups shown in Fig 3.5; they both comprise two converters: the grid side converter (DC-AC converter) and the second converter varies for WTG and PV/battery-based generator. It is an AC-DC converter for type IV WTG and DC-DC for PV/battery-based inverter generators. The grid-side control's architecture determines the behavior of the FSC generators, and the FSC generator's impedance can be estimated using (3.6).

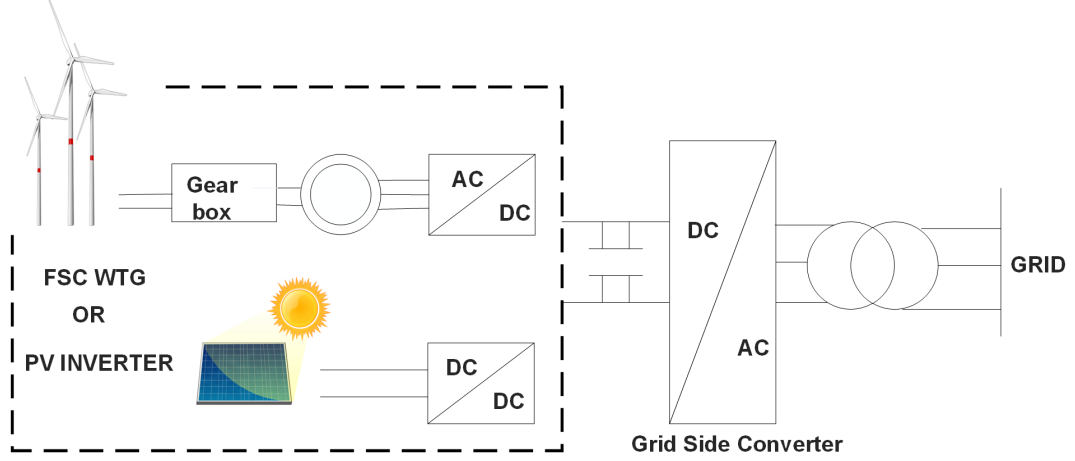


Figure 3.5: A simplified block diagram for an FSC-based generator

$$|Z_{WTG}^-| = \frac{R + jX + H_{filter}(H_{PI}^g - R + jX)}{1 - H_{filter}} \quad (3.6)$$

Where:

Z_{WTG}^- : Negative sequence component impedance of the DFIG

R : Resistance of the choke filter

X : Reactance of the choke filter

H_{filter} : Complex gain of the measurement filter at the network frequency

H_{PI}^g : Complex gain of the PI controller at twice the grid frequency

The grid side controls the architecture of a grid-following inverter and comprises the current controller; current-controlled VSI can be classified into Coupled Sequence Control (CSC) and Decoupled Sequence Control (DSC) controlled inverters. The CSC controls the phase currents, while the DSC independently controls positive or negative sequence currents injected at the Point of Interconnection (POI). The control architecture varies for different inverter manufacturers. Four control architectures are considered in this study.

3.4.1 Coupled Sequence Control (CSC) Architecture

Figure 3.6 presents a simplified block diagram of the CSC section of a Grid Side Controller (GSC); the phase current (I_{abc}) is measured and transformed to the DQ rotating reference frame without decoupling the sequence component, this measured DQ is compared with a reference DQ value based on a defined control objective such as reactive power control, voltage control, power factor controls, etc. To illustrate the fault characteristics of a CSC, the IBDG in Fig. 3.1 is changed to an FSC with a CSC architecture (FSC-CSC).

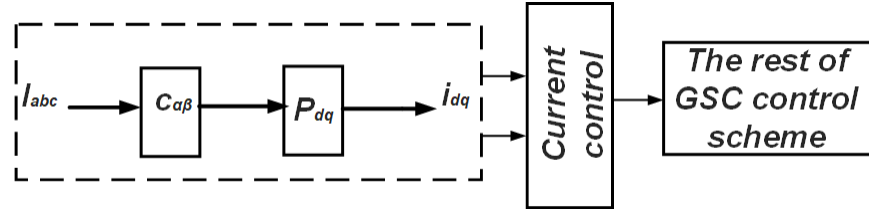


Figure 3.6: A simplified block diagram of the CSC section of a GSC

Table 3.3 shows the magnitude of the phase current, phase voltage, and sequence component during AG, BCG, and ABCG fault conditions of an FSC-CSC. Fig. 3.7 displays the phasor representation of the sequence components. The magnitude of the phase voltage and current are similarly small, like a DFIG. The magnitude of the negative and zero sequence components is smaller compared to DFIG and SG during an unbalanced ground fault. The difference in phase angle of the voltage and current sequence components are representations of a non-inductive system because I_1 does not lag V_1 by approximately 90, and I_2 does not lead V_2 by approximately 90 during fault conditions.

3.4.2 Decoupled Positive Sequence Control (DPSC) Architecture

The Decoupled Positive Sequence Control (DPSC) Architecture is a decoupled sequence control in which only the positive sequence is extracted from the mea-

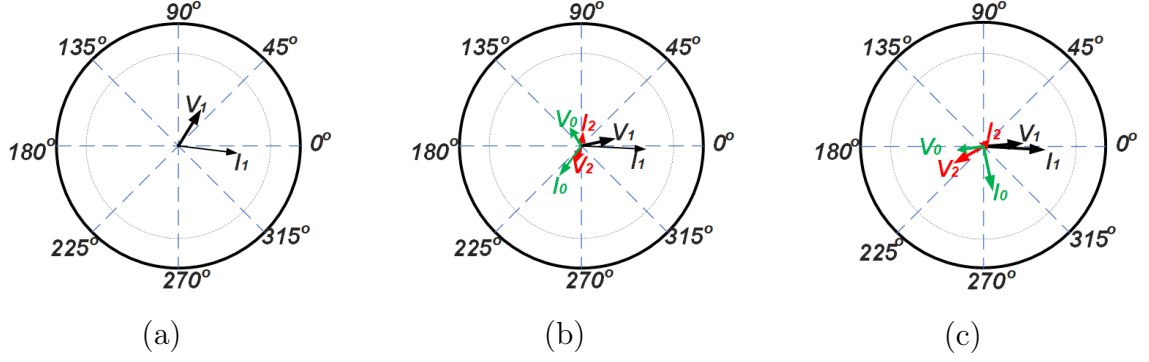


Figure 3.7: FSC-CSC Scenario: Phasor representation of the fault current and voltage sequence component (a) ABC-G Fault (b) AB-G Fault (c) A-G Fault

Table 3.3: FSC-CSC Scenario: Magnitude of the Fault Current and Voltage Sequence Component

	ABCG (P.U.)	ABG (P.U.)	AG (P.U.)
Imag (faulty phase)	1.18	2	1.6
Vmag (faulty phase)	0.05	0.3	0.3
Ipos (I_1)	1.18	1.15	1.15
Ineg (I_2)	0	0.1	0.08
Izero (I_0)	0	0.72	0.75
Vpos (V_1)	0.05	0.45	0.7
Vneg (V_2)	0	0.4	0.3
Vzero (V_0)	0	0.25	0.28

sured PCC signal and controlled, while the negative sequence component of the POI signals is filtered. Figure 3.8 shows a simplified block diagram of the DPSC section of a Grid Side Controller (GSC). The POI voltage and current are measured and then transformed to the DQ rotating reference frame. The positive sequence components are extracted from the DQ frame before feeding to the controllers. This ensures the inverter current injection remains balanced irrespective of the grid or grid fault condition imbalance. This control is seldom used for WTG to avoid using a large capacitor required to absorb ripples caused by the unbalanced POI current [97]. However, the current's balanced nature suppresses the injected current's negative sequence component.

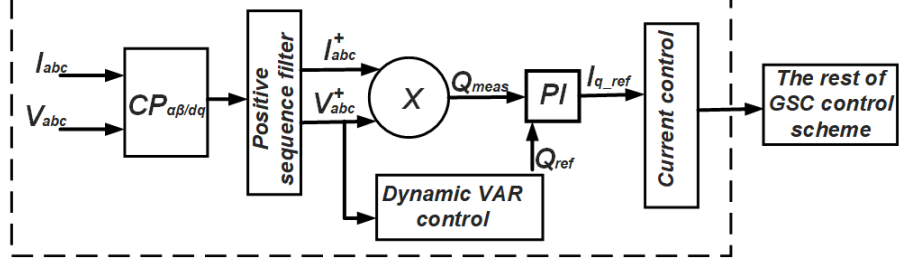


Figure 3.8: A simplified block diagram of the DPSC section of the GSC architecture

To illustrate the fault characteristics of a DPSC, the IBDG in Fig. 3.1 is changed to an FSC with a DPSC architecture (FSC-DPSC). Fig. 3.9 displays the phasor representation of the sequence component by the DPSC type inverter during a Single line-to-ground (SLG) fault. The simulation is done using a Typhoon virtual simulator. The injected current at the POI is balanced and has only a positive sequence component, while the voltage remains unbalanced.

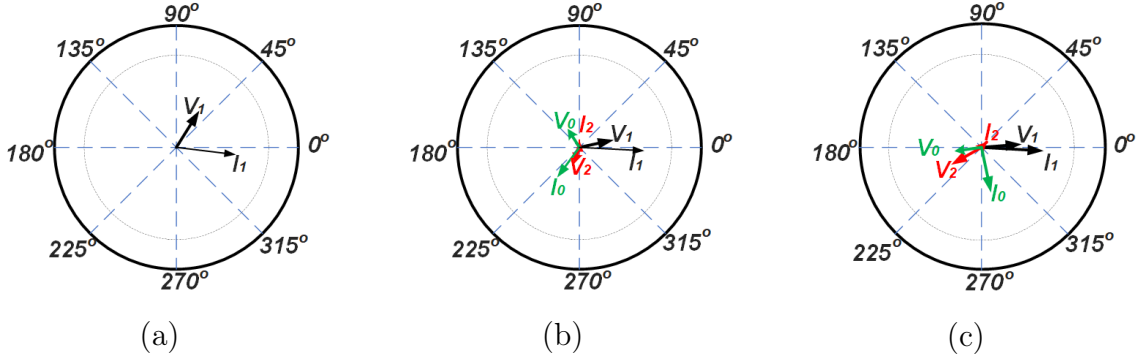


Figure 3.9: Phasor representation of the fault current and voltage sequence component for FSC with DPSC architecture (a): ABC-G Fault, (b): AB-G Fault, (c) A-G Fault

3.4.3 Decoupled Positive and Negative Sequence Control (DPNSC)

Architecture

The Decoupled Positive and Negative Sequence Control (DPNSC) Architecture is a type of decoupled sequence control in which the positive and negative sequence components of the PCC current are decoupled and controlled independently. Figure 3.10 shows a block diagram of the DPNSC section of the GSC; the

decoupling is achieved by generating an oscillating signal from a combination of a low-pass filter (LPF) with double line frequency park transform (P_{dq}^{-2}, P_{dq}^{+2}), which is then subtracted from single line frequency park (P_{dq}^{+1}, P_{dq}^{-1}) transformed signal [95]. The output is a positive and negative sequence component of the POI current, which is then controlled independently.

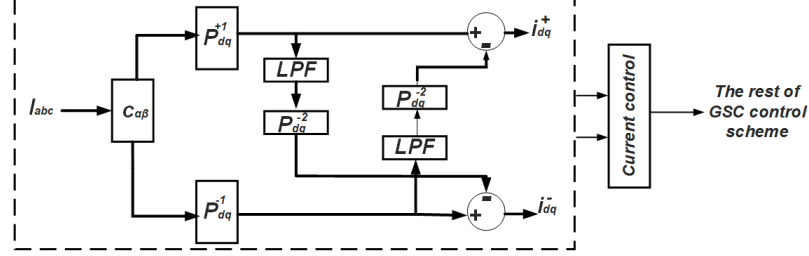


Figure 3.10: A simplified block diagram of the DPNSC section of the GSC architecture

To illustrate the fault characteristics of a DPNSC, the IBDG in Fig. 3.1 is changed to an FSC with a DPNSC architecture (FSC-DPNSC). Table 3.4 shows the magnitude of the phase current, phase voltage, and the magnitude of its sequence component during AG, BCG, and ABCG fault conditions. Fig. 3.11 displays the phasor representation of the sequence component. The magnitude of the phase voltage and current are similar to a DFIG. The magnitude of the negative and zero sequence components is more than an FSC-CSC but less than DFIG and SG during an unbalanced ground fault. The difference in phase angle of the voltage and current sequence component is not inductive during fault conditions.

3.4.4 Modified-Decoupled Positive and Negative Sequence Control

(M-DPNSC) Architecture

The Modified Decoupled Positive and Negative Sequence Control (M-DPNSC) architecture is achieved by modifying DPNSC with the incorporation of the German VDE-AR-N 4120 grid code [2]; the German grid code aims to mimic

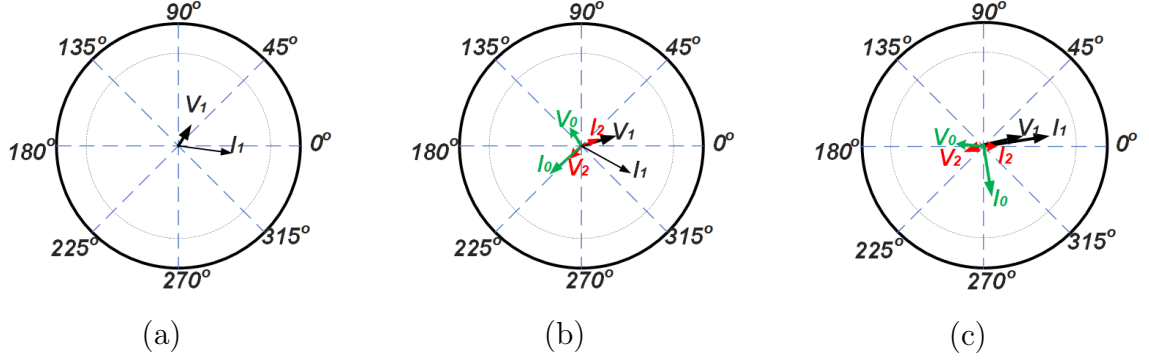


Figure 3.11: FSC-DPNSC Scenario: Phasor representation of the fault current and voltage sequence component (a) ABC-G Fault (b) AB-G Fault (c) A-G Fault

Table 3.4: FSC-DPNSC Scenario: Magnitude of the Fault Current and Voltage Sequence Component

	ABCG (P.U.)	ABG (P.U.)	AG (P.U.)
Imag (faulty phase)	1.2	1.7	1.7
Vmag (faulty phase)	0.05	0.3	0.3
Ipos (I_1)	1.18	1	1.05
Ineg (I_2)	0	0.32	0.32
Izero (I_0)	0	0.75	0.8
Vpos (V_1)	0.05	0.44	0.72
Vneg (V_2)	0	0.4	0.22
Vzero (V_0)	0	0.25	0.25

the traditional synchronous generator such that the inverter injects a negative sequence current and the injected current is proportional to a change in the negative sequence voltage using (3.7). Figure 3.12 shows the K-factor slope, which defines the relationship between the negative sequence component of injected current and the negative sequence component of the POI voltage [2]. The simplified block diagram of the implementation of (3.7) in the inverter GSC architecture is described in Fig. 3.13

$$K = \frac{\Delta I^-}{\Delta V^-} \quad (3.7)$$

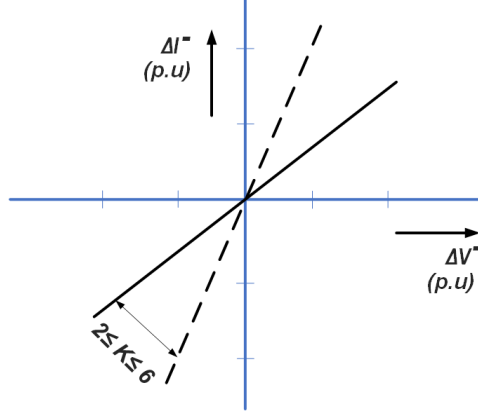


Figure 3.12: Plot of the relationship between POI voltage and current negative sequence component

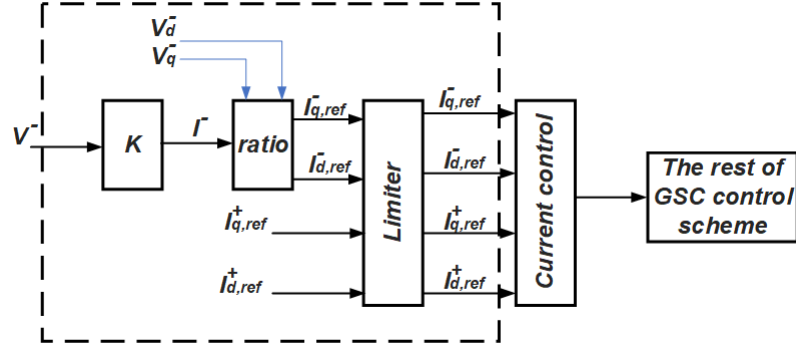


Figure 3.13: Implementation of German grid code in the GSC control [2]

To illustrate the fault characteristics of an M-DPNSC, the IBDG in Fig. 3.1 is changed to an FSC with an M-DPNSC architecture (FSC-M-DPNSC). Table 3.5 shows the magnitude of the phase current, phase voltage, and its sequence component during AG, BCG, and ABCG fault conditions. Figure 3.14 displays the phasor representation of the sequence component. The magnitude of the phase voltage and current are similar to DFIG. The magnitude of the negative and zero sequence components is greater than an FSC-DSC-1N but less than an SG during an unbalanced ground fault. The difference in phase angle of the voltage and current sequence component is also inductive.

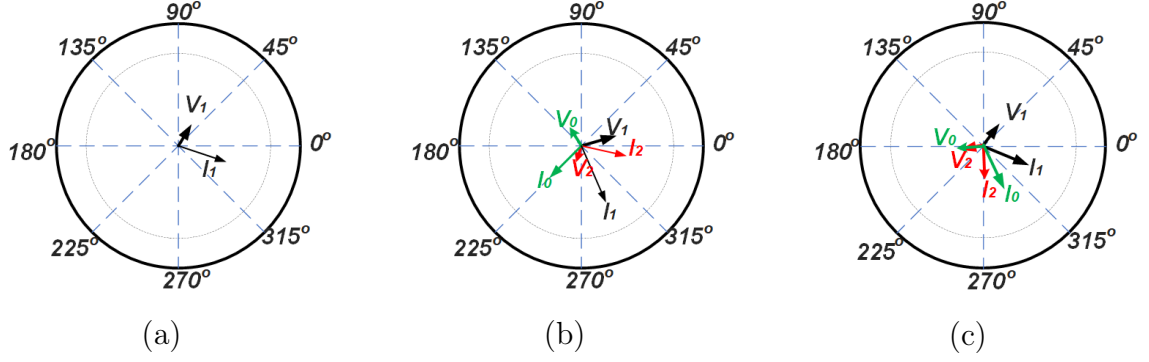


Figure 3.14: FSC-M-DPNSC Scenario: Phasor representation of the fault current and voltage sequence component (a) ABC-G Fault (b) AB-G Fault (c) A-G Fault

Table 3.5: FSC-M-DPNSC Scenario: Magnitude of the Fault Current and Voltage Sequence Component

	ABCG (P.U.)	ABG (P.U.)	AG (P.U.)
Imag (faulty phase)	1.2	1.3	1.5
Vmag (faulty phase)	0.05	0.3	0.3
Ipos (I_1)	1.18	0.7	0.9
Ineg (I_2)	0	0.5	0.4
Izero (I_0)	0	0.65	0.78
Vpos (V_1)	0.05	0.44	0.7
Vneg (V_2)	0	0.38	0.22
Vzero (V_0)	0	0.25	0.28

3.5 Summary of Investigation and Future Direction

This chapter explored the dynamic behavior of fault characteristics in Inverter-Based Distributed Generators (IBDGs). The investigation highlighted that IBDGs demonstrate a distinct fault behavior, especially regarding their fault current contributions compared to traditional generators like synchronous and induction types, potentially causing traditional protection schemes to misoperate.

Furthermore, the insights gained into the fault characteristics of IBDGs underscore the importance of a holistic approach to power system protection. This entails adapting existing protection schemes and embracing advanced technologies and methodologies to ensure that the protection architecture evolves in

tandem with the integration of IBDGs. As we continue to integrate more renewable and inverter-based resources into the power system, the lessons gleaned from this chapter will prove invaluable in steering the direction of future research and development efforts in power system protection.

The analysis pointed out that inverter-based generators could compromise the performance of conventional protection systems by highlighting the difference in fault characteristics of IBDG and synchronous generators. The uniqueness of IBDG fault characteristics can be attributed to its restricted short circuit current capacity, which results from the limited thermal capacity of the power electronic component. This current limitation and lack of inertia make IBDG a weak generating source. The main findings can be summarized as follows:

- For full-scale converters, IBDG fault current characteristics are determined by the grid side control architecture;
- For doubly fed induction generator, the characteristics of the fault current are determined by the electric parameters of the machine and the rotor side control architecture;
- The limited magnitude of phase current can lead to the misoperation of phase-based elements such as the phase overcurrent element;
- The limited magnitude of the current sequence component can cause misoperation of sequence-based elements, such as the mho distance element, negative and zero sequence overcurrent element;
- The power factor and phase angle of the sequence component of an inverter-based generator can be inductive, capacitive, or resistive, depending on the inverter control architecture. This non-inductive characteristic can misoperate the polarization of fault in traditional directional element, mho distance element, and misclassification of faults

Addressing these misoperations involves two main strategies:

- Modification of the Inverter Control Architecture -This includes implementation of virtual impedance, virtual inertia, and control of injected current sequence component
- Modification of the Protection Scheme - This includes modification of relay parameters, adoption of traveling wave-based protection schemes, high frequency-based protection schemes, and application of machine learning in protection systems

To harness the full potential of IBDGs, more effort should be focused on modifying the inverter control architecture such that its fault characteristics can mimic those of a conventional synchronous generator. The rise time of the control architecture should also be considered, as it can influence the response time of the relay protection element.

In addition, more studies should be performed on adopting a traveling wave-based protection scheme and applying artificial intelligence (AI) to power system protection. The adoption of AI should be aided by advanced computing processors and metering technology such that the input data required for machine learning can be distort-less.

In summary, enhancing the integration of IBDGs into the power grid requires a comprehensive grasp and effective management of their fault characteristics. The obstacles outlined in this chapter serve not as mere hindrances but rather as catalysts for innovation, driving us toward a future where the synergy between clean energy and grid reliability is achieved.

CHAPTER 4: NEGATIVE SEQUENCE VOLTAGE POLARISED (NSVP) DIRECTIONAL SCHEME MIS-OPERATION IN THE PRESENCE OF IBDG: INSIGHTS AND PREVENTION

As outlined in chapter 3, the fault behavior of an IBDG differs from that of a traditional synchronous generator, consequently impacting the performance of conventional protection schemes. This chapter focuses on the negative sequence voltage polarized directional scheme, commonly employed in bidirectional power flow networks, to determine either forward or reverse fault direction.

A directional element is fundamental and indispensable to other protection schemes because it is typically combined with other protection elements. Existing directional elements include phase directional elements, Positive-Sequence Voltage Polarized (PSVP) directional elements, Negative-Sequence Voltage Polarized (NSVP) directional elements, and zero-sequence directional elements.

For the phase directional element, the operating quantity is the phase current (I_A , I_B , and I_C) while the polarizing quantity is the phase-phase voltage (V_{BC} , V_{CA} and V_{AB}) of the un-faulted phases. The phase directional is susceptible to misoperation during a Single Line-to-Ground (SLG) fault because the three phases' directional elements are independent. Equation (4.1) to (4.3) shows the phase directional torque (T_A , T_B and T_C) for the phase directional elements.

$$T_A = |V_{BC}| |I_A| \times \cos [(\angle V_{BC}) - (\angle I_A)] \quad (4.1)$$

$$T_B = |V_{CA}| |I_B| \times \cos [(\angle V_{CA}) - (\angle I_B)] \quad (4.2)$$

$$T_C = |V_{AB}||I_C| \times \cos [(\angle V_{AB}) - (\angle I_C)] \quad (4.3)$$

For the zero sequence directional element, the operating quantity is the zero current (I_0), while the polarizing quantity can be zero sequence voltage (V_0) or a current from an external source (I_{POL}). The main setback is the presence of zero sequences mutual coupling, which can cause misoperation. Equations (4.4) and (4.5) show the torque equation for zero sequence voltage polarized (T_{32V}) and zero sequence current (T_{32I}) polarized directional element. $\angle Z_0$ is the zero sequence line impedance angle. A positive torque value depicts forward directional fault, while a negative torque depicts reverse directional fault.

$$T_{32V} = |3V_0||3I_0| \times \cos [\angle -3V_0 - (\angle 3I_0 + \angle Z_0)] \quad (4.4)$$

$$T_{32I} = |3I_{POL}||3I_0| \times \cos [\angle -3I_{POL} - (\angle 3I_0 + \angle Z_0)] \quad (4.5)$$

The Positive Sequence Voltage Polarized (PSVP) directional element operates based on the positive sequence current (I_1) as the operating quantity and the positive sequence voltage (V_1) as the polarizing quantity. However, while the PSVP directional element performs effectively for three-phase faults, it may experience misoperation during unbalanced faults due to the proximity of nominal load and fault current values. Equation (4.6) presents the torque (T_{32P}) equation for the PSVP directional element, where Z_1 represents the positive sequence line impedance. A positive torque value depicts forward directional fault, while a negative torque depicts reverse directional fault.

$$T_{32P} = |3V_1||3I_1| \times \cos [\angle 3V_1 - (\angle 3I_1 + \angle Z_1)] \quad (4.6)$$

In the Negative Sequence Voltage Polarized (NSVP) directional element, the

negative sequence current (I_2) serves as the operating quantity, while the negative sequence voltage (V_2) acts as the polarizing quantity. Unlike the PSVP, the NSVP directional element demonstrates reliable performance for unbalanced faults because the negative sequence fault contribution during fault is significantly higher than the nominal load. The torque (T_{32Q}) equation for the NSVP directional element, presented in (4.7), incorporates the negative sequence line impedance (Z_2). The NSVP stands out as the most efficient option, as it is unaffected by the limitations of PSVP and zero sequence directional elements. A positive torque value depicts forward directional fault, while a negative torque depicts reverse directional fault.

$$T_{32Q} = |3V_2||3I_2| \times \cos [\angle 3V_2 - (\angle 3I_2 + \angle Z_2)] \quad (4.7)$$

For some instances of remote faults when the polarizing quantity (V_2) might be low, a compensating quantity can be introduced to increase the polarizing quantity reducing (4.7) yield (4.10) [98]

$$T_{32QC} = \text{Re} [(V_2 - \alpha \times Z_{line} \times$$

$$I_2) \times (Z_{line} \times I_2)^*] \quad (4.8)$$

Further simplifying (4.10) yield (4.11) [98]

$$Z_2 = \frac{\text{Re}[V_2 \times (I_2 \times \angle Z_{line})^*]}{|I_2|^2} \quad (4.9)$$

Where:

Z_{line} : Angle of the line impedance which is known as the Minimum

Torque Angle (MTA)

Positive Z_2 : Forward fault

Negative Z_2 : Reverse fault

Forward fault : $Z_2 < \text{Forward threshold}$

Reverse fault : $Z_2 > \text{Reverse threshold}$

Forward threshold $<$ Reverse threshold

4.1 Main Contribution

Although the NSVP directional element excels compared to other directional elements, its effectiveness can be compromised when fault characteristics deviate from the traditional fault characteristics. Therefore, this chapter delves into its performance when integrated with IBDGs. The investigation and outcomes of this chapter were published in 2021 at the Applied Power Electronics Conference and Exposition (APEC) conference [73], and the contributions are as follows:

- Investigated the misoperation of NSVP directional element in the presence of IBDG, validating the unique fault behaviors of IBDGs
- Presented a prevention approach to address the identified misoperation issues of the NSVP directional element
- Conducted a Hardware-in-the-Loop (HIL) case study to validate the misoperation of the NSVP directional element and verify the effectiveness of the proposed prevention approach

4.2 Problem Formulation: Misoperation of NSVP Directional Element in the Presence of IBDG

The NSVP is tailored for conventional fault characteristics. In a standard network, an ideally balanced system produces negligible negative sequence component values, with slight increases occurring as network imbalances increase. Typically, power systems are maintained with balanced phases, resulting in minimal negative sequence components during normal operation. However, in

asymmetrical fault scenarios, the negative sequence experiences significant elevation depending on the fault type. Equations 4.10 and 4.11 show the equation for estimating the voltage and current negative sequence component.

$$V_2 = \frac{(V_a + (V_b \cdot e^{j \cdot 240^\circ}) + (V_c \cdot e^{j \cdot 120^\circ}))}{3} \quad (4.10)$$

$$I_2 = \frac{(I_a + (I_b \cdot e^{j \cdot 240^\circ}) + (I_c \cdot e^{j \cdot 120^\circ}))}{3} \quad (4.11)$$

Where:

V_a : Phase A Voltage

V_b : Phase B Voltage

V_c : Phase C Voltage

V_2 : Negative Sequence Voltage

I_a : Phase A Current

I_b : Phase B Current

I_c : Phase C Current

I_2 : Negative Sequence Current

For a balanced normal operation, Assume:

$$V_a = 120 \angle 0^\circ$$

$$V_b = 120 \angle 240^\circ$$

$$V_c = 120 \angle 120^\circ$$

$$I_a = 5 \angle 0^\circ$$

$$I_b = 5 \angle 240^\circ$$

$$I_c = 5 \angle 120^\circ$$

Substituting V_a , V_b , V_c , I_a , I_b , I_c in (4.10) and (4.11) respectively will yield a value of zero ($V_2 = 0$, $I_2 = 0$)

In the case of a Single-Line-to-Ground fault (Phase A to a ground fault), the analysis

is conducted in both forward and reverse directions.

Assume a forward direction Phase A to Ground (AG) fault:

$$V_a = 2\angle 0^\circ$$

$$V_b = 120\angle 240^\circ$$

$$V_c = 120\angle 120^\circ$$

$$I_a = 900\angle 270^\circ$$

$$I_b = 5\angle 150^\circ$$

$$I_c = 5\angle 30^\circ$$

Figure 4.1 illustrates the negative sequence component after substituting V_a , V_b , V_c , I_a , I_b , and I_c into equations (4.10) and (4.11). The resulting phasor values are as follows:

$$V_2 = 39.333\angle 180^\circ$$

$$I_2 = 298.333\angle -90^\circ$$

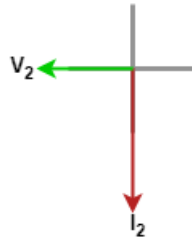


Figure 4.1: Forward direction SLG fault: Negative sequence component

Now, considering the reverse direction Phase AG fault:

$$I_a = 900\angle 90^\circ.$$

In the reverse fault direction, V_a , V_b , V_c , I_b , and I_c remain consistent with the forward direction AG. However, the current of the faulty phase (I_a) varies in terms of the phasor angle due to the change of fault direction. Figure 4.1 illustrates the negative sequence component after substituting V_a , V_b , V_c , I_a , I_b , and I_c into equations (4.10) and (4.11). The resulting phasor values are as follows:

$$V_2 = 39.333\angle 180^\circ$$

$$I_2 = 301.667\angle 90^\circ$$

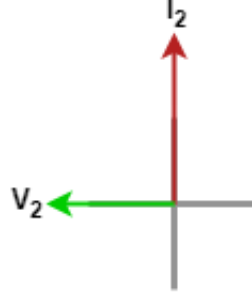


Figure 4.2: Reverse direction SLG fault: Negative sequence component

As depicted in Fig.4.1 and 4.2, representing conventional SLG fault characteristics, during a forward SLG fault, the negative sequence leads the negative voltage sequence by 90° , while during a reverse SLG fault, the negative current lags the voltage sequence by 90° . However, the presence of IBDG can cause misoperation of the directional element due to its unconventional angular relationship between the negative sequence voltage phase and the negative sequence current phase.

4.3 Simulation Setup and Case study

The simulation was conducted in two environment: firstly, on a virtual Typhoon HIL 603 simulator, where the network schematics were compiled on the virtual simulator, and secondly, on a physical Typhoon HIL real-time simulator, with the network schematic compiled on a physical simulator and integrated with a Device Under Test (DUT). According to Typhoon Inc [99], the virtual simulator isn't merely an offline simulator; it replicates the functionality and limitations of a physical HIL simulator.

4.3.1 Virtual Setup

In the virtual setup, the directional element is emulated using the Typhoon schematic editor, with a virtual HIL603 simulator utilized [99]. The NSVP directional Logic of the relay is delineated as a flow chart in Fig.4.3. Symmetrical components of the

voltage and current measurements are extracted, and these symmetrical values serve as the basis for all subsequent calculations and comparisons. The NSVP directional element is activated by an enable logic (32QE), depicted in Fig.4.4, which incorporates a restraining factor to prioritize the activation of the NSVP directional element over the PSVP and ZSP directional elements. Following the successful initiation of NSVP, the negative sequence impedance is calculated using (4.11), and this calculated impedance is subsequently compared against forward and reverse thresholds to determine fault directionality, as illustrated in Fig. 4.5.

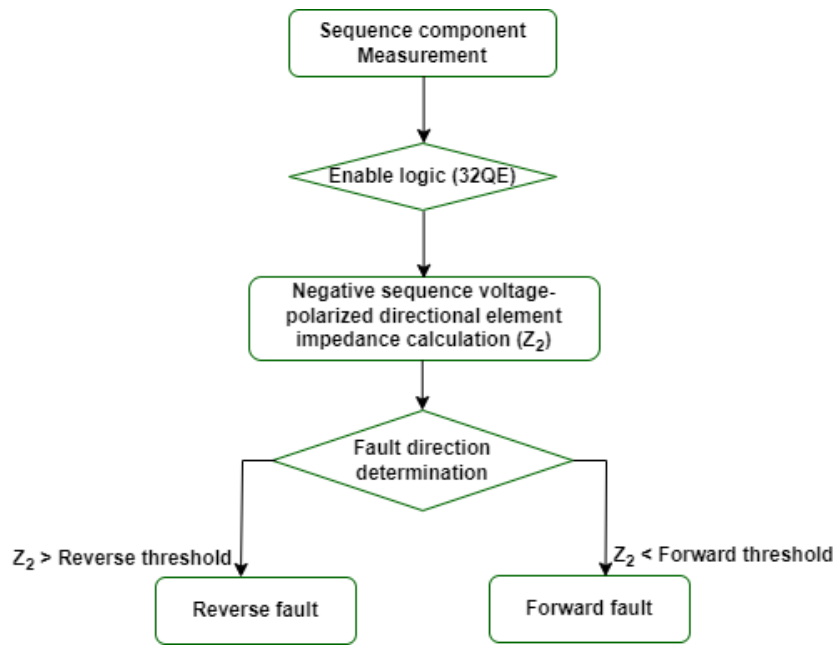


Figure 4.3: A flow chart of the NSVP directional element logic

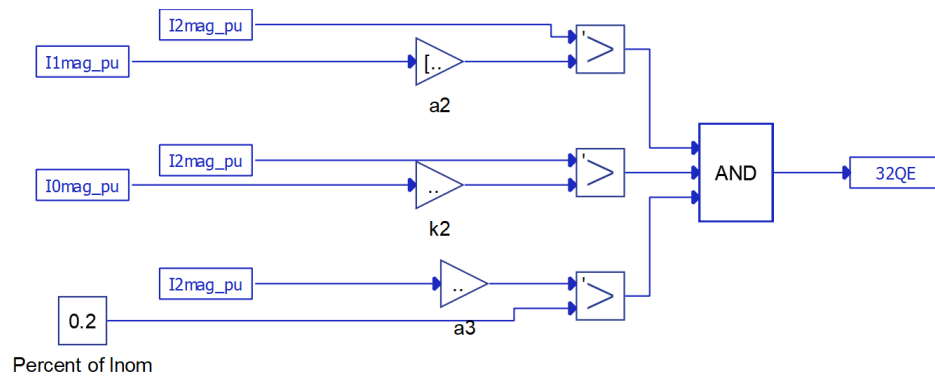


Figure 4.4: Block diagram of the enable logic (32QE)

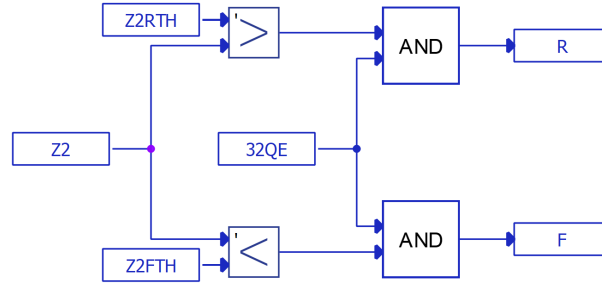


Figure 4.5: Block diagram of the fault direction determination

4.3.2 HIL Setup

The Real-time Hardware in the Loop (HIL) configuration, depicted in Fig. 4.6, consists of several components: a physical protection relay, which is the Service Under Test (DUT), a Typhoon HIL 603 simulator, a HIL device input/output Interface board, and associated software platforms comprising the schematic editor interface, the SCADA interface, relay configuration, and monitoring interface.

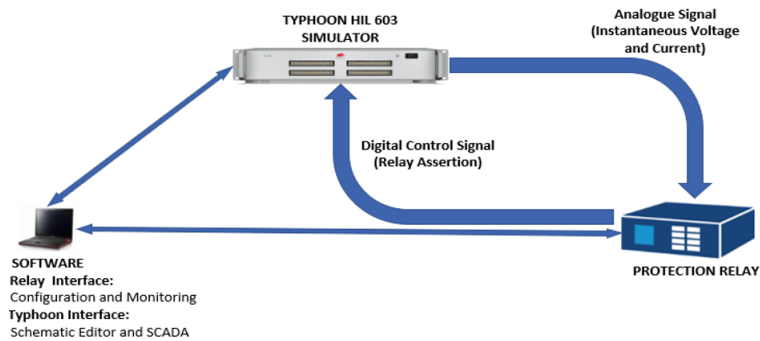


Figure 4.6: A simplified representation of the HIL real-time setup

The HIL 603 simulator is an intermediary between the virtual model within the software and the DUT. The test system, designed within the schematic editor interface, is compiled on the simulator, and input/output signals are configured through the software's SCADA interface. The digital signal (Trip and breaker status) and analog signal (voltage and current signals) are transmitted to the DUT via the input/output interface.

A TRIP logic is established on the DUT (physical protection relay) to detect over-

current directional faults (67). The 67 element asserts if directional Logic (32QR and 32QF) and phase overcurrent (50P) logic are asserted.

4.3.3 Description of Test System

The simulation was done on a modified IEEE 13 bus model. The modification includes the addition of node 676 and node 677, integrating DG at node 677, and removing the capacitor bank, as shown in Fig. 4.7. The distribution generator Point of Interconnection (POI) is at node 677. In addition, the load located after node 675 in the original IEEE 13 bus was instead distributed equally: half of the load is located before node 675, and the other half is after node 675.

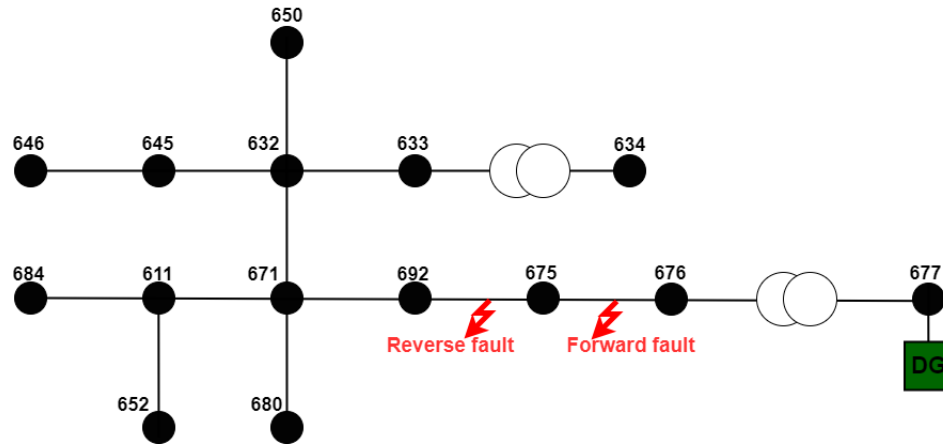


Figure 4.7: Modified IEEE 13-bus system

Regarding the protection configuration, the forward direction is oriented toward the IBDG, while the reverse direction is aimed away from the IBDG. A Single Line-to-Ground (SLG) fault is applied before and after node 675 for reverse and forward fault, respectively, as illustrated in Fig. 4.7.

Fig. 4.8 shows the IBDG grid side control block diagram; a 0.5MVA voltage source inverter was implemented, about 10% of the total network. As noted in chapter 3, IBDG fault characteristic is determined by Grid Side Control (GSC); Fig. 4.9 shows the model of the GSC. The measurement block includes a Phase-Locked Loop (PLL)

driven reactive power calculation, done by evaluating the fundamental positive sequence component of the POI voltage and current over a running window of one cycle. This eliminates the harmonic components and ensures the positive sequence drives the voltage control loop. The FRT was implemented with a dynamic volt-var control using the curve in Fig. 4.10.

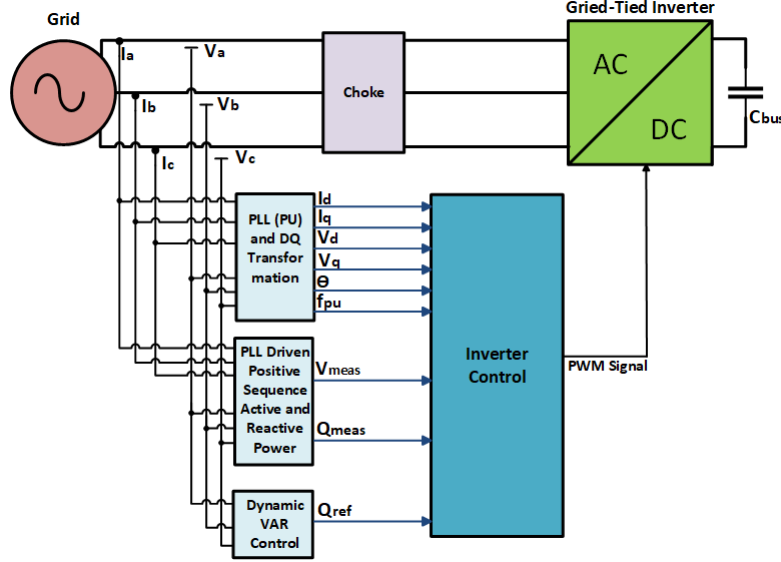


Figure 4.8: A simplified block diagram of IBDG grid side control

4.4 Results and Analysis

Forward and reverse SLG faults were simulated for an IBDG and synchronous-based distribution generator (SDG), the SDG is modeled as a voltage source. Node 675 is the node of interest for protection; hence its voltage and current were measured. The result presented for the virtual simulation is depicted on a SCADA interface; it displays the sequence component phasor, fault direction indicator, fault direction switch, the Minimum Torque Angle (MTA) value, and the phase waveform. The HIL real-time simulation results include the relay front panel and the Event Records (ER). The front panel displays the trip signal and other bit assertions, whereas the (ER) shows the relay bit that was asserted during the fault.

noted in section 4.2. In Fig. 4.12(a), the SCADA interface for a forward fault condition has been demonstrated, where I_2 leads V_2 . It signifies the current is in forward flow; the forward fault logic was activated. Figure 4.12(b) shows the measurement interface for a reverse fault condition. In this scenario, I_2 lags V_2 , which signifies a reverse flow, and the reverse fault logic was activated as expected.

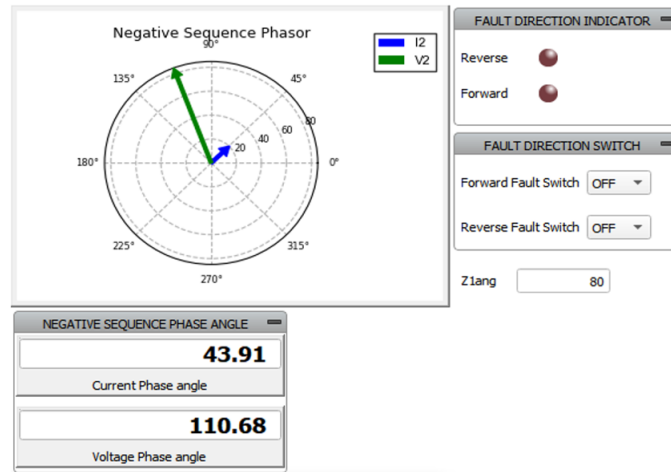


Figure 4.11: Virtual simulation SCADA interface for an SDG scenario: Normal operating condition

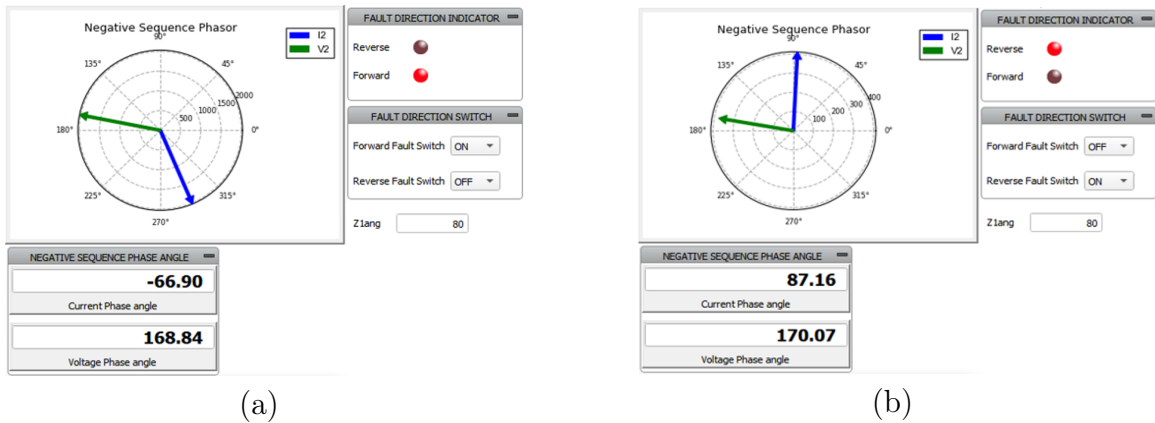


Figure 4.12: Virtual simulation SCADA interface for an SDG Scenario: (a) Forward fault condition, (b) Reverse fault condition

IBDG Virtual Simulation Results: Figure 4.13(a) is the SCADA interface for a forward fault condition; the measurement is the same as the SDG scenario in Fig. 4.12(b) because the direction of fault current in node 675 is only from the grid.

Fig. 4.13(b) shows the SCADA interface for a reverse fault condition; unlike the IBDG scenario, I_2 leads V_2 , causing the forward fault logic to be activated. This is a misbehavior because the measurement is forward-characterized, hence the forward fault logic was activated during a reverse fault condition.

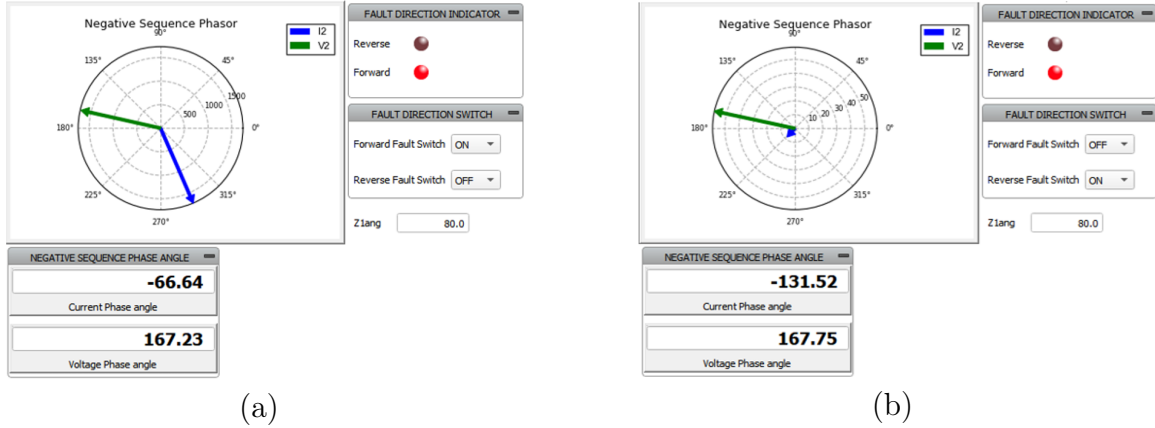


Figure 4.13: Virtual simulation SCADA Interface for an IBDG Scenario: (a) Forward fault condition, (b) Reverse fault condition

4.4.2 HIL Simulation: NSVP Misoperation

As described earlier, the HIL setup requires software, hardware simulators, and DUT. The relay front-panel display and Event Record (ER) indicate the logic asserted during fault and normal conditions. Similar to the virtual simulation, forward and reverse fault conditions are tested and analyzed when the protection relay is configured with forward (F32Q) and reverse direction (R32Q) settings.

SDG Forward Fault Condition: In this scenario, a forward fault is applied when a synchronous-based generator is integrated;

When the relay trip logic is configured with a forward element, the front panel in Fig. 4.14 reveals that a trip signal was asserted; this is because the trip logic was configured with a forward directional element, the ER in Fig. 4.15 also reveals that the forward direction element (F32Q) and the overcurrent directional element (67) was asserted.

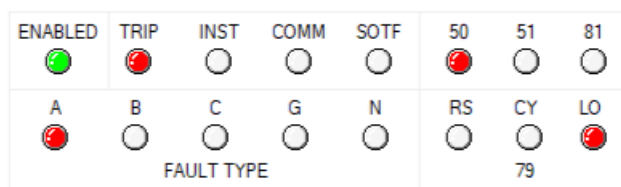


Figure 4.14: Front panel display: Forward directional element setting during forward fault - SDG scenario

FID=SEL-351-6-R516-V1-Z106105-D20170818				CID=296C	
#	Date	Time	Element	State	
6	07/03/20	20:27:16.611	SER archive cleared		
5	07/03/20	20:27:25.036	F32QG	Asserted	
4	07/03/20	20:27:25.036	F32Q	Asserted	
3	07/03/20	20:27:25.048	67P1	Asserted	
2	07/03/20	20:27:25.048	50P1	Asserted	
1	07/03/20	20:27:25.082	67P1T	Asserted	

Figure 4.15: Event record display: Forward directional element setting during forward fault - SDG scenario

However, when the relay trip logic is configured with a reverse element, the ER in Fig. 4.17 reveals that the overcurrent element (50P1) was asserted, and the forward directional element (F32Q) was asserted, but the trip logic was not asserted as shown in the front panel in Fig. 4.16 because it was configured to assert for a reverse fault; hence the relay configurations behaved as expected during forward fault condition in the presence of SDG.

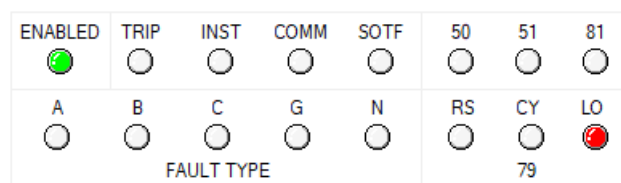


Figure 4.16: Front panel display: Reverse directional element setting during forward fault - SDG scenario

FID=SEL-351-6-R516-V1-Z106105-D20170818				CID=296C
#	Date	Time	Element	State
6	07/03/20	22:40:44.390	SER archive cleared	
5	07/03/20	22:41:21.088	32GF	Asserted
4	07/03/20	22:41:21.088	F32QG	Asserted
3	07/03/20	22:41:21.088	F32Q	Asserted
2	07/03/20	22:41:21.088	32NF	Asserted
1	07/03/20	22:41:21.100	50P1	Asserted

Figure 4.17: Event record display: Reverse directional element setting during forward fault - SDG scenario

SDG Reverse Fault Condition: In this scenario, a reverse fault is applied when a synchronous-based generator is integrated;

The front panel in Fig. 4.18 reveals that a trip signal was asserted; this is because the trip logic was configured with a reverse directional element; the ER in Fig. 4.19 also reveals that the reverse direction element (R32Q) and the overcurrent directional element (67) was asserted.

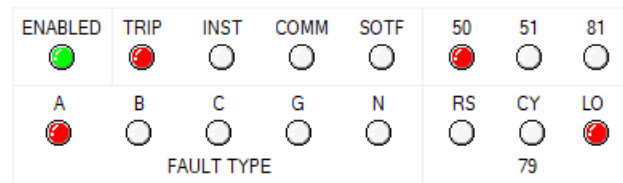


Figure 4.18: Front panel display: Reverse directional element setting during reverse fault - SDG scenario

However, when the relay trip logic is configured to operate during a forward fault, the ER in Fig. 11(d) reveals that the overcurrent element (50P1) was asserted. The reverse directional element (R32Q) was asserted, but the trip logic was not asserted as shown in the front panel in Fig.11(b) because it was configured to assert for a forward fault; hence the relay configurations behaved as expected during reverse fault condition in the presence of SDG.

However, when the relay trip logic is configured with a forward element, the ER in

FID=SEL-351-6-R516-V1-Z106105-D20170818				CID=296C
#	Date	Time	Element	State
7	07/03/20	22:32:28.704	SER archive cleared	
6	07/03/20	22:32:38.112	F32P	Deasserted
5	07/03/20	22:32:38.116	R32QG	Asserted
4	07/03/20	22:32:38.116	R32Q	Asserted
3	07/03/20	22:32:38.120	67P1	Asserted
2	07/03/20	22:32:38.120	50P1	Asserted
1	07/03/20	22:32:38.154	67P1T	Asserted

Figure 4.19: Event record display: Reverse directional element setting during reverse fault - SDG scenario

Fig. 4.21 reveals that the overcurrent element (50P1) was asserted, and the reverse directional element (R32Q) was asserted, but The trip logic was not asserted as shown in the front panel in Fig. 4.20 because it was configured to assert for a reverse fault; hence the relay configurations behaved as expected during reverse fault condition in the presence of SDG.

















ENABLED	TRIP	INST	COMM	SOTF	50	51	81
							
A	B	C	G	N	RS	CY	LO
							
FAULT TYPE					79		

Figure 4.20: Front panel display: Forward directional element setting during reverse fault - SDG scenario

FID=SEL-351-6-R516-V1-Z106105-D20170818				CID=296C
#	Date	Time	Element	State
4	07/03/20	20:44:29.143	SER archive cleared	
3	07/03/20	20:44:46.121	R32QG	Asserted
2	07/03/20	20:44:46.121	R32Q	Asserted
1	07/03/20	20:44:46.125	50P1	Asserted

Figure 4.21: Event record display: Forward directional element setting during reverse fault - SDG scenario

IBDG Reverse Fault Condition: The forward fault condition for the IBDG scenario is the same as the SDG scenario. Hence, the IBDG forward fault condition will not be discussed. In a reverse fault condition scenario, a reverse fault is applied when an inverter-based generator is integrated; Note that the logic of interest is the direction element logic(32Q)

When the relay trip logic is configured with reverse direction settings, the front panel in Fig. 4.22 shows that a trip signal was not asserted. The ER in Fig. 4.23 shows that the reverse directional element (R32Q) was de-asserted while a forward directional element (F32Q) was asserted during a reverse fault condition. This is a misoperation as it mistakes a reverse direction fault for a forward fault. Hence, the mis-operation experienced during the virtual simulation was replicated in the HIL real-time simulation.

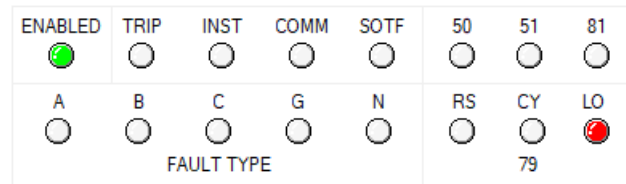


Figure 4.22: Front panel display: Reverse directional element setting during reverse fault - IBDG scenario

=SEL-351-6-R516-V1-Z106105-D20170818			CID=296C
Date	Time	Element	State
07/03/20	22:13:20.295	SER archive cleared	
07/03/20	22:13:22.170	R32QG	Deasserted
07/03/20	22:13:22.170	R32Q	Deasserted
07/03/20	22:13:22.174	32GF	Asserted
07/03/20	22:13:22.174	F32QG	Asserted
07/03/20	22:13:22.174	F32Q	Asserted
07/03/20	22:13:22.174	F32P	Asserted
07/03/20	22:13:22.174	32NF	Asserted

Figure 4.23: Event record display: Reverse directional element setting during reverse fault - IBDG scenario

It is worth noting that the overcurrent element (50P) and the directional overcurrent

(67) were not of interest as the direction element is the goal of this study. The 50P and 67 elements were not asserted due to the limited fault contribution of the IBDG. The results from both virtual and HIL simulations are consistent; the directional element performs well for synchronous distributed generators and misoperated for inverter generators. The main reason for the misoperation is the deviation of the IBDG fault characteristics from the conventional synchronous generator. During a reverse fault condition, The negative sequence current contribution of the IBDG leads to the negative sequence voltage (capacitive characteristics), a characteristic specific to forward fault conditions. In reverse fault conditions, the negative sequence component is expected to be inductive, i.e., the current should lag the voltage by an angle between 10° and 90° .

4.4.3 NSVP prevention Approach (Virtual and HIL Simulation)

Identifying the cause of the misoperation as the angular difference between the current and voltage sequence components provides insight into the required modification of the parameters of the protection scheme to ensure that it can operate normally in the presence of IBDG. As noted in Fig yy, (I_2) leads (V_2) by approximately 62° . the impedance phase angle $(\angle Z_{line})$ which is the MTA value, was configured as a conventional inductive line with $\angle Z_{line}$ or MTA value of 90° . substitute the values in (4.11) yield a negative Z_2 value as shown in (4.12), which is a characteristic of forward fault:

$$\cos(62^\circ + 90^\circ) = -0.883 \quad (4.12)$$

To prevent misoperation, it's essential for the Z_2 value to have a positive sign during the reverse operation of the directional element. This can be accomplished by ensuring that the sign of $\cos(\angle Z_{line} - \Theta)$ is positive, which occurs when $(\angle Z_{line} - \Theta)$ lies in

the first or fourth Cartesian plane where cosine is always positive.

Modifying the setting configuration by biasing the MTA ($\angle Z_{line}$) to reduce the value from 90° to a value that will result in a positive value, thus leading to the proper operation of the direction element. setting the value of the MTA to less than 28° will result in a positive Z_2 shown in (4.13) which is a viable solution:

$$\cos(62^\circ + 25^\circ) = +0.052 \quad (4.13)$$

Simulation results confirmed the effectiveness of this prevention measure; the MTA (Z_{1ang}) is configured to 15° . Figure 4.24 is the SCADA interface showing the proper operation of the directional element after modifying the MTA (Z_{1ang}) to 15° . As shown in the SCADA interface, the forward and reverse directional elements operated reliably for forward and reverse faults accordingly in Fig. 4.24(a) and Fig. 4.24(b), respectively.

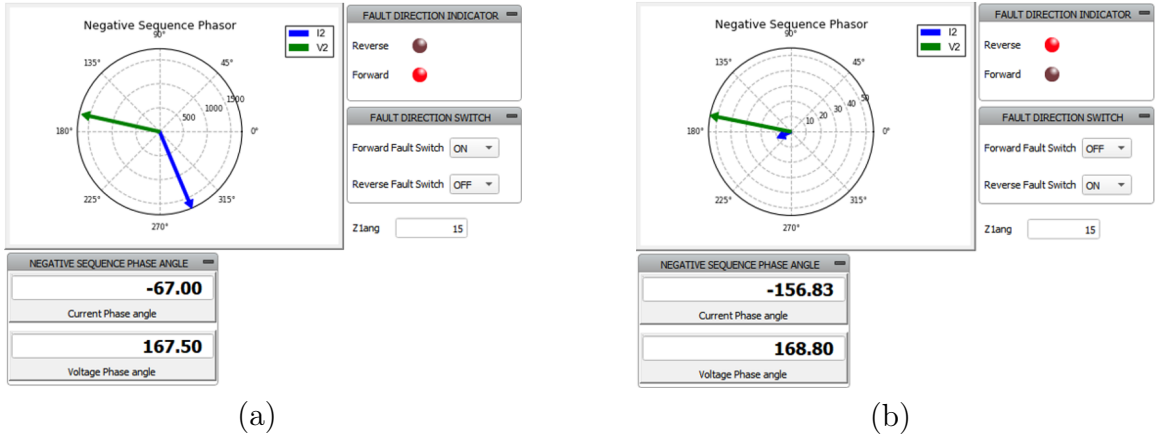


Figure 4.24: prevention approach validation: Virtual simulation SCADA interface for an IBDG scenario: (a) Forward fault condition, (b) Reverse fault condition

Similarly, the event record shows that the forward element ($F32Q$) and the reverse element ($R32Q$) asserted for forward and reverse faults accordingly in Fig. 4.25 and Fig. 4.26, respectively.

SEL-351-6-R516-V1-Z106105-D20170818			CID=296C
Date	Time	Element	State
07/03/20	20:27:16.611	SER archive cleared	
07/03/20	20:27:25.036	F32QG	Asserted
07/03/20	20:27:25.036	F32Q	Asserted
07/03/20	20:27:25.048	67P1	Asserted
07/03/20	20:27:25.048	50P1	Asserted
07/03/20	20:27:25.082	67P1T	Asserted

Figure 4.25: prevention approach validation: Event record display for forward directional element setting during forward fault - IBDG scenario

SEL-351-6-R516-V1-Z106105-D20170818			CID=296C
Date	Time	Element	State
07/03/20	20:44:29.143	SER archive cleared	
07/03/20	20:44:46.121	R32QG	Asserted
07/03/20	20:44:46.121	R32Q	Asserted
07/03/20	20:44:46.125	50P1	Asserted

Figure 4.26: prevention approach validation: Event record display for reverse directional element setting during reverse fault - IBDG scenario

4.5 Conclusion

The findings validate the misoperation of the NSVP directional scheme in the presence of IBDG. This misoperation is attributed to the fault characteristics of the IBDG during fault conditions, which deviate from the conventional fault characteristics. Specifically, the negative sequence current of the IBDG leads to the negative sequence voltage during reverse faults, contradicting the expected behavior for conventional synchronous distributed generators (SDGs). As a result, the directionality of the NSVP scheme is affected, as it is tailored for conventional SDGs where the negative sequence current typically lags the negative sequence voltage during reverse faults. The proposed prevention strategy involves adjusting the MTA of the NSVP directional element, effectively preventing misoperation in the presence of IBDGs.

In addition, the proposed solution approach was validated considering bolted faults; it is important to highlight that while this solution is effective for non-bolted faults, the maximum MTA for bolted faults is lower than for non-bolted faults due to the

higher resistive nature of non-bolted faults.

Considering that directional elements are used to supervise other protection elements, they pose a significant risk to the reliability of the power system if they misoperate, while specific schemes, such as communication-based solutions and differential schemes, do not require directional elements and are immune to these fault characteristics, they tend to be considerably more costly compared to schemes that utilize directional elements.

The adopted solution approach modifies the protection element setting; further research should prioritize enhancing inverter controllers to emulate the fault characteristics of conventional synchronous generators. Moreover, protection engineers and inverter manufacturers must collaborate to establish a standardized control architecture for IBDGs that will work with conventional protection schemes. This joint endeavor will play a pivotal role in ensuring grid protection and, consequently, the seamless integration of IBDGs, which is crucial for grid modernization efforts.

CHAPTER 5: ENHANCED PROTECTION COORDINATION APPROACH: A COMPARATIVE ANALYSIS

Given the evolving nature of power grids towards greater decentralization and interconnectedness, an efficient protection coordination approach is necessary to uphold overall system reliability. Such coordination of overcurrent relays can be realized through graphical methods, numerical iteration techniques like Newton-Raphson or gradient descent, and optimization approaches. The coordination aims to minimize the operating time of protective devices while ensuring seamless coordination among them. An effective relay coordination approach enhances system reliability, maintains continuity of service to customers, and prevents cascading failures by ensuring that protective devices operate selectively and cohesively to isolate faults while minimizing unnecessary tripping of healthy system components. As the grid transitions towards a network of microgrids and nanogrids, the performance evaluation of diverse protection coordination strategies becomes paramount.

5.1 Main Contribution

The transition towards a more dynamic grid, characterized by bidirectional power flow, underscores the significance of Directional Overcurrent Relay (DOCR) schemes. By discerning fault direction, DOCRs play a pivotal role in reducing customer outages. Consequently, the coordination of DOCRs must be managed to achieve the desired levels of reliability and selectivity. This chapter focuses on the performances of the coordinating approaches of DOCRs. An enhanced Particle Swarm Optimization (PSO) is developed to improve protection coordination outcomes, and the work is conducted on two test systems. The investigation and outcomes of this chapter

were published in 2023 at the Texas Power and Energy Conference (TPEC) [100], and the contributions are as follows:

- Presented an enhanced PSO algorithm for DOCR coordination
- Validated the superiority of the enhanced PSO algorithm against different coordination approaches: numerical iteration, Genetic Algorithm (GA), and conventional PSO
- Implemented three variations of the PSO coordination approach; the performance of the three variations is based on total operating time and CTI

5.2 Overview and Methodology

This section describes the protection coordination formulation for Directional Over-current Relays (DOCR) and discusses the coordination approaches, including numerical iteration, Genetic Algorithms (GA), and Particle Swarm Optimization (PSO).

5.2.1 Protection Coordination Formulation

Coordination of protective devices involves configuring appropriate operating characteristics and response times for devices such as relays, circuit breakers, fuses, and other protective elements to minimize the system outage. The protection device nearest to the fault zone operates faster than other protection farther away.

The DOCR can be configured to operate in three ways: instantaneous operation when the line current exceeds a threshold value, operation of the relay after a predetermined time when the line current exceeds a threshold value, and the operation of the relay based on an inverse-time current relationship, this operational feature aids in DOCR coordination. Equations (5.1) and (5.2) describe the inverse-time current relationship of DOCRs for the IEC standard and US standard, respectively. $t_{op}^{(j,i)}$ is the operating time of primary relay j for a fault in zone i , TDS^j is the Time Dial Setting for relay j , A , B , and β are set of constants that determine the curve types, there are five types

of curve for both IEC standard and US standard [101] as shown in Table 5.1 and Table 5.2. The very inverse curve in the U.S. standard is used for the coordination study in this chapter.

$$t_{op}^{(j,i)} = TDS^j \times \left(B + \frac{A}{\left(\frac{I_f}{I_p}\right)^\beta - 1} \right) \quad (5.1)$$

$$t_{op}^{(j,i)} = TDS^j \times \left(\frac{A}{\left(\frac{I_f}{I_p}\right)^\beta - 1} \right) \quad (5.2)$$

Table 5.1: IEC Inverse-Time Current Curve (TCC) Equation Parameters

Curve Type	β	A
Standard Inverse	0.02	0.14
Very Inverse	1	13.5
Extremely Inverse	2	80
Long-Time Inverse	1	120
Short -Time Inverse	0.04	0.05

Table 5.2: U.S. Inverse-Time Current Curve (TCC) equation parameters

Curve Type	β	A	B
Moderately Inverse	0.02	0.0104	0.0226
Inverse	2	5.95	0.18
Very Inverse	2	3.88	0.0963
Extremely Inverse	2	5.64	0.0243
Short-Time Inverse	0.02	0.00342	0.00262

In power system protection, each protection zone is protected by a coordination pair of relays consisting of a primary and backup protection relay. The primary protection relay is positioned closest to the Zone of Protection (ZOP) and is designed to operate faster than the backup protection relays. The duration between the operation of the primary and backup relays is termed the Coordination Time Interval (CTI), which is typically within the range of 0.2 to 0.5 seconds [102] to accommodate factors such as circuit breaker delays, transducer errors, and relay safety margins. To achieve optimal

coordination, two objectives must be met: firstly, ensuring that each relay operates within the shortest possible time frame as shown in (5.3), and secondly, ensuring that the coordination interval is not less than the minimum CTI value as shown in (5.4),

$$\min \sum T_{pr} = \min \left(\sum_{i=1}^{\varphi} \sum_{j=1}^{\phi} t_{op}^{(j,i)} \right) \quad (5.3)$$

$$t_{bc}^i - t_{pr}^i \geq CTI \quad (5.4)$$

Where:

T_{pr} : Total operating time of all the relays

$t_{op}^{(j,i)}$: Operating of each relay j for a i – th fault zone

φ : Number of fault zones

ϕ : Number of relays

t_{bc} : Backup operating time of fault zone i backup protection relay

t_{pr} : Primary operating time of fault zone i primary protection relay

The conventional approach to protection coordination commonly employed in the industry is the graphing method, where the pickup current and TDS are obtained by graphically tracing the time-current curve. However, the methodologies proposed in this paper use the inverse-time current equations to calculate the pickup current and TDS.

5.2.2 Numerical Iteration Method

The Gauss-Seidel iterative method is employed in this study to address the coordination problem, wherein variables are iteratively updated with the latest values. The coordination problem is formulated as a linear equation, as detailed in (5.5) In this formulation, the only variable to solve for is the Time Dial Setting of relay j

$(TDS_{pr}^j(x))$ which is updated every $x - th$ iteration, while the relay pickup currents are predefined by multiplying the nominal current by a factor of 1.25. The constant $K_{I_f^i I_p}^j$ remains fixed for each iteration x , and it is a function of the pickup current and fault current for fault at zone i (primary and backup fault current) of each relay as described by (5.6).

$$t_{pr}^j(x) = TDS_{pr}^j(x) \times K_{I_f^i I_p}^j \quad (5.5)$$

$$K_{I_f^i I_p}^j = \left(B + \frac{A}{\left(\frac{I_f^i}{I_p} \right)^\beta - 1} \right) \quad (5.6)$$

Below is the description of the pseudocode for numerical iteration. This process is repeated for each iteration. However, only the first iteration necessitates initialization; subsequent iterations utilize the values from the most recent iteration.

Iteration 1: (x=1)

Relay j

- * Select a starting relay j
- * Determine the load current and the minimum fault current seen by relay j
- * Calculate the pickup current of relay j (I_p^j) by multiplying the nominal current seen by relay j by a factor of 1.25 ($1.25 \times I_{nom}^j$)
- * Initialize a value for the Time Dial Setting of relay j ($TDS_{pr}^j(x)$)
- * Calculate the primary operating time of relay j ($t_{pr}^j(x)$) using the initialized TDS

Relay j-1

- * Calculate the backup operating time of relay $j - 1$ using ($t_{pr}^{j-1}(x)$) with ($t_{bc}^{j-1}(x) = t_{pr}^j(x) + CTI$), where CTI is a predetermined constant.

- * Calculate the TDS of relay $j - 1$ using $(TDS_{bc}^{j-1}(x) = \frac{t_{bc}^{j-1}(x)}{K_{(If_{bc}I_p)}^{j-1}})$.
- * Calculate the primary operating time of relay $j - 1$ ($t_{pr}^{j-1}(x)$) using the newly calculated TDS ($TDS_{bc}^{j-1}(x)$).

Relay j-2

- * Calculate the backup operating time of relay $j - 2$ using $(t_{pr}^{j-2}(x))$ with $(t_{bc}^{j-2}(x) = t_{pr}^{j-1}(x) + CTI)$, where CTI is a predetermined constant.
- * Calculate the TDS of relay $j - 2$ using $(TDS_{bc}^{j-2}(x) = \frac{t_{bc}^{j-2}(x)}{K_{(If_{bc}I_p)}^{j-2}})$.
- * Calculate the primary operating time of relay $j - 2$ ($t_{pr}^{j-2}(x)$) using the newly calculated TDS ($TDS_{bc}^{j-2}(x)$).

Relay j-3

.

.

Relay J-($\phi + 1$)

Relay J-(ϕ)

- * Calculate the backup operating time of relay $j - \phi$ using $(t_{pr}^{j-\phi}(x))$ with $(t_{bc}^{j-\phi}(x) = t_{pr}^{j+\phi+1}(x) + CTI)$, where CTI is a predetermined constant.
- * Calculate the TDS of relay $j - \phi$ using $(TDS_{bc}^{j-\phi}(x) = \frac{t_{bc}^{j-\phi}(x)}{K_{(If_{bc}I_p)}^{j-\phi}})$.
- * Calculate the primary operating time of relay $j - \phi$ ($t_{pr}^{j-\phi}(x)$) using the newly calculated TDS ($TDS_{bc}^{j-\phi}(x)$).

Iteration 2: (x=2)

Relay j

- * Calculate the backup operating time of relay j using $(t_{pr}^j(x))$ with $(t_{bc}^j(x) = t_{pr}^\phi(x) + CTI)$, where CTI is a predetermined constant.
- * Calculate the TDS of relay j using $(TDS_{bc}^j(x) = \frac{t_{bc}^j(x)}{K_{(If_{bc}I_p)}^j})$.

- * Calculate the primary operating time of relay j ($t_{pr}^j(x)$) using the newly calculated TDS ($TDS_{bc}^j(x)$).

The convergence criteria are:

Convergence criteria A: Number of iterations (x) > maximum number of iterations

Convergence criteria B: Check if the magnitude of ($t_{pr}^j(x-1) - t_{pr}^j(x)$) < tolerance value

In summary, Equation (5.7) through (5.9) are utilized to compute both the TDS and the operating time of the relays for each iteration in the pseudocode.

$$t_{pr}^j(x) = TDS_{pr}^j(x) \times K_{I_{pr}^j I_p}^j \quad (5.7)$$

$$t_{bc}^{j-1}(x) = t_{pr}^j(x) + CTI \quad (5.8)$$

$$TDS_{bc}^{j-1}(x) = \frac{t_{bc}^{j-1}(x)}{K_{(If_{bc} I_p)}^{j-1}} \quad (5.9)$$

5.2.3 Optimization Algorithms

The objective is to minimize the relay's operating time (T_{pr}) with a CTI equality constraint while ensuring that the TDS , pickup current (I_p), and operating time are constrained by predefined limits. Equation (5.10) describes the objective function while (5.11) through (5.15) are the constraints. The results of the Genetic Algorithm (GA) and Particle Swarm Optimization (PSO) are compared in this chapter.

$$\min \sum T_{pr} = \min \sum_{i=1}^{\varphi} \sum_{j=1}^{\phi} t_{pr}^{j,i} \quad (5.10)$$

$$t_{bc} - t_{pr} \geq CTI \quad (5.11)$$

$$TDS_{min} \leq TDS^j \leq TDS_{max} \quad (5.12)$$

$$I_{pmin} \leq I_p^j \leq I_{pmax} \quad (5.13)$$

$$t_{min} \leq t_{pr}^{j,i} \leq t_{max} \quad (5.14)$$

$$t_{min} \leq t_{bc}^{j,i} \leq t_{max} \quad (5.15)$$

Genetic Algorithm: A Genetic Algorithm (GA) is a population-based metaheuristic optimization technique inspired by natural selection and genetics principles. In a GA, the variables are typically represented as chromosomes, which evolve over successive generations. Through the process of selection, crossover, and mutation, individuals with better fitness (i.e., optimal objective function) are more likely to survive and produce offspring, gradually improving the overall population. A typical flowchart of GA is shown in Fig. 5.1; the parameters include population size, crossover rate and method, mutation rate and method, and selection method.

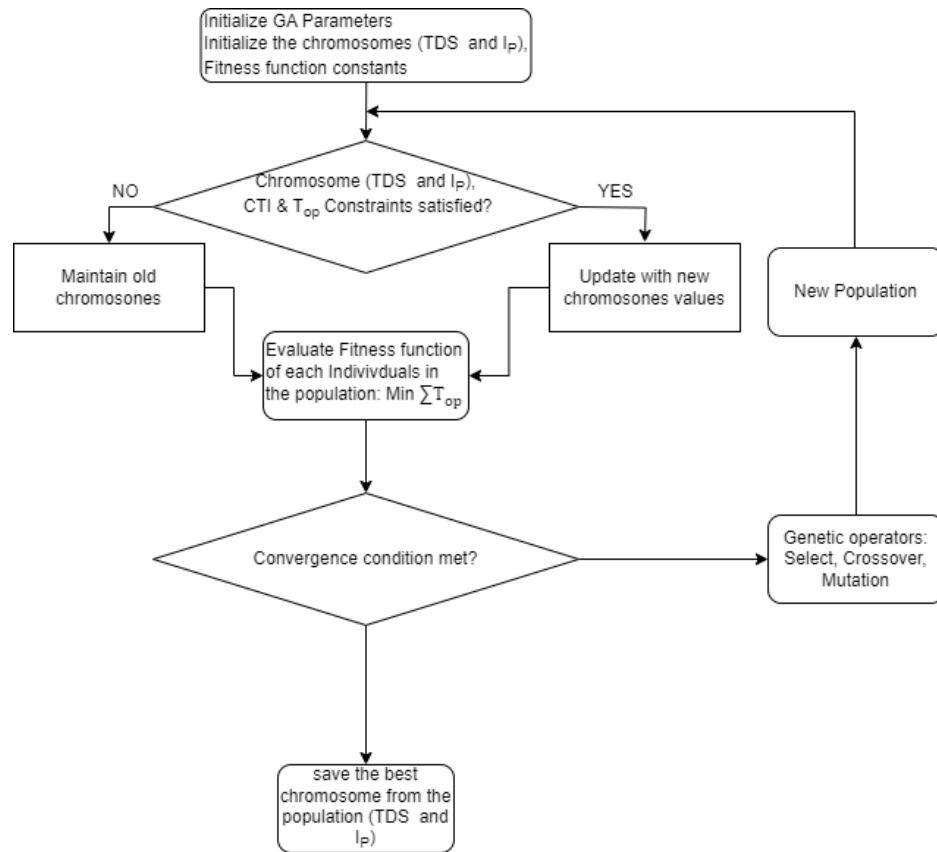


Figure 5.1: A flowchart of genetic algorithm

Particle Swarm Optimization: Similarly to GA, Particle Swarm Optimization (PSO) is a population-based metaheuristic optimization algorithm inspired by animal biological behavior. It emulates animal swarming, such as a flock of birds searching for food. In a swarm, individual movement in the search space is influenced by individual and group intelligence. Figure 5.2 is a flowchart of the PSO.

Equations (5.16) and (5.17) are the major components of the algorithm, the constant c_p and c_g are the acceleration that pushes the particle towards the individual best position and the group best position respectively. To increase the global convergence solution, the social acceleration coefficient c_g will be decreased linearly during the iteration using (5.18). Similarly to global acceleration, the value of inertia weight is modified to improve the algorithm's explorative and exploitative search ability. It has been shown that it is best to use an inertia weight between 0.9 and 0.4 [103].

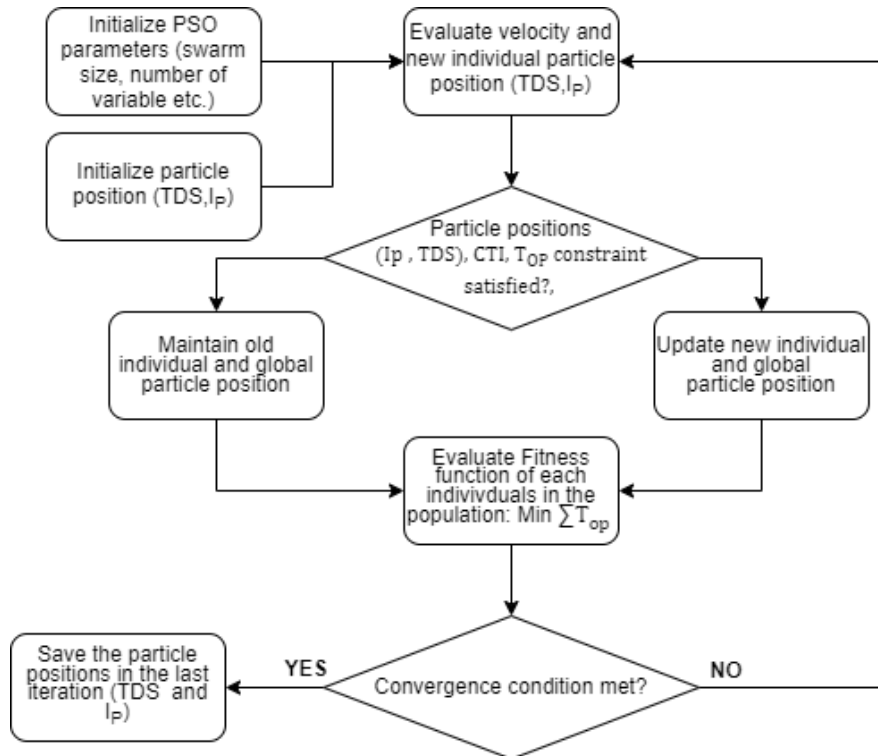


Figure 5.2: A flowchart of particle swarm optimization

$$v_n^{(i+1)} = \omega_1^i \times v_n^i + (c_P \times r_p \times (P_{nbest}^i - x_n^i) + C_g^i \times r_g \times (g_{nbest}^i - x_n^i)) \quad (5.16)$$

$$x_n^{i+1} = x_n^i + v_n^{i+1} \quad (5.17)$$

$$C_g^i = 0.8 - (0.5/\maxiters)i \quad (5.18)$$

Where:

$v_n^{(i+1)}$: Velocity of particle n at $(i + 1)th$ iteration

ω^i : Inertial weight of velocity at iteration i

v_n^i : Velocity of particle n at ith iteration

c_P : Cognitive acceleration coefficients

c_g : Social acceleration coefficients

r_P and r_g : Random numbers sampled from a uniform distribution

P_{nbest}^i : Individual best position of particle n with respect to its position at ith iteration

g_{best}^i : Global best position with respect to its position at ith iteration

x_n : Position of particle n at ith iteration

To further improve the performance of PSO, three variations of inertia weight described in (5.19) were used: Constant Inertia Weight (CIW-PSO) value of 0.5, linear Inertia Weight (LIW-PSO), which decreases the velocity linearly from 0.9, and Exponential Inertia Weight (EIW-PSO) which exponentially decrease the value from 0.9. The EIW-PSO is expected to perform better than the LIW-PSO variation because EIW-PSO has a higher value of inertia weight at latter iterations, as shown in Fig. 5.3, making it explore more solution search space to obtain a global solution.

$$\omega^i = \begin{cases} CIW = 0.5 & \text{if } i = 0 \\ LIW = 0.9 - \frac{0.5}{\max_{itera}} \times i & \text{if } 0 < i < \max_{itera} \\ EIW = 0.82 \times \left(e^{-\frac{i}{\max_{itera}}} \right) + 0.20 & \text{otherwise} \end{cases} \quad (5.19)$$

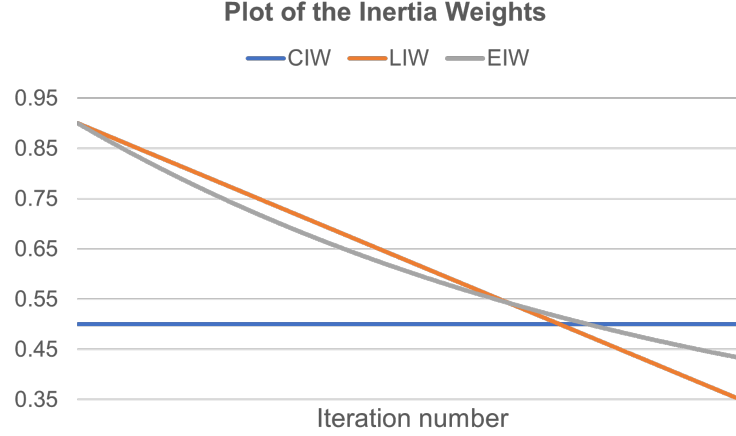


Figure 5.3: Plot of three variations of inertia weight

5.3 Result and Analysis

The methodologies presented in section 5.2 were validated using two test systems simulated on a typhoon virtual Hardware-in-the-Loop (HIL) simulator. Nominal power flow and short circuit simulations were conducted to obtain the nominal load current and short-circuit current, respectively. Additionally, a model of the Directional Overcurrent Relay (DOCR) was created within the virtual HIL simulator. The performance criterion for comparing the three methodologies - numerical iteration, GA, and PSO is the total operational time of both primary and backup relays.

5.3.1 Description of Test System

The research study used two test systems: a 9-bus test system and a modified IEEE 33-bus system. Figure 5.4 illustrates the 9-bus system microgrid, a 24.9kV radial system comprising two DGs located at buses 6 and 9. The rating of each DG is 10 MVA,

with a total load of 15.4 MVA. Each branch is protected by both forward and reverse relays, as depicted in Fig. 5.4. The forward protection relays at bus n are denoted as F_n , while the reverse protection relays at bus n are labeled as R_n in Fig. 5.4. The test system comprises 18 relays and 18 pairs of coordinated relays, as depicted in Table 5.3, including the fault current seen by the primary and backup protection relay. The nominal current of the 9-bus system is presented in Appendix A.1.

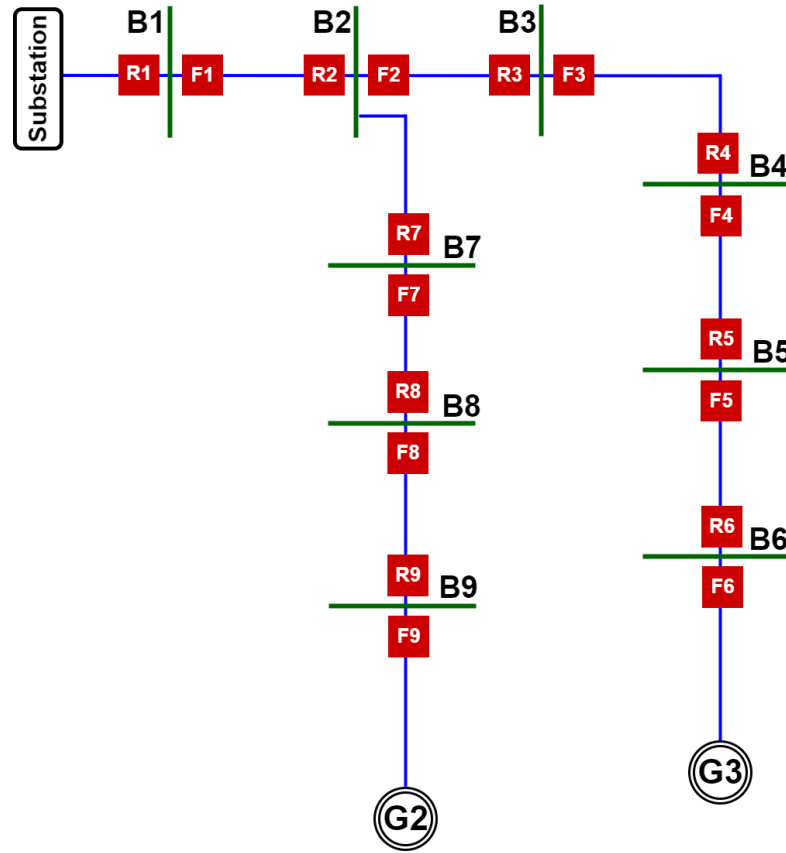


Figure 5.4: 9-bus system: A single line diagram

Figure 5.5 is the modified IEEE 33-bus system used for this study; it is a 12.15kV system comprising one 2MVA DG located at bus 29. Each branch is protected by both forward and reverse relays, as depicted in fig. 5.5. The forward protection relays at bus n are denoted as F_n , while the reverse protection relays at bus n are labeled as R_n in Fig. 5.5. The test system comprises 32 relays and 36 pairs of coordinated relays, as depicted in Table 5.4, including the fault current seen by the primary and

Table 5.3: 9-Bus System: Relay Coordination Pairs and Fault Current Characteristics

Relay Coordination Pair number	Primary Protection		Backup Protection	
	Relay	Fault Current (A)	Relay	Fault Current (A)
Pair 1	F1	1978	F2	2605
Pair 2	F2	1425	F3	1365
Pair 3	F3	1000	F4	880
Pair 4	F4	839	F5	812
Pair 5	F5	812	F6	798
Pair 6	F1	1978	F7	2530
Pair 7	R2	624	F7	2530
Pair 8	F7	1633	F8	1616
Pair 9	F8	1616	F9	1578
Pair 10	R7	903	F2	2605
Pair 11	R2	624	R1	1620
Pair 12	R3	660	R2	624
Pair 13	R4	868	R3	839
Pair 14	R5	1155	R4	1091
Pair 15	R6	2016	R5	1981
Pair 16	R7	1108	R1	1620
Pair 17	R8	1501	R7	1479
Pair 18	R9	1943	R8	1851

backup protection relay. The nominal current of the 33-bus system is presented in Appendix A.6

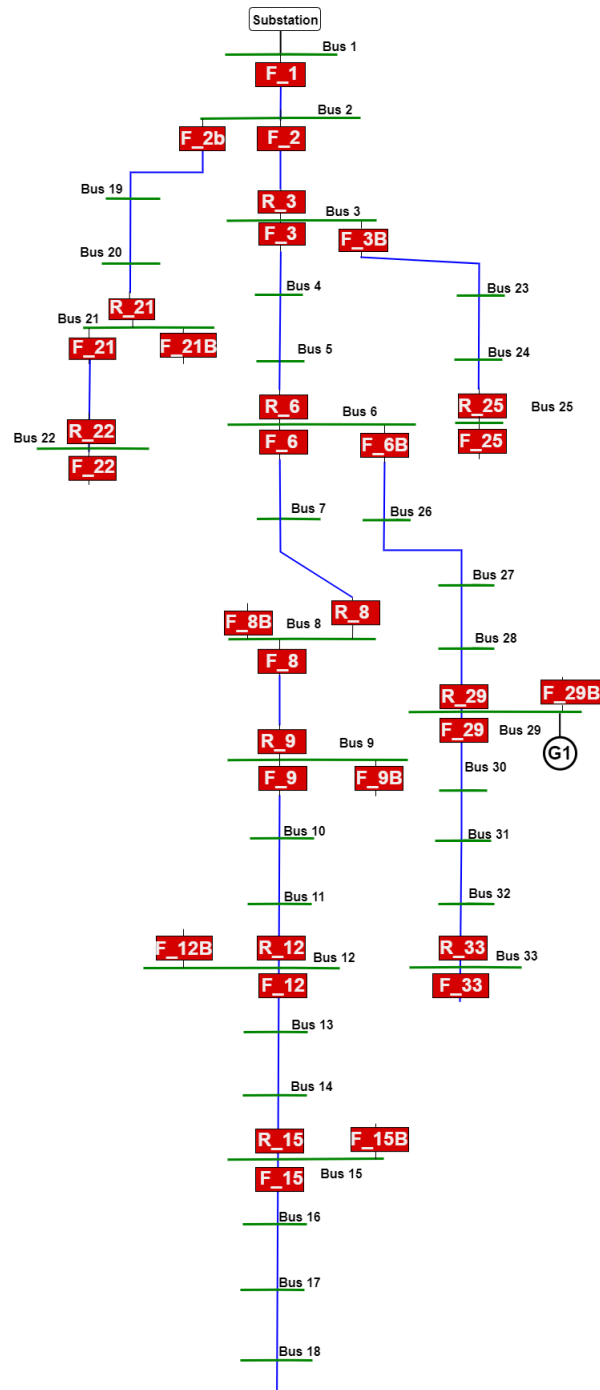


Figure 5.5: Modified IEEE 33-bus system: A single line diagram

5.3.2 Result and Analysis for 9-Bus System

The initial comparison involves numerical iteration, Genetic Algorithm (GA), and Constant Inertia Weight-Particle Swarm Optimization (CIW-PSO), while the subse-

Table 5.4: IEEE-33-Bus System: Relay Coordination Pairs and Fault Current Characteristics

Relay Coordination Pair number	Primary Protection		Backup Protection	
	Relay	Fault Current (A)	Relay	Fault Current (A)
Pair 1	F2	70583.89	F1	70610.08
Pair 2	F2	70583.89	R21	83.91
Pair 3	R3	165.00	R6	166.00
Pair 4	F3	10991.36	F2	10991.28
Pair 5	R6	830.50	R29	204.90
Pair 6	R6	830.50	R8	680.00
Pair 7	F6	3098.00	F3	2780.00
Pair 8	F6	3098.00	R29	334.80
Pair 9	R8	1048.20	R9	254.90
Pair 10	F8	2890.00	F6	1883.00
Pair 11	R9	460.12	R12	460.96
Pair 12	F9	1737.25	F8	1737.25
Pair 13	R12	767.00	R15	166.00
Pair 14	F12	1966.50	F9	1043.60
Pair 15	F15	944.30	F12	945.60
Pair 16	F33	501.00	F29	521.80
Pair 17	F3B	11756.41	R6	830.40
Pair 18	F3B	11756.41	F2	10991.57
Pair 19	F25	2106.40	F3B	2115.50
Pair 20	F29B	2000.00	F6B	1400.00
Pair 21	F29B	2000.00	R33	369.80
Pair 22	F6B	3802.00	F3	2780.74
Pair 23	F6B	3802.00	R8	1050.00
Pair 24	R29	341.00	R33	105.12
Pair 25	F29	1622.00	F6B	1383.27
Pair 26	F15B	1442.00	F12	946.00
Pair 27	F9B	2503.00	F8	1737.00
Pair 28	F9B	2503.00	R12	766.00
Pair 29	F2B	70733.88	F1	70577.13
Pair 30	F2B	70733.88	R3	161.31
Pair 31	F21	3283.00	F2B	2418.01
Pair 32	F12B	416.00	F9	257.80
Pair 33	F12B	416.00	R15	166.00
Pair 34	F21B	2832.00	F2B	2418.01
Pair 35	F8B	866.35	F6	1132.10
Pair 36	F8B	866.35	R9	254.90

quent comparison focuses on three different versions of Particle Swarm Optimization. As detailed in section 5.2, these methodologies yield solutions in the form of Time Dial Settings (TDS) and Pickup current (I_p), which are subsequently utilized to calculate the relay operating time and CTI. The TDS and I_p values obtained from the numerical iteration, GA, and the three PSO variations are presented in Appendix A.2 and A.3

Table 5.5 illustrates the performance of the numerical iteration, GA, and CIW-PSO for the 9-bus system; the performance is based on CTI, minimum total operating time for the primary (*PR Time*), and backup (*BR Time*) relays. In the numerical iteration approach, the relay operating time is 5.524s and 16.286s for both primary (*PR*) and backup (*BR*) protection relays, respectively, higher than that achieved by the GA and the 3 PSO variations. However, the CIW-PSO method demonstrates a lower total operating time compared to GA, and the computational time and convergence rate of GA were consistently higher over 25 executions than those of CIW-PSO.

Since the CIW-PSO performed better than GA, the comparison delves into improving the PSOs by developing three variations of PSOs. Table 5.6 presents a summary of Constant-Inertia Weight (CIW), Linear-Inertia Weight (LIW), and Exponential-Inertia Weight (EIW) PSO methods for the 9-bus system.

Comparing the total primary operating time (*PR Time*) of LIW and EIW with CIW-PSO, we observe that LIW and CIW exhibit slightly better primary relay operating

Table 5.5: 9-Bus System: Performance Summary of the Numerical Iteration, GA, CIW-PSO Variation

Coordination Approach	Total BR Time (Sec)	Total PR Time (Sec)	CTI (Sec)	Sum of BR and PR Time (Sec)	Number of CTI Violations
Numerical Iteration	16.186	5.524	10.662	21.71	0
GA	10.418	3.275	7.144	13.693	0
CIW-PSO	9.872	2.585	7.286	12.457	0

Table 5.6: 9-Bus System: Performance Summary of the CIW-PSO, LIW-PSO, and EIW-PSO variation

Coordination Approach	Total BR Time (Sec)	Total PR Time (Sec)	CTI (Sec)	Sum of BR and PR Time (Sec)	Number of CTI Violations
CIW-PSO	9.872	2.585	7.286	12.457	0
LIW-PSO	7.268	2.559	4.710	9.827	0
EIW-PSO	6.690	2.761	3.928	9.451	0

time (*PR Time*), while EIW demonstrates the lowest CTI and backup operating time (*BR Time*). By summing up the primary and backup operating times for each of the three variations, we find that EIW yields the lowest value of 9.451s, compared to 9.827s and 12.457s for LIW-PSO and CIW-PSO, respectively. Therefore, EIW is the optimal PSO variation due to its minimal sum of primary and backup operating times. More detail of the performance metric showing the operating and CTI of each coordination pair is presented in Appendix A.3 - A.4.

5.3.3 Result and Analysis for the IEEE 33-Bus System

Similarly to the analysis conducted on the 9-bus systems, the key performance indicators are the total operating time and Coordination Time Interval (CTI). The initial comparison involves three methods: numerical iteration, GA, and CIW-PSO, while the subsequent comparison focuses on three variations of Particle Swarm Optimization. As detailed in section 5.2, the Time Dial Settings (TDS) and the pickup current (I_p) obtained from the optimization solution are presented in Appendix A.7.

Table 5.7 presents the summary of the performance of the numerical iteration, GA, and CIW-PSO for the IEEE 33-bus system. Similar to the 9-bus system analysis findings, the numerical iteration method results have a higher relay operating time for both primary (*PR Time*) and backup (*BR Time*) relays compared to GA and CIW-PSO in the IEEE 33-bus system. However, the performance of GA and CIW-PSO exhibits similarities, but the computational time of GA is consistently higher

Table 5.7: IEEE 33-Bus System: Performance Summary of the Numerical Iteration, GA, CIW-PSO Variation

Coordination Approach	Total BR Time (Sec)	Total PR Time (Sec)	CTI (Sec)	Sum of BR and PR Time (Sec)	Number of CTI Violations
Numerical Iteration	36.012	5.057	30.955	41.069	0
GA	29.106	4.575	24.531	33.681	0
CIW-PSO	29.005	4.541	24.514	33.546	0

and has lower convergence rates across 25 executions compared to CIW-PSO.

Table 5.8 presents the performance of the three variations of PSO for the IEEE 33-bus system. The result matches the findings of the 9-bus system analysis; the primary (*PR Time*) operating time of CIW-PSO and LIW-PSO demonstrates a lower primary operating time compared to EIW-PSO. However, EIW-PSO exhibits the least CTI and backup operating time. When summing up the backup and primary operating times for each of the three variations, EIW-PSO yields the lowest value of 24.821s, which is less than 28.279s and 33.546s. Hence, EIW-PSO, with the least sum of primary and backup operating time, emerges as the superior PSO variation. More detail of the performance metric showing the operating and CTI of each coordination pair for the IEEE 33-bus system is presented in Appendix A.8 - A.10.

The relay settings obtained from the coordination approach were configured and validated on the test system; for instance, in Fig. 5.6, a simulation showcases the results: a Single Line to Ground (SLG) fault was applied between BRK3 and BRK4 in the

Table 5.8: IEEE 33-Bus System: Performance Summary of the CIW-PSO, LIW-PSO, and EIW-PSO Variation

Coordination Approach	Total BR Time (Sec)	Total PR Time (Sec)	CTI (Sec)	Sum of BR and PR Time (Sec)	Number of CTI Violations
CIW-PSO	29.005	4.541	24.514	33.546	0
LIW-PSO	23.766	4.513	19.253	28.279	0
EIW-PSO	20.193	4.628	15.565	24.821	0

9-bus system single line drawing described in Fig. 5.4, the fault was isolated by forward primary protection relay $F3$ at 0.05s and reverse primary protection relay $R4$ at 0.2s which initiated a forward and reverse overcurrent trip signal to breaker at bus 3 and bus 4 respectively. Backup protection relays $F2$ and $R5$, which are the forward and reverse backup relays, did not operate. As the breaker remains closed during post-fault, there is a current flow during the post-fault condition.

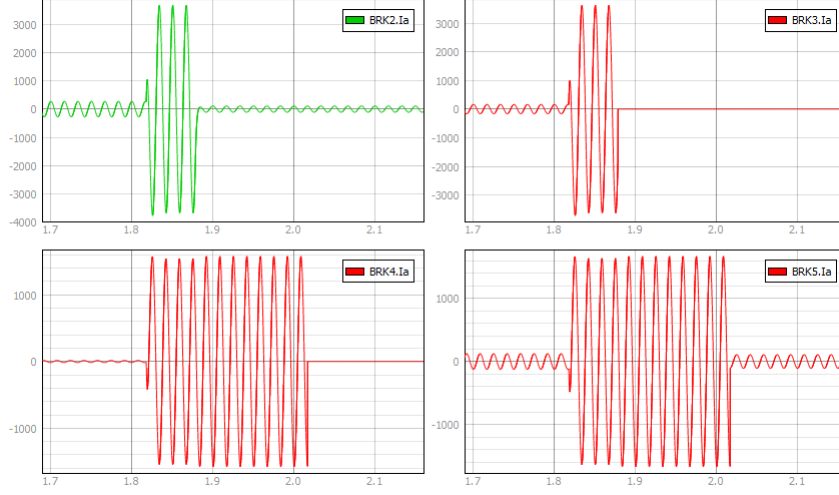


Figure 5.6: Simulation of the fault Isolation by the branch primary protection relays

5.4 Conclusion

As demonstrated in the analysis, achieving optimized relay coordination and operating time depends on the coordination approach adopted. The coordination outcomes from the numerical iteration approach, GA, and PSO were compared across two test systems. While the results of GA and PSO were similar for the IEEE 33-BUS System, GA exhibited longer computational times than PSO. Three PSO variations were developed and evaluated to enhance PSO performance further, focusing on adjusting the velocity inertia weight as detailed in section 5.2. Among these variations, the EIW variation yielded the most favorable outcomes for both test systems, resulting in the shortest operating time. To corroborate the consistent superiority of EIW in minimizing relay operating time, statistical analyses of the four optimization approaches,

including the three PSO variations, are presented in the box plots shown in Fig.5.7 and Fig.5.8 for the 9-bus system and the IEEE 33-bus system, respectively. Notably, the results across 25 executions consistently reaffirmed the superiority of EIW-PSO.

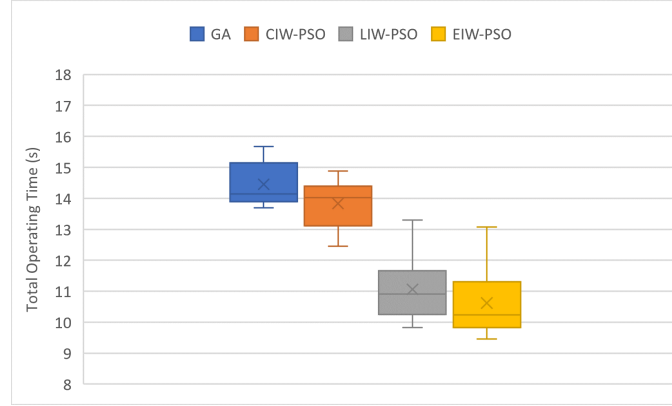


Figure 5.7: 9-bus system: Total operating time of the optimization approaches for 25 executions

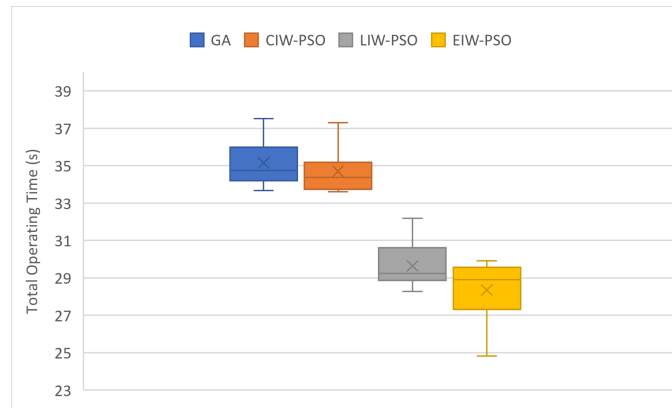


Figure 5.8: Modified IEEE 33-bus system: Total operating time of the optimization approaches for 25 executions

In summary, this chapter presents an optimization approach to achieve optimal relay coordination. It emphasizes the importance of employing optimization algorithms for relay coordination and suggests the adoption of more efficient algorithms for improved outcomes. The subsequent chapter will explore enhancing protection coordination's reliability by identifying and addressing miscoordination issues. This aims to fortify relay coordination, ensuring robustness and reliability amidst increased interconnectivity and the growing penetration of Distributed Generators (DGs).

CHAPTER 6: ADDRESSING OVERCURRENT RELAY MISCOORDINATION CAUSED BY CHANGES IN FAULT CURRENT DURING FAULT ISOLATION

As the power system network evolves, its interconnectivity increases, characterized by bidirectional power flow and unintentional reconfiguration. This characteristic often leads to the miscoordination of Directional Overcurrent Relays (DOCRs). Miscoordination occurs when the backup relay operates faster than the primary protection relay or when the interval between the primary and secondary relay operating time falls below the Coordination Time Interval (CTI). The CTI represents the difference in operating time between the primary and backup relays, providing a safety margin accounting for delays caused by the primary circuit breaker and the primary relay's transducer errors.

6.1 Main Contribution

To prevent miscoordination and minimize relay operations, an optimized coordination solution and formulation are essential. As depicted in chapter 5, achieving coordination among DOCRs involves optimizing the Time Dial Setting, pickup current, and curve type of multiple relays to ensure minimal operating time while maintaining coordination. The work in Chapter 5 demonstrated that the optimization approach results in coordinated DOCRs with reduced total operating time than non-optimization approaches; this was also established in [104] - [105]. The authors in [49, 50, 51, 52, 104, 106, 105] focused on optimizing relay operating times while ensuring coordination under the assumption of a static power system network. [61, 62, 63, 75] are centered on adaptable coordination immune to non-transient topological changes such as line outages, varying DG penetrations, and network reconfig-

uration during maintenance.

In [107]-[108], the miscoordination of DOCR caused by transient changes in fault current during fault isolation was analyzed, and solutions to resolve the miscoordination were proposed; [107, 109] uses the maximum fault current seen by the relay during fault isolation for its CTI constraint to prevent the miscoordination, leading to a significant increase of relay operating time, while [108] introduced an equality constraint that forces all the forward and reverse-direction primary relay protecting a fault zone to operate at the same time. However, this constraint caused a significant increase in relay operating time, and there is no guarantee of obtaining a feasible optimization solution. This chapter presents a dynamic non-linear formulation integrated with an optimization approach to prevent relay miscoordinations while maintaining minimal operating time, thus enhancing system reliability. The investigation and outcomes of this chapter were published in 2023 at the North-American Power Symposium (NAPS) [110] and submitted to Electric Power Systems Research (EPSR) [111], and the main contributions are as follows.

- Presented the critical issue of directional overcurrent relay miscoordination in mesh networks resulting from transient changes in fault current vis-avis network topology changes during fault isolation. This miscoordination arises due to the assumption of a static network in traditional protection coordination formulation.
- Proposed a dynamic non-linear optimization formulation to prevent the potential miscoordination of directional overcurrent relays resulting from transient changes in fault current during fault isolation. This formulation can be incorporated into any optimization algorithm to minimize the operating time of the protection relays while maintaining coordination and ensuring the reliability of the power system.

6.2 Problem Statement and Formulation

In a mesh network with a bidirectional power flow, fault currents can flow in either forward or reverse directions. Hence, every Zone of Protection (ZOP) in such a network must be protected by forward and reverse protection relays. In this chapter, the pair of forward and reverse-direction protection relays protecting each zone of protection are described as adjacent relays; that is, for each ZOP, the forward-directional relay is adjacent to the reverse-directional relay and vice versa.

Figure 6.1 is a simple 4-bus mesh network employed to illustrate the cause of increased fault current and miscoordination during fault isolation; the 4-bus network consists of two fault sources and two protection zones, one between Bus 2 and Bus 3 ($ZOP1$), and the other between Bus 3 and Bus 4 ($ZOP2$). Protection relay $R4$ serves as the reverse-direction protection relay for the zone of protection $ZOP2$ and is also referred to as the adjacent relay to forward-direction protection relay $R3$. If the reverse protection relay $R4$ operates faster than the forward protection relay $R3$, then during the brief interval between the operation of reverse relay $R4$ and forward relay $R3$, the fault current flowing through $R3$ and $R2$ will increase, as all the fault current contributions from $SRC2$ and $SRC1$ will pass through $R2$ and $R3$ within this short timeframe. Figure 6.2 illustrates this increased fault current from the fault current (If_{cl}) observed by $R2$ and $R3$ when the adjacent breaker operated by reverse relay $R4$ is closed to the fault current (If_{op}) when the adjacent breaker operated by reverse relay $R4$ is open. This increase in fault current reduces the CTI between the primary forward-direction relay $R3$ and the backup forward-direction relay $R2$, as depicted in Fig.6.3. Should the CTI decrease below the required threshold, it will result in miscoordination.

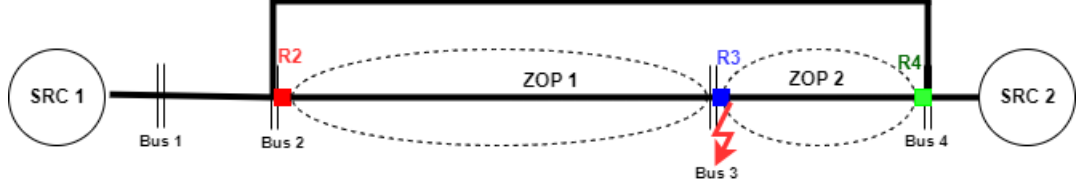


Figure 6.1: A simple mesh network showing ZOP and relays

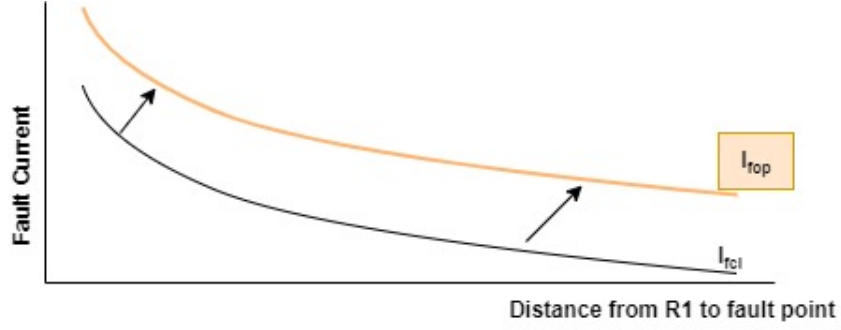


Figure 6.2: Two levels of fault current during fault isolation

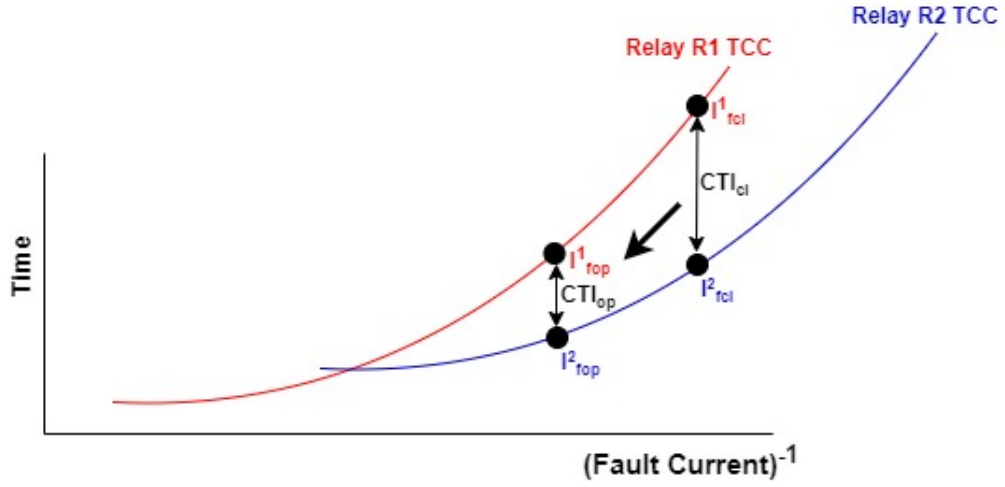


Figure 6.3: Overcurrent TCC for R1 and R2 showing CTI changes during fault isolation

6.3 Proposed Dynamic Formulation

Equation (6.1) is the conventional Time Current Curve (TCC) equation; it is designed for static power system networks such that the fault current is fixed. However, the formulation is compromised when the fault current changes during fault isolation, as illustrated in section 6.2. To address this compromise, the conventional formula is

modified to account for the variation in fault current relative to the transient changes in network topology during fault isolation.

$$t_{pr}^{j,i} = TDS^j \times \left(B + \frac{A}{\left(\frac{I_{fi}^j}{I_p^j} \right)^\beta - 1} \right) \quad (6.1)$$

Where:

$t_{pr}^{j,i}$: Operating time of relay j for fault at ZOP i

TDS : Time Dial Settings

I_{fi}^j : Fault current seen by relay j for fault at ZOP i

I_p^j : Pickup current seen by relay j

A, B, β : Inverse time overcurrent coefficients that determines the curve type

According to [112], the operating time of an inverse-time overcurrent relay can be estimated by solving for the operating time when the integral of (6.1) is equated to 1 as shown in (6.2), this emulates the dynamics of the induction disk inverse-time overcurrent relay which will ensure the coordination of DOCRs even with varying fault current.

$$\int_0^{t_{pr}^{j,i}} \frac{1}{TDS^j \times \left(B + \frac{A}{\left(\frac{I_{fi}^j}{I_p^j} \right)^\beta - 1} \right)} dt = 1 \quad (6.2)$$

Using Fig. 6.1 as a reference to derive a coordination formulation for the forward-direction primary relay $R3$ and reverse-direction backup relay $R2$. As illustrated in section 6.2, there are two levels of fault current seen by relay $R3$ and relay $R2$: firstly, when the adjacent beaker $R4$ is closed (If_{cl}^3) and second, when it is open (If_{op}^3). For forward-direction relay $R3$, equation (6.2) can be rewritten as (6.3)

$$\int_0^{t_{pr}^{3,(ZOP2)}} \frac{1}{TDS^3 \times \left(B + \frac{A}{\left(\frac{I_{f3}^{ZOP2}}{I_p^3} \right)^\beta - 1} \right)} dt = 1 \quad (6.3)$$

The integral in (6.3) can be split into two integrals to account for the two fault levels (I_{cl}^3 and I_{op}^3) seen by forward-direction primary relay $R3$ before and after reverse-direction relay $R4$ operates at time $t4$ respectively, shown in (6.4). In this equation, the operating time ($t_{pr}^{3,(ZOP2)}$) of forward-direction primary relay $R3$ is split considering the time interval before and after reverse-direction relay $R4$ operates at time $t4$. Solving for the operating time ($t_{pr}^{3,(ZOP2)}$) of relay $R3$ through (6.4) yields (6.6); similarly, the operating time ($t_{bc}^{2,(ZOP2)}$) of forward-direction backup relay $R2$ is formulated as a dynamic equation in (6.7).

$$\int_0^{t_{pr}^{3,(ZOP2)}} dt = \int_0^{t4} \frac{1}{K_{f3(cl)}} dt + \int_{t4}^{t_{pr}^{3,(ZOP2)}} \frac{1}{K_{f3(op)}} dt = 1 \quad (6.4)$$

Where:

$$K_{f3(cl)} = TDS^3 \times \left(B + \frac{A}{\left(\frac{I_{f3(cl)}}{I_{p3}^{ZOP2}} \right)^\beta - 1} \right)$$

$$K_{f3(op)} = TDS^3 \times \left(B + \frac{A}{\left(\frac{I_{f3(op)}}{I_{p3}^{ZOP2}} \right)^\beta - 1} \right)$$

$$\frac{t4}{K_{f3(cl)}} + \frac{t_{pr}^{3,(ZOP2)} - t4}{K_{f3(op)}} = 1 \quad (6.5)$$

$$t_{pr}^{3,(ZOP2)} = t^4 + \frac{(K_{f3(op)}^{ZOP2} \times K_{f3(cl)}^{ZOP2}) - (K_{f3(op)}^{ZOP2} \times t^4)}{K_{f3(cl)}^{ZOP2}} \quad (6.6)$$

$$t_{bc}^{2,(ZOP2)} = t^4 + \frac{(K_{f2(op)}^{ZOP2} \times K_{f2(cl)}^{ZOP2}) - (K_{f2(op)}^{ZOP2} \times t^4)}{K_{f2(cl)}^{ZOP2}} \quad (6.7)$$

Equation(6.6) and(6.7) aim to prevent the miscoordination due to transient fault current during fault isolation when the adjacent reverse relay operates faster than the primary operating relay ($t^4 < t_{pr}^{3,(ZOP2)}$). However, this equation is not feasible for situations when the forward-direction primary relay operates faster than the adjacent reverse-direction relay ($t^4 > t_{pr}^{3,(ZOP2)}$); hence the formulation was amended to give (6.8)- (6.10) such that the conventional static network equation in (6.1) is used when the primary relay operates faster than the adjacent relay ($K_{f4(cl)}^{ZOP2} > K_{f3(cl)}^{ZOP2}$), while the dynamic equations in (6.6) and (6.7) are used when the adjacent breaker responds faster than the primary operating relay ($K_{f4(cl)}^{ZOP2} < K_{f3(cl)}^{ZOP2}$).

$$t_{pr}^{3,(ZOP2)} = M \times \left(t^4 + \frac{(K_{f3(op)}^{ZOP2} \times K_{f3(cl)}^{ZOP2}) - (K_{f3(op)}^{ZOP2} \times t^4)}{K_{f3(cl)}^{ZOP2}} \right) + (1 - M) \times K_{f3(cl)}^{ZOP2} \quad (6.8)$$

$$t_{bc}^{2,(ZOP2)} = M \times \left(t^4 + \frac{(K_{f2(op)}^{ZOP2} \times K_{f2(cl)}^{ZOP2}) - (K_{f2(op)}^{ZOP2} \times t^4)}{K_{f2(cl)}^{ZOP2}} \right) + (1 - M) \times K_{f2(cl)}^{ZOP2} \quad (6.9)$$

$$M = \begin{cases} 1, & \text{if } K_{f4(cl)}^{ZOP2} < K_{f3(cl)}^{ZOP2} \\ 0, & \text{if } K_{f4(cl)}^{ZOP2} \geq K_{f3(cl)}^{ZOP2} \end{cases} \quad (6.10)$$

Where:

$t_{pr}^{3,(ZOP2)}$: Primary operating time of relay 3 for fault at ZOP 2

$t_{bc}^{2,(ZOP2)}$: Backup operating time of relay 2 for fault at ZOP 2

$K_{f3(cl)}^{ZOP2}$: K function of forward direction primary relay 3 when adjacent breaker is closed for fault at ZOP 2

$K_{f3(op)}^{ZOP2}$: K function of forward direction primary relay 3 when adjacent breaker is opened for fault at ZOP 2

$K_{f2(cl)}^{ZOP2}$: K function of forward direction backup relay 2 when adjacent breaker is closed for fault at ZOP 2

$K_{f2(op)}^{ZOP2}$: K function of forward direction backup relay 2 when adjacent breaker is opened for fault at ZOP 2

$K_{f4(cl)}^{ZOP2}$: K function of reverse direction primary relay 4 when adjacent breaker is closed for fault at ZOP 2

6.4 Case Study and Simulation Results

The miscoordination due to transient changes in fault current during fault isolation is illustrated, and the proposed solution approach is validated using the IEEE 8-bus and a modified IEEE 33-bus system. To Validate the performance of the proposed approach in section 6.3, two coordination formulation approaches are compared with the proposed approach. The first approach is the traditional formulation approach described in chapter 5 and equation(6.11), and the second approach is described as a modified traditional approach; the difference between the modified traditional approach and the traditional approach is the fault current used to evaluate the DOCR operating time. The traditional approach assumes a static network, meaning the fault current is constant during fault isolation. Hence it uses the fault current seen by the DOCR when the adjacent breaker is closed (If_{cl}), while the modified traditional formulation approach uses the fault current seen by the DOCR when the adjacent circuit

breaker is open (If_{op}). The formulation for the traditional and modified traditional approach, including the difference, is described in (6.11) - (6.16).

$$\min \sum T_{pr}(If_x) = \min \sum_{i=1}^{\varphi} \sum_{j=1}^{\phi} t_{pr}^{j,i}(If_x) \quad (6.11)$$

$$t_{bc}^i(If_x) - t_{pr}^j(If_x) \geq CTI \quad (6.12)$$

$$TDS_{min} \leq TDS^j \leq TDS_{max} \quad (6.13)$$

$$I_{pmin} \leq I_p^j \leq I_{pmax} \quad (6.14)$$

$$t_{min} \leq t_{pr}^{j,i}(If_x) \leq t_{max} \quad (6.15)$$

$$\text{Where :} \quad If_x = \begin{cases} If_{cl}, & \text{Traditional formulation.} \\ If_{op}, & \text{Modified traditional formulation} \end{cases} \quad (6.16)$$

6.4.1 Description of Test System

Figures 6.4 and 6.5 show the single-line diagram of the IEEE 8-bus system and the modified IEEE 33-bus system, respectively, illustrating the location of the DOCRs. The IEEE 8-bus system is structured as a mesh network comprising a single substation and two DGs. Within this configuration, there are 14 DOCRs and 20 pairs of coordinated relays, as detailed in Table 6.1. The modified IEEE 33-bus system includes one substation and four DGs ($G1, G2, G3, G4$ located at buses 29, 33, 8, and 21 respectively). Among these, three DGs are switched ON, while DG ($G3$) at bus 8 is switched OFF, with all inter-tie switches (depicted by dashed lines) connected. The test system comprises 32 relays and 56 coordinated relay pairs, including corresponding adjacent relays, as detailed in Table 6.2.

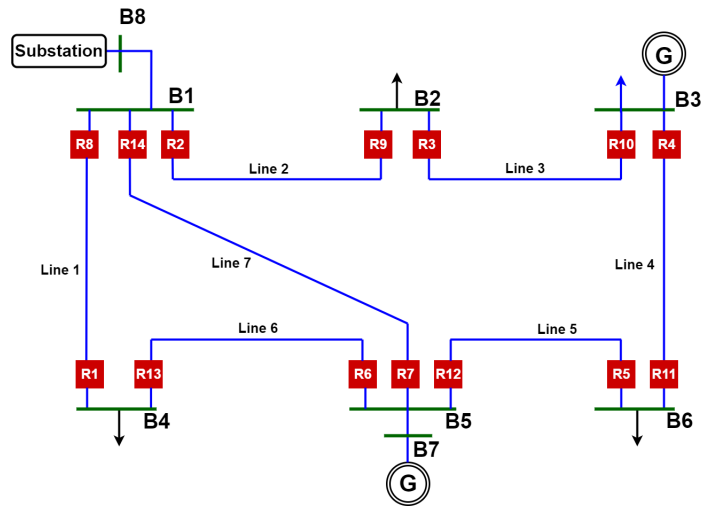


Figure 6.4: IEEE 8-bus system: Single line diagram

Table 6.1: IEEE 8-Bus System: Relay Coordination Pairs

Pair	Primary Relay	Backup Relay	Adjacent Relay	Pair	Primary Relay	Backup Relay	Adjacent Relay
1	R1	R6	R8	11	R7	R13	R14
2	R2	R1	R9	12	R8	R7	R1
3	R2	R7	R9	13	R8	R9	R1
4	R3	R2	R10	14	R10	R11	R3
5	R4	R3	R11	15	R11	R12	R4
6	R5	R4	R12	16	R12	R13	R5
7	R6	R5	R13	17	R12	R14	R5
8	R6	R14	R13	18	R13	R8	R6
9	R7	R5	R14	19	R14	R9	R7
10	R14	R1	R7	20	R9	R10	R2

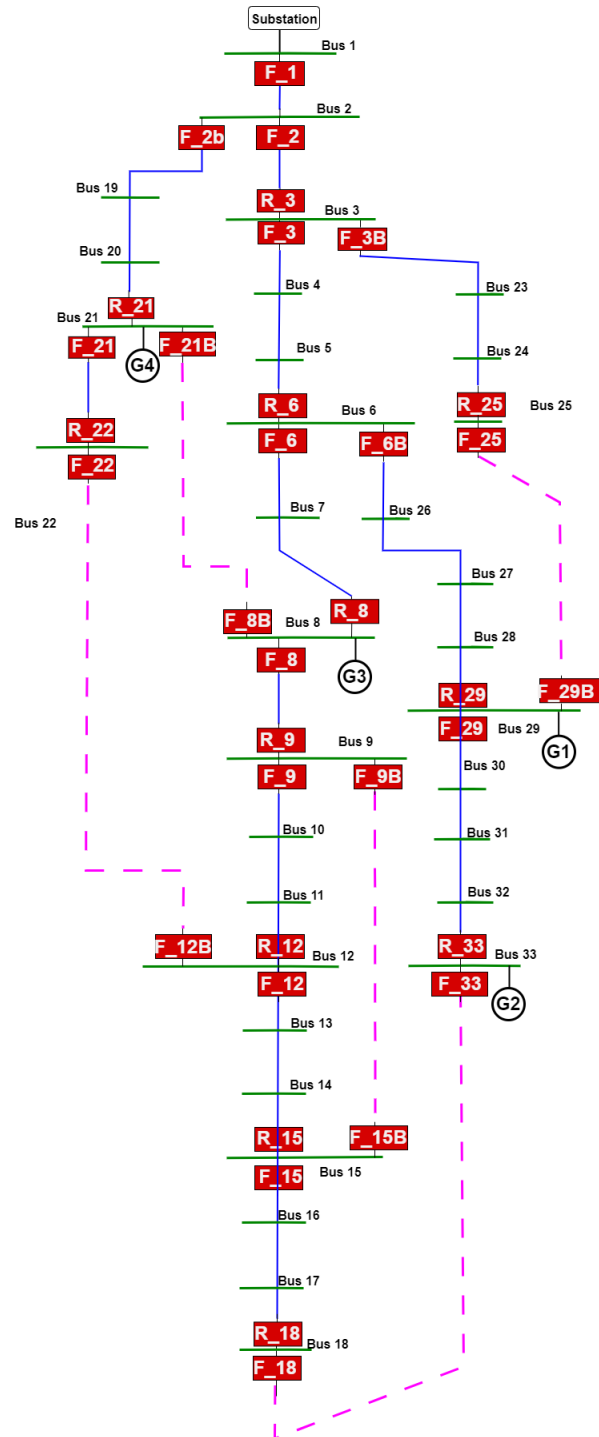


Figure 6.5: Modified IEEE 33-bus system: Single line diagram

Table 6.2: Modified IEEE 33-Bus System: Relay Coordination Pairs

Pair	Primary Relay	Backup Relay	Adjacent Relay	Pair	Primary Relay	Backup Relay	Adjacent Relay
1	F2	F1	R3	29	F3B	F2	R25
2	F2	R21	R3	30	R25	F29B	F3B
3	R3	R25	F2	31	F25	F3B	F29B
4	R3	R6	F2	32	F29B	F6B	F25
5	F3	F2	R6	33	F29B	R33	F25
6	F3	R25	R6	34	F6B	F3	R29
7	R6	R29	F3	35	F6B	R8	R29
8	R6	R8	F3	36	R29	F25	F6B
9	F6	F3	R8	37	R29	R33	F6B
10	F6	R29	R8	38	F29	F25	R33
11	R8	F21B	F6	39	F29	F6B	R33
12	R8	R9	F6	40	R33	F15	R33
13	F8	F21B	R9	41	F15B	F12	F9B
14	F8	F6	R9	42	F15B	F33	F9B
15	R9	R12	F8	43	F9B	F8	F15B
16	R9	F15B	F8	44	F9B	R12	F15B
17	F9	F15B	R12	45	F2B	F1	R21
18	F9	F8	R12	46	F2B	R3	R21
19	R12	R15	F9	47	R21	F12B	F2B
20	R12	F22	F9	48	R21	F8B	F2B
21	F12	F9	R15	49	F21	F2B	F12B
22	F12	F22	R15	50	F21	F8B	F12B
23	R15	F9B	F12	51	F12B	F9	F21
24	R15	F33	F12	52	F12B	R15	F21
25	F15	F12	F33	53	F21B	F2B	F8B
26	F15	F9B	F33	54	F21B	F12B	F8B
27	F33	F29	F15	55	F8B	F6	F21B
28	F3B	R6	R25	56	F8B	R9	F21B

Table 6.3 further provides insights into the variation of primary and backup fault currents observed by the relay in the IEEE 8-bus systems, considering open and closed adjacent breakers. The status of these adjacent breakers controlled by the corresponding adjacent relays is significant for the proposed dynamic formulation and modified traditional formulations described in section 6.2. As detailed in the table, the fault current is higher when the adjacent breaker is open than when it is closed. This variation in fault current is the cause of the miscoordination and needs to be considered in coordination formulations. The variation in the fault current based on adjacent breaker status is also similar in the IEEE 33-bus system as shown in Appendix B.2

Table 6.3: IEEE 8-bus System: Fault Current Considering Adjacent Breaker Status

Pair	Closed Adjacent Breaker		Opened Adjacent Breaker	
	Primary Fault Current (A)	Backup Fault Current (A)	Primary Fault Current (A)	Backup Fault Current (A)
1	3232	3232	5650	5650
2	5924	996	7300	1150
3	5924	1890	7300	2500
4	3556	3556	5500	5500
5	3783	2244	4600	4600
6	2401	2401	4500	4500
7	6109	1197	7300	1250
8	6109	1874	7300	2900
9	5223	1197	7100	1250
10	5199	996	7100	2123
11	5223	987	7100	2150
12	6093	1890	7400	2800
13	6093	1165	7400	1230
14	3883	2344	4900	4800
15	3707	3707	5750	5750
16	5899	987	7400	1150
17	5899	1874	7400	2500
18	2991	2991	5600	5600
19	5199	1165	7100	1230
20	2484	2484	4400	4400

6.4.2 IEEE 8-Bus: Coordination Simulation Results and Analysis

The performance metrics of the three solution formulation approaches are presented for the IEEE 8-bus and the modified IEEE 33-bus system. Table 6.4 shows the CTI for each coordinated relay pair for the IEEE 8-bus system, comprising the three solution formulations discussed in section 6.4 (Traditional formulation, modified traditional formulation, and the proposed formulation).

Table 6.4: IEEE 8-bus System: Coordination Time Interval

Pair	Traditional Formulation CTI (Sec)	Modified Traditional Formulation CTI (Sec)	Proposed Formulation CTI (Sec)
1	0.254	0.209	0.201
2	0.040	0.202	0.201
3	0.091	0.226	0.288
4	0.006	0.223	0.225
5	0.040	0.202	0.201
6	0.217	0.200	0.342
7	0.206	0.226	0.200
8	0.041	0.357	0.201
9	0.277	0.432	0.297
10	0.301	0.220	0.206
11	0.080	1.987	0.312
12	0.020	1.692	0.204
13	0.187	0.373	0.202
14	0.211	0.215	0.210
15	0.205	0.206	0.205
16	0.124	1.962	0.206
17	0.040	0.944	0.210
18	0.202	0.209	0.206
19	0.329	0.205	0.201
20	0.201	0.219	0.228
TOTAL CTI	3.071	10.508	4.546

The salient points from this table are:

- Only the traditional formulation scenario exhibited miscoordination be-

cause 10 coordinated relay pairs violated the 0.2 thresholds.

- The CTIs in both the modified traditional formulation and the proposed formulation did not violate the 0.2 threshold.
- The sum of CTI in the modified traditional formulation is greater than the proposed formulation, making the proposed formulation a better solution approach.

Table 6.5 shows the summary of the performance metric (total operating time, sum of CTIs, and number of CTI violations) of the three formulation approaches. The traditional formulation gives the least total operating time but has the highest number of CTI violations, and the operating time (T_{pr}) of the modified traditional formulation is greater than both the traditional formulation and proposed formulation approach. The detailed performance result for the three formulation approaches is presented in Appendix B.1.

Table 6.5: IEEE 8-Bus System: Summary of Total Operating Time and Coordination Time Interval (CTI)

Formulation Approach	Total Operating Time (Sec)	Sum of CTI (Sec)	Number of CTI Violations (each)
Traditional Formulation	1.2065	3.071	10
Modified Traditional Formulation	2.0844	10.498	0
Proposed Formulation	1.2034	4.546	0

In addition, since PSO, which is a metaheuristic optimization model, was used to solve the protection coordination problem, the consistency of the PSO optimization model result was confirmed over 23 executions to avoid convergence to a local minimum; the statistics of the 23 executions are shown in the boxplots in Fig. 6.6.

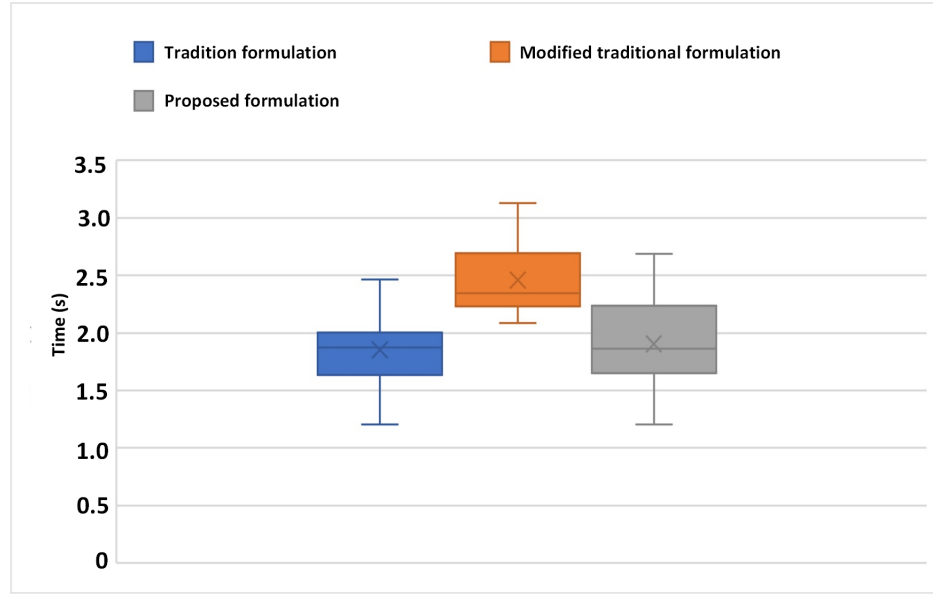


Figure 6.6: IEEE 8-bus system: Statistics of the total operating time from each formulation approach across 23 executions

6.4.3 IEEE 33-Bus Coordination Simulation Results and Analysis

Table 6.6 shows the results of the IEEE 33-bus system in terms of the performance metrics: the total operating time, the sum of CTI, and the number of CTI violations. The detailed performance result for the three formulation approaches is presented in Appendix B.3 and Appendix B.4.

Table 6.6: Modified IEEE 33-bus system: Summary of Total Operating Time and Coordination Time Interval (CTI)

Formulation Approach	Total Operating Time (Sec)	Sum of CTI (Sec)	Number of CTI Violations (each)
Traditional Formulation	3.894	9.771	44
Modified Traditional Formulation	5.696	21.647	0
Proposed Formulation	4.175	12.396	0

The results and the salient points are quite similar to the results from the IEEE 8-bus

system and are:

- **Total Operating Time and Sum of CTI Comparisons:** The modified traditional formulation has a higher total operating time and sum of CTIs than both the traditional and proposed formulation approaches. This highlights its relatively inefficient timing despite its coordination benefits.
- **Traditional Formulation Coordination Issue:** While the traditional formulation exhibits the lowest total operating time, it faces significant coordination challenges. Specifically, 44 out of 56 relay pairs failed to meet the coordination threshold, demonstrating a high rate of miscoordination.
- **CTI Threshold Compliance:** Both the modified traditional and proposed formulations successfully adhere to the CTI threshold criteria, with no instances of violation noted. This indicates a strong coordination performance for these approaches.
- **Performance of Proposed Formulation:** The proposed formulation achieves an acceptable trade-off between the reduction of total operating time and relay coordination by complying with CTI thresholds while maintaining a total operating time that is lower than the modified traditional approach but slightly higher than the traditional formulation.

Similarly to the IEEE 8-bus system, the consistency of the PSO optimization model result was confirmed over 23 executions to avoid convergence to the local minimum. Figure 6.7 is a box plot describing the statistics of the total operating time of the DOCR considering the 23 PSO executions. The statistics are consistent with the observed takeaways.

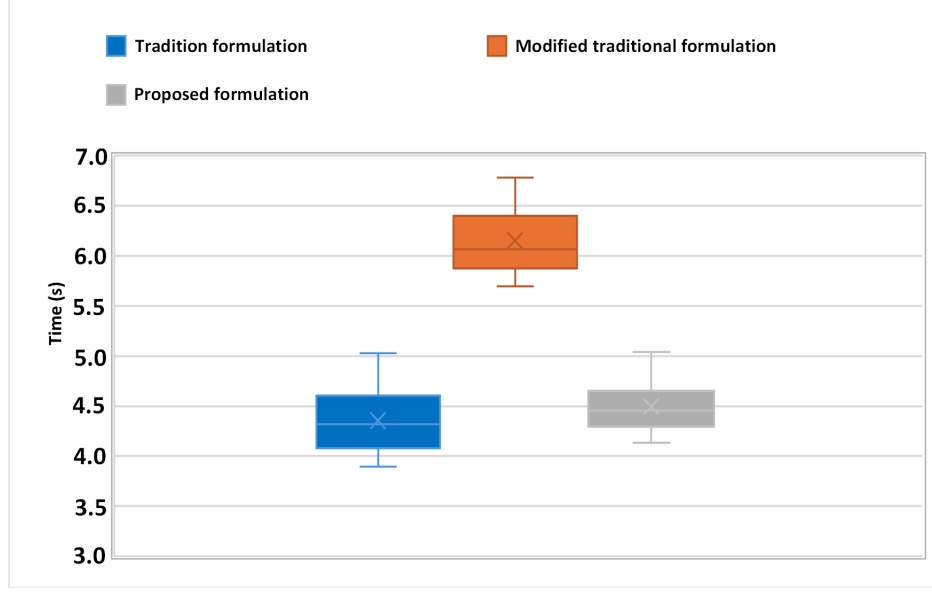


Figure 6.7: Modified IEEE 33-Bus System: Statistics of the total operating time from each formulation approach across 23 executions

6.5 Conclusion and Future Work

In this chapter, the miscoordination caused by transient changes in fault current during fault isolation was analyzed, leading to the presentation of a dynamic non-linear formulation integrated with optimization approaches to prevent miscoordination while maintaining minimal operating time. The proposed formulation ensures coordination even with varying fault currents, as validated through case studies on IEEE 8-bus and 33-bus systems. Results indicate superior performance of the proposed formulation over the traditional and modified traditional approaches. The proposed formulation offers an acceptable trade-off between reduced operating time and DOCR coordination, thus enhancing overall system reliability.

In conclusion, the coordination formulation presented in this chapter addresses a critical issue in power system protection: the miscoordination of Directional Overcurrent Relays (DOCRs) in evolving network topologies. The practical implications of this contribution offer a coordination formulation that ensures the reliability of the power system protection considering the increasingly complex and interconnected networks.

Looking ahead, further validation of the proposed dynamic non-linear optimization approach is necessary, potentially through real-world field trials. Additionally, exploring the integration of more advanced optimization algorithms could reduce the relays' operating time.

Subsequent chapters expanded upon the proposed formulation by adapting it to create a coordination strategy resilient to changes in network operation and topology, such as line outages. Furthermore, the formulation was broadened to encompass relay coordination and ensure the stability of Distributed Generation (DG) within a mesh network.

CHAPTER 7: A ROBUST DIRECTIONAL OVERCURRENT RELAY COORDINATION STRATEGY: IMMUNE TO NETWORK OPERATION AND TOPOLOGY RECONFIGURATION, ENSURING DISTRIBUTED GENERATION STABILITY

The modernization of the traditional grid is characterized by the integration of distributed generating resources, the introduction of microgrids, and frequent reconfiguration of the network topology and operations. While this modernization aims to enhance grid reliability and resilience, it brings forth challenges such as power quality issues, relay misoperation, and protection relay miscoordination. Chapters 3 and 4 focused on the misoperation of traditional protection elements, chapter 5 and chapter 6 focus on enhancing the relay coordination and preventing miscoordination due to transient changes in fault current during fault isolation, This chapter addresses miscoordination challenges arising from network reconfiguration and also investigates the stability issues of Distributed Generator (DG) during post fault conditions.

7.1 Main Contribution

Building upon the proposed formulation in chapter 6, which targets mesh networks, the strategy proposed in this chapter inherently resolves miscoordination due to transient fault current changes. This chapter presents a strategy for enhancing overcurrent relay coordination to prevent the challenges posed by network operation and topology changes. These changes include line outages, network reconfigurations, and varying DG penetration. This strategy identified the appropriate clustering technique by evaluating the performance of each clustering method using the silhouette score metric; it leveraged this metric to determine the clustering variable that would yield

superior optimization results and validated that the choice of the variable selected for clustering significantly influences the outcome of the optimization solution.

The paper's contributions are centered around investigating DG stability issues and DOCR miscoordination due to changes in network topology and generation short circuit capacity. Some parts of the investigation and outcomes of this chapter were published in 2024 at the North-American Power Symposium (NAPS) [113] and submitted to Industry Applications Society (IAS) [114] and Electric Power Systems Research (EPSR) [111] for peer reviewing, and the contributions are categorized into two main sections as follows:

- Illustrated the instability of DGs when their Critical Clearing Time (CCT) is not considered in the coordination formulation and proposed a CCT-constrained coordination formulation to prevent DG instability
- Illustrated the miscoordination due to network operation and topology changes
- Proposed a clustering-based DOCR coordination optimization strategy to prevent miscoordination due to network operation and topology changes
- Illustrated importance of clustering variable type in enhancing the optimization outcome

7.2 Stability of Distributed Generator

The transient stability of a power system network is the generators' ability to maintain stable operation when subjected to large disturbances such as faults. The generators considered are synchronous machine-based machines. Figure 7.1 is a simplified equivalent of a synchronous machine; the real power delivered to the grid is given by (7.1).

$$P_{elec} = \frac{VE}{X_s} \sin \delta \quad (7.1)$$

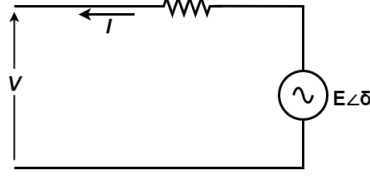


Figure 7.1: A simplified equivalent circuit of a synchronous machine

where

- P_{elec} is the electrical generated power
- V is bus (terminal) voltage
- E is stator-induced emf
- X_s is the equivalent reactance between the generator and the bus
- δ is the angle between V and E or between the rotor axis and stator flux axis (both rotating at synchronous speed).

Neglecting all losses, during the normal operation, the generated electrical power (P_{elec}) is equal to the mechanical power (P_m); however, upon disturbance, the swing equation in (7.2) relates the generated electrical power and the mechanical power; this equation estimates the network's transient behavior. The maximum time to clear the disturbance (fault) is the critical clearing time (t_{cr}) to maintain the system's stability. The critical clearing time is evaluated by solving the swing equation (7.2)

$$M \frac{d^2 \delta}{dt^2} + D \frac{d\delta}{dt} = P_m - \frac{EV \sin(\delta)}{X_s} \quad (7.2)$$

Estimating the Critical Clearing Time for a multimachine system requires complex calculations for different fault disturbances at different locations on the network. Since the scope of this study is limited to optimizing relay coordination and ensuring DG stability, the critical clearing times used in this study are evaluated using time-domain dynamic simulation. This is achieved by varying the fault-clearing time until any of

the DGs loses synchronism; this is repeated for all the network buses. To ensure stability and avoid nuisance tripping of the DGs, the obtained CCT values should be greater than the operating time of the relays required to isolate the corresponding fault.

7.2.1 Solution Approach to Prevent Generator Instability

To obtain an optimized DOCR coordination solution that ensures that the CCT is greater than the relay operating time, authors [115]-[116] addressed DG stability by incorporating CCT considerations in developing relay settings. [115] uses a graphical method to coordinate the relays because the focus is on showing how to prevent the instability of DG that might occur when the critical clearing time is neglected. Hence, the graphical coordination approach will not result in an optimal solution. Authors [117]-[116] proposed a double inverse curve to cater to both the CCT and CTI constraints, [116] incorporating the instantaneous operation of relays to ensure relays operate before CCT. However, these solutions will treat temporary faults as permanent faults because of the instantaneous operation of relays. In addition, the solution approach in [115]-[116] primarily focuses on static networks and DG stability without considering the dynamic nature of the mesh network during fault isolation.

This chapter presents a co-optimization of the relay coordination and the DG CCT requirement; the critical clearing time associated with every fault condition is incorporated as a constraint for the relays assigned to isolate the fault. Equations (7.3) to (7.8) show the objective function and constraints used for the DOCR coordination. The constraint in the optimization formulation includes the critical clearing time (t_{cr}^{ji}) constraint for relay j when there is a fault at zone i as shown in (7.7) and (7.8). The performance metric is the total operating time of relays and the presence of CTI or CCT violations.

$$\min \sum T_{pr} = \min \sum_{i=1}^{\varphi} \sum_{j=1}^{\phi} t_{pr}^{j,i} \quad (7.3)$$

$$t_{bc}^i - t_{pr}^i \geq CTI \quad (7.4)$$

$$TDS_{min} \leq TDS^j \leq TDS_{max} \quad (7.5)$$

$$I_{pmin} \leq I_p^j \leq I_{pmax} \quad (7.6)$$

$$t_{min} \leq t_{pr}^{j,i} \leq t_{crt}^{j,i} \quad (7.7)$$

$$t_{min} \leq t_{bc}^{j,i} \leq t_{crt}^{j,i} \quad (7.8)$$

7.3 Network Topology and Operational Changes

The integration of distributed generation units, the increased interconnectivity, and the adoption of innovative grid technologies have changed the dynamic operation of the power system; the need for fault isolation and service restoration in the face of disruptive events highlights the complexity of relay coordination in terms of adaptability and robustness because the changes in the network topology and generation short circuit capacity impact the conventional DOCR coordination resulting from the changes in nominal current and fault current.

7.3.1 Solution Approach to Prevent Miscoordination due to Changes in Network Topology and Operational Changes

[118] - [119] proposed adaptive relay coordination that uses a communication-assisted approach that devised a distinct set of settings for each network topology. While this approach effectively addressed the issue, it requires a central control station for the continuous reconfiguration of the relay amidst changes in network scenarios. The drawbacks of this method are the cost implications tied to the communication infrastructure and the potential risk of incorrect settings configuration stemming from

regular adjustments to align with changes in scenarios. In addition, another limitation is related to the restricted number of setting groups that a typical numerical protection relay can accommodate [101].

References [55], [120], and [121] propose an approach to reduce the number of setting groups by enabling a single setting to accommodate multiple network scenarios. This eliminates the necessity for a central control point and frequent changes in relay settings, as the relay settings are pre-configured. The setting group can be changed through communication between relays or by employing a machine learning technique, enabling the relay to adjust its setting group dynamically, [55], [120] developed a multi-objective optimization algorithm that includes setting the desired number of setting groups and ensuring that there is no miscoordination in each group, [120] developed a multiobjective optimization algorithm that includes the risk of having many settings changes during system operational changes, while [121] uses a linear optimization approach to coordinate the relays, it also uses a clustering approach that aligns with the linear formulation to determine the different settings group; the index used in the clustering is the average and standard deviation of relay operating time in each network scenario considering a unity value of TDS. The approach in [55], [120], and [121] solves the problem of miscoordination due to operational changes and also prevents the disadvantage of having a distinct relay setting for each network scenario in [118] and [119] by reducing the number of settings group; however, this compromises the optimal operating time of the relay.

Given the compromise in the relay's operating time, it is crucial to identify alternative aspects where improvements in coordination formulation could offset these limitations, thereby enhancing the relay's operational performance. Unlike [121], this chapter presents a non-linear formulation, and the index used for the clustering is the operating time of individual relay and the coordination time interval in each network scenario obtained using this non-linear optimization formulation; this mit-

igates the compromise by reducing the total operating time of the relays while the CTI is maintained. The superiority of the proposed approach over the approach in [121] is presented; the proposed strategy establishes a robust relay coordination scheme that addresses the complexities introduced by network topological changes and changes in generation short circuit capacity, including DG stability constraint and transient changes in current during fault isolation described in chapter 6. In doing so, it presents a comprehensive solution to enhance the coordination of power system protection, thereby bolstering the reliability and effectiveness of the protection mechanisms.

7.3.1.1 Description of Clustering Technique

Clustering is an unsupervised learning technique that groups similar data points based on their characteristics. Thus, data points in the same group are more similar than those in other groups.

In this study, three clustering algorithms: K-means, Hierarchical, and Spectral clustering algorithm was selected [122]. Each algorithm offers unique strengths depending on the dataset's complexity, ensuring a thorough exploration of clustering solutions and making them suitable options for analyzing power system coordination data. K-means excels with large numerical datasets by segmenting based on Euclidean distances. Hierarchical clustering is ideal for exploring unknown data relationships without predefined groupings. Spectral clustering is adept at uncovering complex, non-linear feature relationships, using eigenvalues to reduce dataset dimension.

The study employs a dataset encompassing different system operations and network topology configurations. To investigate and improve the clustering performance on the coordination dataset, three distinct clustering approaches were applied based on different dataset variable types.

1. Approach 1: The variable type is the operating time of the relays com-

puted using the conventional Time Current Curve (TCC) equation referenced in (6.1), with a Time Dial Settings (TDS) value of 1, and a pickup current calculated by multiplying nominal current by 1.5, Equation (6.1) is simplified to (7.9), resulting in the same outcome as [121] which uses the fault current and nominal current seen by the relay. This equivalence arises because the operating time in (7.9) varies linearly with the ratio of the fault current to the nominal current.

$$t_{op}^{j,i} \propto \left(\frac{1}{\left(\frac{I_f}{I_p}\right) - 1} \right) \quad (7.9)$$

2. Approach 2: The approach 2 employs each relay's operating time and CTI computed using the nonlinear optimization formulation adopted in chapter 6.
3. Approach 3: In this approach, the network configurations are randomly grouped, and they are independent of the dataset variables.

The performance of the three clustering techniques on the dataset was evaluated by estimating the silhouette score [123] to determine which clustering is most suitable for the coordination of the dataset. The silhouette score measures how similar a dataset is to its group compared to others. The score ranges from -1 to +1, where a high value indicates that the dataset is well matched to its group and poorly matched to other groups. The silhouette score for each point is calculated using the following formula:

$$s(i) = \frac{b(i) - a(i)}{\max\{a(i), b(i)\}} \quad (7.10)$$

Where $\bar{a}(i)$ is the average distance from the i -th point to the other points in the same cluster, and $\bar{b}(i)$ is the minimum average distance from the i -th point to points in

a different cluster, minimized over clusters. The overall silhouette score for a set of samples is given as the mean of the silhouette score for each sample.

where

- $a(i)$ is the average distance from the i -th point to the other points in the same cluster
- $b(i)$ is the minimum average distance from the i -th point to points in other cluster
- The overall silhouette score for the clustering is given as the mean of the silhouette score of each variable

7.4 Case Study and Simulation Results

The findings are presented in two sections: the first section demonstrates the instability issues associated with Distributed Generation (DG) and validates the effectiveness of the proposed co-optimization strategy in preventing these instabilities. The second section demonstrates issues of DOCR miscoordinations arising from changes in network topology and operations and validates the proposed coordination strategy. The investigation of the DG stability is comprehensively validated on eleven different configurations of an IEEE 33-bus, while the miscoordination due to network reconfiguration is validated on an IEEE 14-bus and an IEEE 33-bus test system.

7.4.1 Description of Test System

Figure 7.2 describes the IEEE 14-bus system showing the location of the DOCRs. The test system comprises 40 relays and 94 coordinated relay pairs; The relay positioned at bus 1, which protects the line connecting bus 1 and 2, is referred to as $R1_2$. Conversely, the relay positioned at bus 2, which protects the line connecting bus 2 and 1, is identified as $R1_2$. The distributed generator (DG) is penetrated at buses 1, 3, 6, 8, and 13. The eight distinct operation and network topologies cases used for

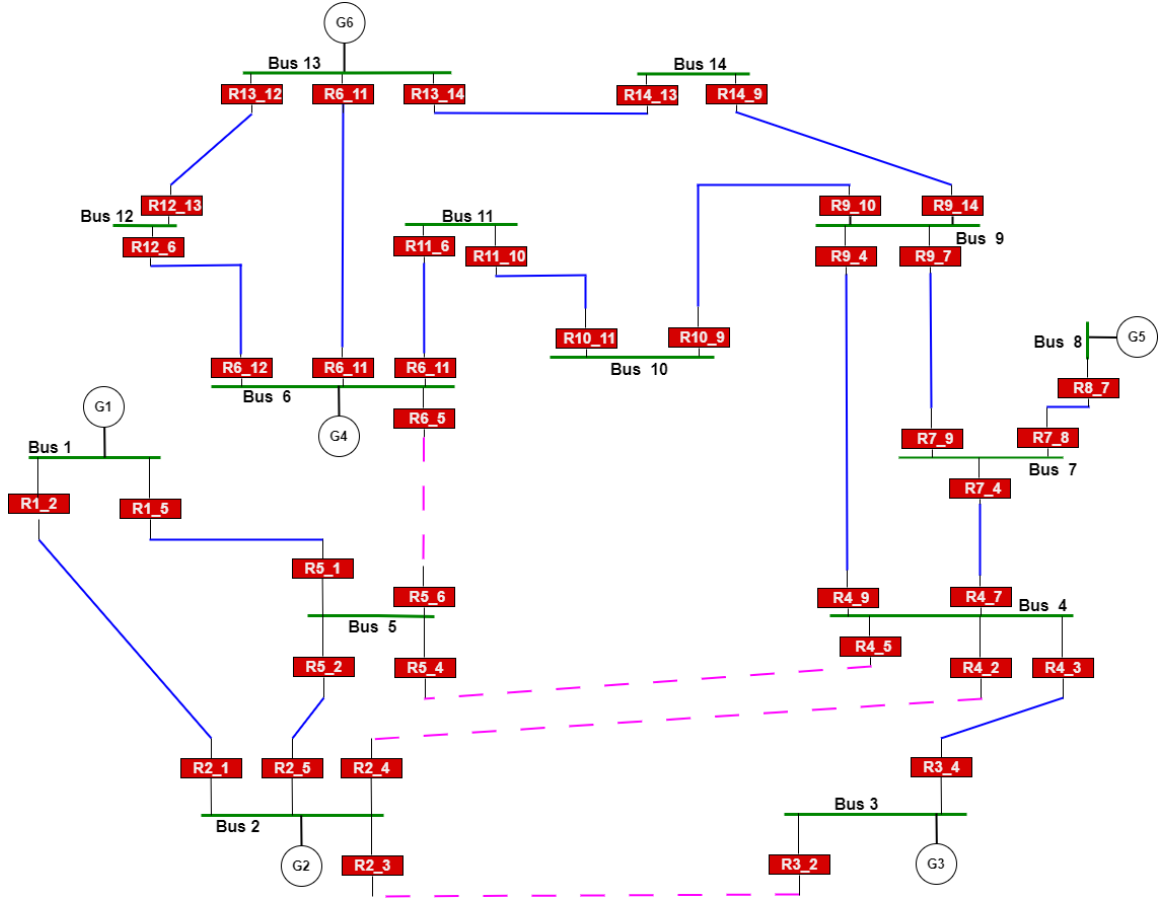


Figure 7.2: Modified IEEE 14-bus system: Single line diagram

the study are detailed in Table 7.1. Cases 1 through 4 are associated with various DG penetrations (different short circuit ratings) at buses 1, 3, 6, 8, and 13, highlighted in the first column of Table 3.1. Meanwhile, cases 5 to 8 have the same DG penetration but different line outages; the lines subject to outages are denoted as dashed lines in Fig. 7.2. For instance, case 1 involves no line outage, whereas case 5 entails opening the branch connecting buses 5 and 4 (*5-4*).

The modified IEEE 33-bus system used to investigate the work in this chapter is the same in chapet 6 shown in Fig. 6.5. The test system comprises 32 DOCRs and 56 coordinated DOCR pairs. A 1.3MVA DG is penetrated at buses 8,21,29,33. Eleven distinct operation and network topologies were simulated and detailed in Table 7.2; each of the cases is associated with different DG status (*on or off*) at buses 8, 21,

Table 7.1: IEEE 14-bus system: Network Operation and Topology Configuration Cases

Network Case	G1 (MVA)	G2 (MVA)	G3 (MVA)	G4 (MVA)	G5 (MVA)	G6 (MVA)	Open Branch
Case 1	615	60	60	25	25	0	N/A
Case 2	615	110	110	75	75	50	N/A
Case 3	615	110	160	25	125	0	N/A
Case 4	615	10	160	75	75	50	N/A
Case 5	615	10	160	75	75	50	5-4
Case 6	615	10	160	75	75	50	6-5
Case 7	615	10	160	75	75	50	2-3
Case 8	615	10	160	75	75	50	2-4

29, and 33, highlighted in the first column of Table 7.2. Meanwhile, only cases 7 to 11 correspond to cases with line outages; the lines subject to outages are denoted as dashed lines in Fig. 6.5. For instance, case 1 involves no line outage, whereas case 10 entails opening the branch connecting buses 25 and 29 (25 – 29) and opening a branch connecting buses 33 and 18 (33 – 18).

Table 7.2: Modified IEEE 33-bus System: Network Operation and Topology Configuration Cases

Network Case	G1 (Status)	G2 (Status)	G3 (Status)	G4 (Status)	Opened Branch
Case 1	on	on	off	on	N/A
Case 2	off	off	off	off	N/A
Case 3	off	on	on	off	N/A
Case 4	on	off	on	off	N/A
Case 5	on	off	off	on	N/A
Case 6	off	on	off	off	N/A
Case 7	on	on	off	on	25-29
Case 8	off	on	on	off	22-12
Case 9	on	off	on	off	33-18, 25-29
Case 10	on	off	off	off	25-29, 9-15
Case 11	off	on	off	off	25-29, 33-18

7.4.2 Stability of Distributed Generator

The instability investigation was carried out on all 11 network configuration cases of IEEE 33-bus in Table 7.2. However, the results of four of the cases are presented in this chapter. The DG units are modeled as synchronous machines, with their parameters adjusted to demonstrate instabilities following protection coordination and to verify the effectiveness of the proposed prevention approach.

Table 7.3 presents the Critical Clearing Time (CCT) of the DG and the corresponding operating time of relays when the CCT stability constraint is not included in the optimization formulation. The relays with CCT less than 0.5s are the relays under scrutiny. The table indicates instances where the CCT is less than 0.5s with the actual CCT values, while instances where it exceeds 0.5s are marked as >0.5 .

CCT violation instances, where the CCT is shorter than the relay operating time, are highlighted in Table 7.3. For example, in Scenario 1, the critical clearing time required for faults within the zone protected by the relay (F_{21}) is 0.15s, while the relay's operating time is 0.31s. Similarly, for faults within the zone protected by the relay (F_{33}), the CCT is 0.18s, whereas the operating time is 0.23s. The count of CCT violation instances in each scenario is 4, 2, 4, and 2 for scenarios 1, 2, 3, and 4, respectively. To confirm the consistency of the findings, the statistics of CCT violations across 23 PSO executions are depicted in Fig. 7.3, which shows that the CCT violation is consistent.

Table 7.3: Modified IEEE 33-Bus System: Critical Clearing Time and Relay Operating Time (Without CCT Constraint)

Relay	Critical Clearing Time in each Network Case (Sec)				Operating Time in each Network Case (Sec)			
	1	2	3	4	1	2	3	4
F2	0.3	0.20	0.24	0.2	0.049	0.032	0.007	0.090
F3	0.25	0.22	0.24	>0.5	0.168	0.085	0.112	0.135
F6	>0.5	>0.5	0.22	>0.5	0.137	0.332	0.169	0.184
F8	>0.5	>0.5	>0.5	0.17	0.293	0.261	0.008	0.124
F9	>0.5	>0.5	>0.5	>0.5	0.099	0.03	0.002	0.023
F12	>0.5	>0.5	>0.5	>0.5	0.024	0.015	0.103	0.226
F15	>0.5	>0.5	>0.5	>0.5	0.325	0.131	0.025	0.315
F21	0.15	0.13	0.15	>0.5	0.313	0.122	0.182	0.481
F22	0.3	>0.5	>0.5	>0.5	0.183	0.077	0.486	0.136
F25	>0.5	>0.5	>0.5	>0.5	0.010	0.172	0.155	0.170
F29	0.15	0.15	0.18	0.17	0.042	0.015	0.013	0.259
F33	0.18	>0.5	0.18	>0.5	0.228	0.049	0.093	0.183
R3	0.3	>0.5	>0.5	0.2	0.025	0.059	0.338	0.028
R6	0.25	0.22	0.24	>0.5	0.163	0.165	0.258	0.020
R8	>0.5	>0.5	>0.5	0.17	0.003	0.011	0.124	0.022
R9	>0.5	>0.5	>0.5	>0.5	0.123	0.395	0.150	0.019
R12	>0.5	>0.5	>0.5	>0.5	0.165	0.229	0.196	0.150
R15	>0.5	>0.5	>0.5	>0.5	0.120	0.067	0.197	0.057
R21	0.16	0.13	0.17	>0.5	0.061	0.19	0.256	0.163
R25	>0.5	>0.5	>0.5	>0.5	0.144	0.456	0.000	0.000
R29	0.18	0.15	0.18	0.17	0.050	0.029	0.017	0.184
R33	0.18	>0.5	0.16	>0.5	0.153	0.1	0.326	0.000
F21B	0.15	0.13	0.17	>0.5	0.171	0.111	0.107	0.381
F15B	>0.5	>0.5	>0.5	>0.5	0.020	0.232	0.213	0.395
F9B	>0.5	>0.5	>0.5	>0.5	0.119	0.059	0.366	0.076
F29B	0.15	0.15	0.18	0.17	0.202	0.194	0.085	0.156
F3B	0.25	0.22	0.24	>0.5	0.201	0.062	0.022	0.030
F6B	>0.5	>0.5	0.22	>0.5	0.097	0.156	0.037	0.090
F8B	>0.5	>0.5	>0.5	>0.5	0.207	0.066	0.025	0.068
F2B	0.3	0.20	0.24	0.2	0.079	0.099	0.075	0.029
F12B	>0.5	>0.5	>0.5	>0.5	0.236	0.305	0.293	0.230
Total Operating Time					4.208	4.306	4.442	4.424

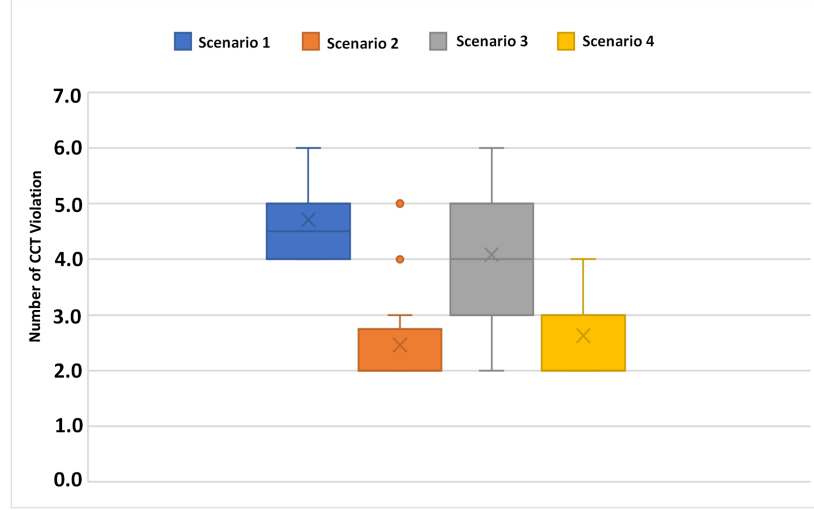


Figure 7.3: Statistics of the CCT violation of the four scenarios across 23 executions

To prevent instability, the co-optimization formulation of relay coordination and CCT is implemented. Table 7.4 shows the relay operating times after integrating the CCT constraint into the formulation. It is observed that the introduction of the CCT constraint effectively prevented CCT violations, as the operating times of the critical relays (those under observation) are now shorter than the CCT. For instance, the operating time of relay $F21$ in scenario 1 reduces to 0.14s, which is lower than the CCT value of 0.15s. However, the total operating time across all four scenarios has increased due to the inclusion of the CCT constraint.

The implementation of the simulation results is shown in Fig. 7.4 and Fig. 7.5; Figure. 7.4 illustrates the instability experienced by DG1 in scenario 1 because relay $F21B$ operating time (0.171s) is greater than the prescribed CCT of 0.15s. In contrast, Figure 7.5 shows the stability of DG1 after implementing the CCT constraint because the operating time of the relay is reduced to 0.127s, which is lower than the CCT threshold.

Table 7.4: IEEE 33-Bus System: Relay Operating Time Considering CCT Constraint

Relay	Operating Time in each Scenario (s)				Relay	Operating Time in each Scenario (s)			
	1	5	7	9		1	5	7	9
F2	0.09	0.03	0.09	0.12	R12	0.46	0.1	0.15	0.31
F3	0.16	0	0.21	0.47	R15	0.11	0.09	0.1	0.07
F6	0.05	0.16	0.1	0.2	R21	0.1	0.07	0.15	0.3
F8	0.07	0.03	0.11	0.11	R25	0.45	0.483	0	0
F9	0.1	0.21	0.13	0.13	R29	0.12	0.1	0.16	0.16
F12	0.18	0.297	0.42	0.04	R33	0.16	0.11	0.15	0
F15	0.29	0.15	0.08	0.29	F21B	0.127	0.09	0.16	0.476
F21	0.14	0.07	0.09	0.08	F15B	0.14	0.39	0.33	0.13
F22	0.24	0.15	0.18	0.43	F9B	0.1	0.12	0.21	0.13
F25	0.06	0.23	0.22	0.18	F29B	0.01	0.05	0.17	0.14
F29	0.09	0.11	0.18	0.09	F3B	0	0.17	0.05	0.05
F33	0.01	0.01	0.18	0.19	F6B	0.14	0.2	0.13	0.06
R3	0.07	0.12	0.47	0.16	F8B	0.21	0	0.12	0
R6	0.22	0.16	0.07	0	F2B	0.15	0.15	0.03	0.074
R8	0.32	0.491	0.43	0.15	F12B	0.32	0.29	0.09	0.21
R9	0.2	0.139	0.14	0.39					
Total Operating Time						4.907	4.590	4.840	4.757

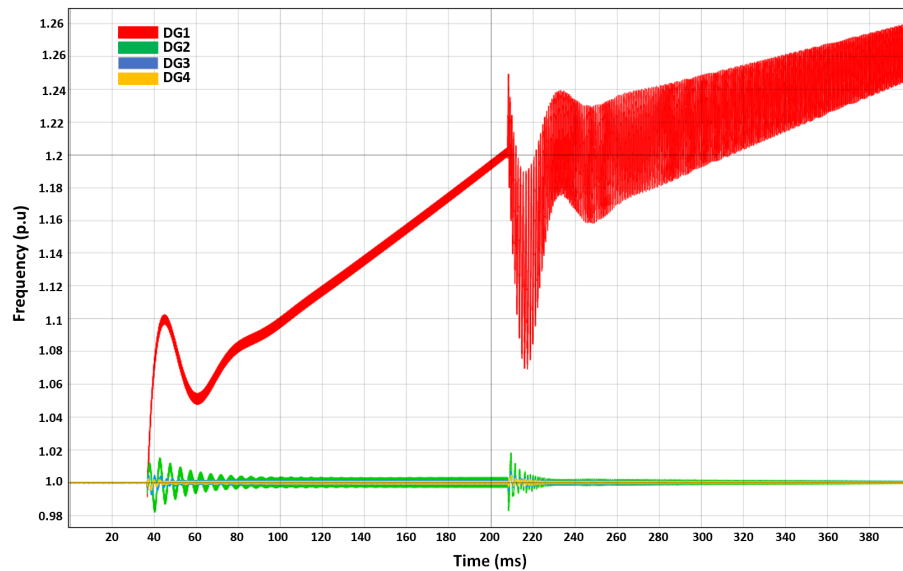


Figure 7.4: DG1 instability due to CCT violation (Before implementing CCT constraint in relay coordination)

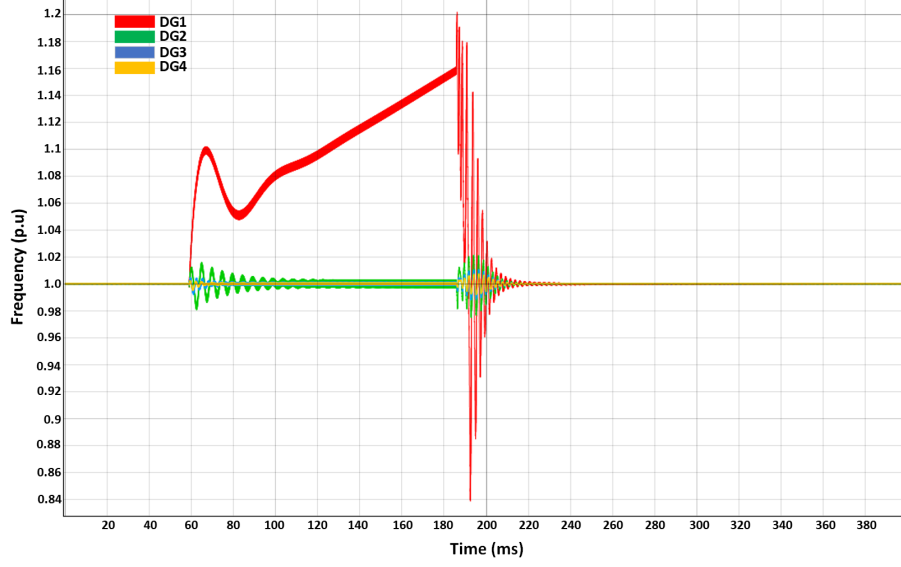


Figure 7.5: Stable DG1 after relay operation (After implementing CCT constraint in relay coordination)

7.4.3 Network Topology and Operational Changes

The strategy to prevent the miscoordination caused by network topology and operational changes involves clustering and optimization. The results of both steps are presented for a Modified IEEE 14-bus and IEEE 33-bus test system.

7.4.3.1 Clustering result

Three clustering techniques; K-means, Hierarchical, and spectral clustering algorithms, are compared. The best clustering technique for miscoordination is determined by evaluating the performance of each clustering technique using the silhouette score metric. The performance was analyzed for the two variable types discussed in section 7.3.1.1. The 8 and 11 network configuration cases in IEEE 14-bus (Table 7.1) and IEEE 33-bus test system (Table 7.2), respectively, are grouped into three such that a unique coordination Setting Group (SG) is assigned to each group.

Table 7.5 summarizes the performance of the clustering techniques; clustering approach 2 consistently demonstrates the highest silhouette scores, indicating superior

Table 7.5: Summary of Clustering Performance

Test System	Silhouette Score				
	Clustering Approach 1		Clustering Approach 2		Clustering Approach 3
	K-means/ Hierarchy	Spectral	K-means/ Hierarchy	Spectral	
IEEE 14-bus	0.185	0.043	0.372	0.13	-0.12
IEEE 33-bus	0.059	-0.091	0.247	0.023	-0.09

clustering performance. In addition, the K-means clustering algorithm consistently has a higher silhouette score and outperforms spectral clustering. Therefore, the grouping of the K-means clustering is adopted for this study. However, an optimization framework is devised for all three approaches, and the optimization outcomes are compared to validate the clustering performance of the three approaches.

The grouping results of the K-means clustering for the three approaches are shown in Fig. 7.6 and Fig. 7.7; the approaches are based on the variable type as explained in section 7.3.1.1, each approach is grouped into three Setting Groups (SGs).

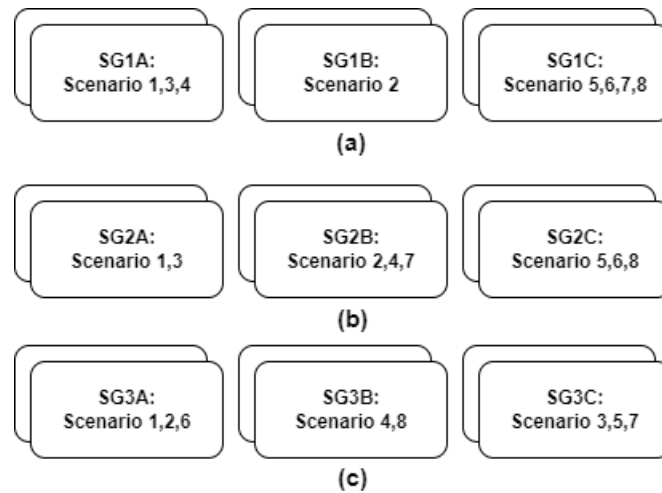


Figure 7.6: IEEE 14-bus Clustering Result: (a) Clustering Approach 1 (b) Clustering Approach 2 and (c) Clustering Approach 3

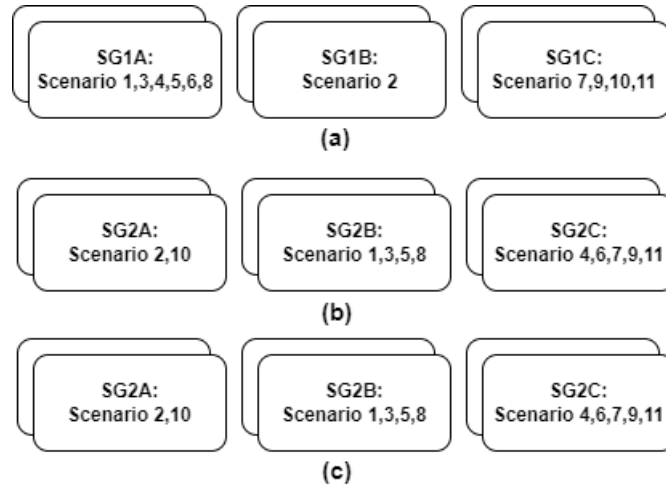


Figure 7.7: IEEE 33-bus Clustering Result: (a) Clustering Approach 1 (b) Clustering Approach 2 and (c) Clustering Approach 3

IEEE 14-bus:

- For approach 1 are SG1A comprising network configuration cases 1, 3, 4, SG1B comprising network configuration cases 2, and SG1C comprising network configuration cases 5, 6, 7, 8
- For approach 2 are SG2A comprising network configuration cases 1, 3, SG2B comprising network configuration cases 2, 4, 7, and SG2C comprising network configuration cases 5, 6, 8
- For approach 3 are SG3A comprising network configuration cases 1, 2, 6, SG3B comprising network configuration cases 4, 8, and SG3C comprising network configuration cases 3, 5, 7

IEEE 33-bus:

- For approach 1 are SG1A comprising network configuration cases 1, 3, 4, 5, 6, 8, SG1B comprising network configuration cases 2, and SG1C comprising network configuration cases 7, 9, 10, 11
- For approach 2 are SG2A comprising network configuration cases 2, 10,

SG2B comprising network configuration cases 1, 3, 5, 8, and SG2C comprising network configuration cases 4, 6, 7, 9, 11

- For approach 3 are SG3A comprising network configuration cases 1, 2, 3, 4, SG3B comprising network configuration cases 5, 6, 7, 8, and SG3C comprising network configuration cases 9, 10, 11

7.4.3.2 Optimization Results

Initially, before optimizing the coordination formulation for Distributed Overcurrent Relay (DOCR) settings in each setting group outlined Fig. 7.6 and Fig. 7.7, the attempt to create a single coordination setting capable of functioning without miscoordination across all the network cases in the IEEE 14-bus system and the IEEE 33-bus system yielded no feasible solution. Consequently, a tailored DOCR coordination solution was optimized for each setting group. Since PSO, a metaheuristic optimization algorithm, is used, the optimization is executed at least 25 times.

Tables 7.6 and 7.7 provide statistical insights into Coordination Time Interval (CTI) violations, highlighting instances of miscoordination that arise when relay coordination intended for a specific setting group is applied to a different network case not belonging to that setting group. The highlighted cases in Tables 7.6 and 7.7 show no CTI violations; they correspond to network cases assigned to specific groups and configured with the same setting group.

For instance, In Table 7.6, Setting Group 1B (SG1B), which is tailored solely for case 2, only case 2 exhibits relay coordination. Similarly, within Setting Group 1A (SG1A), designated for network cases 1, 3, and 4, coordination was achieved solely for cases 1, 3, and 4, whereas other cases displayed miscoordination in at least one of their relay coordinating pairs.

To further validate the most effective approach, each clustering method's total DOCR operating time is compared. Table 7.8 presents the optimization outcomes for both the

Table 7.6: Modified IEEE 14-Bus System: Overview of the Coordination Time Interval Violations in Cases across Setting Groups

Network Case	Statistics	SG 1A	SG 1B	SG 1C	SG 2A	SG 2B	SG 2C	SG 3A	SG 3B	SG 3C
Case 1	Median	0	2	4	0	2	4	0	4	3
	Minimum	0	2	3	0	2	4	0	3	3
Case 2	Median	3	0	2	3	0	2	0	1	2
	Minimum	2	0	1	2	0	1	0	1	1
Case 3	Median	0	4	3	0	2	2	2	3	0
	Minimum	0	2	3	0	1	1	2	2	0
Case 4	Median	0	4	2	2	0	1	1	0	3
	Minimum	0	2	1	2	0	1	0	0	2
Case 5	Median	5	3	0	5	3	0	4	2	0
	Minimum	4	3	0	3	3	0	3	2	0
Case 6	Median	4	2	0	3	3	0	0	1	3
	Minimum	2	2	0	2	2	0	0	1	2
Case 7	Median	2	5	0	4	0	3	5	4	0
	Minimum	2	4	0	3	0	2	4	2	0
Case 8	Median	5	4	0	5	3	0	5	0	2
	Minimum	4	3	0	3	2	0	4	0	1

IEEE 14-bus and 33-bus systems; the total DOCR operating time for each clustering is estimated using (7.11), it is the sum of all the relay operating time for all the network cases within each clustering setting group, considering that the configuration of DOCR coordination settings for each case aligns with the respective setting group to which they are clustered.

$$\sum T_{clust} = \sum_{SG=1}^l \sum_{Case=1}^k \sum_{n=1}^m t_{case}^n \quad (7.11)$$

To reinforce the consistency of these findings, Figure.7.8 and Figure.7.9 present a box plot illustrating the total operating time across 25 executions for the three clusterings. This aligns with the results in Table 7.8: clustering approach 3 consistently yields a higher total operating time than Clustering Approaches 1 and 2, while clustering approach 2 consistently produces the least total operating time. A detailed total operating time obtained from the three clustering approaches is presented in

Table 7.7: Modified IEEE 33-Bus System: Overview of the Coordination Time Interval Violations in Cases across Setting Groups

Network Case	Statistics	SG 1A	SG 1B	SG 1C	SG 2A	SG 2B	SG 2C	SG 3A	SG 3B	SG 3C
Case 1	Median	0	5	4	4	0	2	0	3	5
	Minimum	0	4	3	4	0	2	0	2	4
Case 2	Median	4	0	2	0	6	2	0	4	3
	Minimum	3	0	2	0	4	2	0	3	3
Case 3	Median	0	5	3	4	0	5	0	3	5
	Minimum	0	4	2	2	0	3	0	1	3
Case 4	Median	0	4	4	3	3	0	0	1	5
	Minimum	0	3	2	3	2	0	0	1	4
Case 5	Median	0	3	2	4	0	4	1	0	3
	Minimum	0	2	2	2	0	3	1	0	3
Case 6	Median	0	2	3	3	4	0	4	0	2
	Minimum	0	2	2	1	3	0	2	0	0
Case 7	Median	3	5	0	3	2	0	2	0	3
	Minimum	1	4	0	3	0	0	1	0	0
Case 8	Median	0	2	3	3	0	3	2	0	4
	Minimum	0	1	2	2	0	2	2	0	2
Case 9	Median	3	2	0	3	5	0	4	5	0
	Minimum	2	2	0	2	2	0	2	3	0
Case 10	Median	3	2	0	0	4	1	3	6	0
	Minimum	3	0	0	0	3	0	2	4	0
Case 11	Median	5	2	0	2	4	0	3	5	0
	Minimum	4	2	0	1	4	0	2	4	0

Table 7.8: Total Operating Time of each Clustering Approach

Test System	Clustering 1 (Sec)	Clustering 2 (Sec)	Clustering 3 (Sec)
IEEE 14 -bus	41.51	37.91	46.85
IEEE 33-bus	62.60	58.37	66.11

appendix C.1 and C.2.

The result of optimization shows that clustering approach 2, which employs each relay's operating time and CTI computed using the nonlinear optimization formulation in chapter 6, has the least total operating time; this optimization result aligns with the clustering performance result in Table 7.4, which shows that clustering approach 2 has the highest silhouette score (best performance); hence it is the most effective.

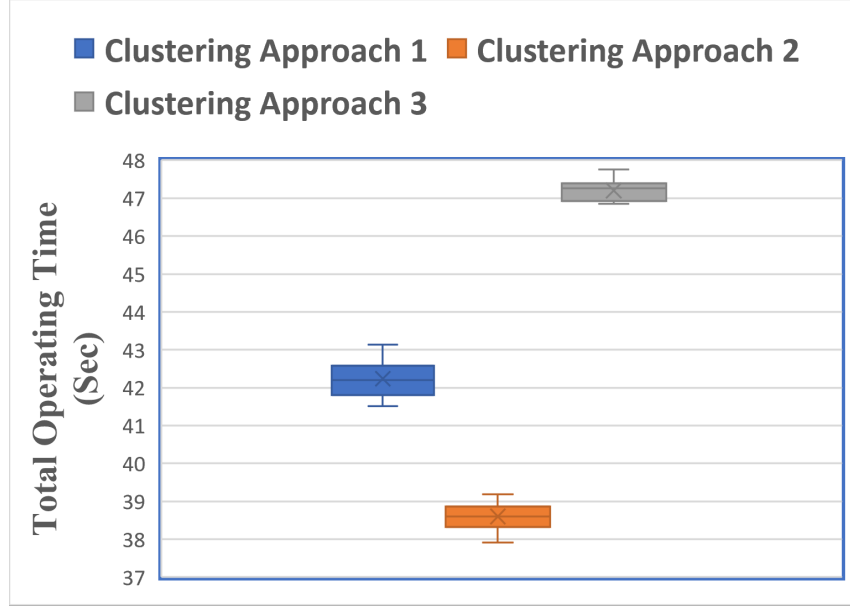


Figure 7.8: Modified IEEE 14-bus system: Total operating time of the three clustering approach considering 25 executions

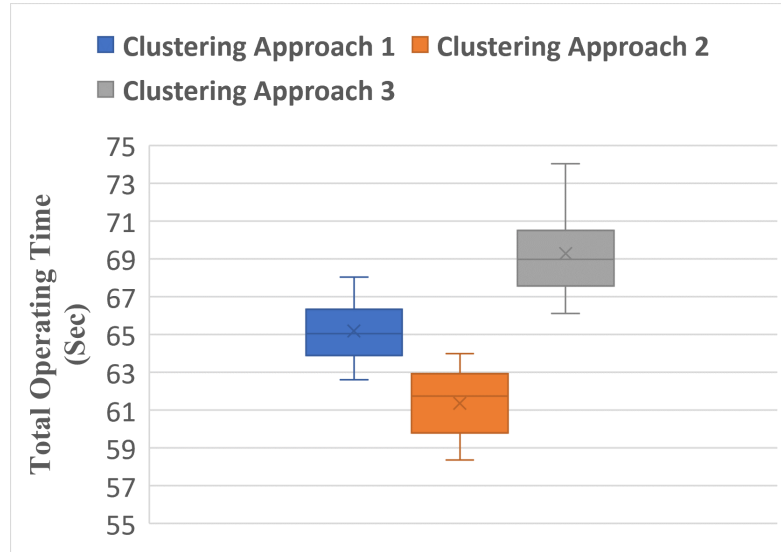


Figure 7.9: Modified IEEE 33-bus system: Total operating time of the three clustering approach considering 25 executions

7.5 Conclusion and Future Work

This study underscores the importance of effectively coordinating directional overcurrent relays in power systems considering changes in network topology and generation short circuit capacity, including Distributed Generators (DG) stability.

The first part of the investigation showcased the inherent instability within the system when the CCT of DGs is not considered in coordination formulation, prompting the adoption of a solution that incorporated the Critical Clearing Time (CCT) constraint. While this adjustment effectively curbed instances of CCT violation, it also resulted in a notable increase in the cumulative operating time across all relays. Hence, optimization approaches should be developed to limit the increase in total operating time due to the inclusion of the CCT constraint.

The chapter also addresses the changes in network topology and generation short circuit capacity by employing K-means clustering to group distinct operational and network topology scenarios into specific relay setting groups. Coordination Time Interval (CTI) violations resulting from changing network topology and varying generation short circuit capacity were illustrated, underscoring the importance of assigning tailored setting groups to individual cases to achieve effective coordination. In addition, the comparison of total operating times across the clustering approaches emphasized the tangible benefits of selecting the appropriate clustering variable to achieve an optimized grouping of network cases.

While this research provides valuable insights, the proposed methodology's real-world validation applicability within diverse power system configurations presents promising avenues for future research. In conclusion, this study signifies a step forward in addressing the challenges of relay coordination in modern power systems, offering a robust framework for improved reliability and resilience in the face of operation and network reconfiguration, including varying DG short circuit capacity.

CHAPTER 8: CONCLUSIONS AND RECOMMENDATIONS

8.1 Overview

This dissertation addresses and proposes solutions to the challenges of power system protection posed by modernizing the grid, characterized by increased grid interconnectivity and integration of Distributed Generators (DG). The investigation into power system protection challenges was approached from two primary perspectives: Misoperation of the protection scheme and protection relay coordination challenges posed by increased interconnectivity, DG integration, and frequent grid reconfiguration such as line outage and variation in DG short circuit capacity. Chapters 3, and 4 delve into the misoperation of protection schemes, while Chapters 5, 6, and 7 delve into Directional Overcurrent Relay (DOCR) coordination challenges. Through rigorous analysis, these challenges were investigated, and enhanced solution strategies were proposed; these include the development of dynamic TCC formulation that is immune to variation in fault current during fault isolation, application of optimization, and clustering techniques to minimize the DOCR operating time while maintaining coordination standards.

8.2 Summary of Research Contributions

This work advances the understanding of how grid modernization affects the reliability of traditional power system protection. The contributions can be summarized as follows:

1. In chapter 3, a comprehensive impact analysis of the effects of Inverter-Based Distributed Generators (IBDGs) on conventional protection schemes

was investigated, and it was shown that the power system's fault characteristic depends on the type of DGs on the network. The chapter revealed that the fault behavior of the power system correlates with the specific types of DGs integrated into the network. This research lays the groundwork for collaboration between manufacturers of inverter-based DGs and protection engineers, aiming to bolster the reliability of the power grid.

2. In Chapter 4, the prevention strategy for protection scheme misoperation, particularly focusing on the directional element, is presented. Identifying the fault characteristics associated with different DG types and investigating the misoperation of the negative sequence direction element, a prevention strategy was formulated and subsequently validated using a Real-Time Hardware-in-the-Loop (RT HIL) setup.
3. In Chapter 5, The DOCR coordination approach was explored. The numerical iteration method was compared against optimization algorithms such as Genetic Algorithms and Particle Swarm Optimization. The analysis revealed the superiority of optimization algorithms over the numerical iteration method and highlighted Particle Swarm Optimization as particularly advantageous over Genetic Algorithms in addressing DOCR coordination challenges. The findings further presented how improving the coordination approach, such as modifying the PSO optimization algorithm, could minimize the operating time of DOCRs. This chapter presents an opportunity to develop advanced optimization algorithms to minimize DOCR operating time while maintaining coordination.
4. In Chapter 6, the impact of an increased interconnected network with a bidirectional fault contribution on DOCR coordination was presented and investigated. To prevent DOCR miscoordination, a novel dynamic relay coordination approach capable of adjusting to variations of fault current

during fault isolation was presented and validated; the proposed formulation enhances the reliability of DOCR in a mesh network

5. In Chapter 7, we delved into two critical protection coordination challenges. Firstly, we examined the stability concerns encountered by DGs within a network featuring DOCRs. Secondly, we investigated the instances of DOCR misoperations resulting from network topology and operation changes. To tackle these issues effectively, we proposed a resilient co-optimization strategy. This strategy ensured the stability of DGs and seamlessly adapted to the changes in network topology and changes in short circuit capacity while minimizing DOCR operating times. We validated the efficacy of this strategy using the IEEE test system.

8.3 Recommendations and Future Directions

This work introduced formulations and solution strategies to prevent protection scheme misoperations and address DOCR miscoordination issues. Additionally, this section explores potential avenues for future research and acknowledges certain limitations inherent in this study.

1. The investigation and the proposed strategies developed in this dissertation were investigated and validated on IEEE test systems and HIL setups; however, real-world implementation and validation of these strategies would enhance understanding of their practical feasibility.
2. The impact of inverter control architecture on protection scheme was investigated in this dissertation, but it does not delve into improving or modifying the inverter control architecture to prevent misoperation or miscoordination of relays; hence, more research should be on adapting inverter controls to address protection misoperations, such as those involving negative sequence direction element. For instance, exploring the potential for

inverters to produce inductive negative sequence fault currents while offering voltage ride-through support during fault conditions could be an ideal solution.

3. In this dissertation, the DOCR coordination studies were done considering the presence of synchronous machine-based distributed generators. Given the prevalence of Inverter-Based Distributed Generators (IBDGs), further studies are necessary to ensure effective relay coordination that does not depend on communication-based schemes, thereby reducing cost implications.
4. This dissertation improved DOCR coordination using advanced coordination formulations and clustering-based optimization algorithms. Clustering, an unsupervised machine learning technique, yielded promising results. Therefore, exploring other machine learning algorithms and hybrid approaches presents a potential path to enhancing relay coordination.

REFERENCES

- [1] Western Electricity Coordinating Council, “PCS 2022 Misoperation Report,” 2022. Accessed: 2023-09-24.
- [2] “Technical connection rules for high-voltage (vde-ar-n 4120).” Available online, October 2018.
- [3] U.S. Energy Information Administration (EIA), “Eia projections on primary energy consumption,” 2023. Accessed on: November 1, 2023.
- [4] McKinsey & Company, “Modernizing the investment approach for electric grids,” Insert Year. Accessed on: Insert Access Date.
- [5] J. W. Busby, K. Baker, M. D. Bazilian, A. Q. Gilbert, E. Grubert, V. Rai, J. D. Rhodes, S. Shidore, C. A. Smith, and M. E. Webber, “Cascading risks: Understanding the 2021 winter blackout in texas,” *Energy Research Social Science*, vol. 77, p. 102106, 2021.
- [6] “Texas freeze winter storm 2021 death count.” <https://www.texasstandard.org/stories/texas-freeze-winter-storm-2021-death-count/>: :text=Texas November 1,2023.
- [7] E. B. Watson and A. H. Etemadi, “Modeling electrical grid resilience under hurricane wind conditions with increased solar and wind power generation,” *IEEE Transactions on Power Systems*, vol. 35, no. 2, pp. 929–937, 2020.
- [8] R. Rastgoufard, I. Leevongwat, and P. Rastgoufard, “Impact of hurricanes on gulf coast electric grid islanding of industrial plants,” in *2015 Clemson University Power Systems Conference (PSC)*, pp. 1–5, 2015.
- [9] J. Bruzgul and N. Weisenfeld, “Resilient power: How utilities can identify and effectively prepare for increasing climate risks, sl,” *ICF, Fairfax*, 2021.
- [10] P. H. Larsen, B. Boehlert, J. Eto, K. Hamachi-LaCommare, J. Martinich, and L. Rennels, “Projecting future costs to u.s. electric utility customers from power interruptions,” *Energy*, vol. 147, pp. 1256–1277, 2018.
- [11] “Decentralizing energy for a high-demand, low-carbon world,” *One Earth*, vol. 1, no. 4, pp. 388–391, 2019.
- [12] A. Hussain, V.-H. Bui, and H.-M. Kim, “Microgrids as a resilience resource and strategies used by microgrids for enhancing resilience,” *Applied Energy*, vol. 240, pp. 56–72, 2019.
- [13] X. Lu, J. Wang, and L. Guo, “Using microgrids to enhance energy security and resilience,” *The Electricity Journal*, vol. 29, no. 10, pp. 8–15, 2016.
- [14] A. Soroudi, P. Maghouli, and A. Keane, “Resiliency oriented integration of dsrs in transmission networks,” *IET Generation, Transmission & Distribution*, vol. 11, no. 8, pp. 2013–2022, 2017.

- [15] A. Majzoubi and A. Khodaei, "Application of microgrids in providing ancillary services to the utility grid," *Energy*, vol. 123, pp. 555–563, 2017.
- [16] Y. Huo and G. Gruosso, "Hardware-in-the-loop framework for validation of ancillary service in microgrids: Feasibility, problems and improvement," *IEEE Access*, vol. 7, pp. 58104–58112, 2019.
- [17] M. H. Gomes and J. T. Saraiva, "Allocation of reactive power support, active loss balancing and demand interruption ancillary services in microgrids," *Electric Power Systems Research*, vol. 80, no. 10, pp. 1267–1276, 2010.
- [18] S. S. Rangarajan, S. Sreejith, and S. Nigam, "Effect of distributed generation on line losses and network resonances," in *2014 International Conference on Advances in Electrical Engineering (ICAEE)*, pp. 1–6, IEEE, 2014.
- [19] A. Ogunjuyigbe, T. Ayodele, and O. Akinola, "Impact of distributed generators on the power loss and voltage profile of sub-transmission network," *Journal of Electrical Systems and Information Technology*, vol. 3, no. 1, pp. 94–107, 2016.
- [20] M. Delfanti, D. Falabretti, and M. Merlo, "Dispersed generation impact on distribution network losses," *Electric Power Systems Research*, vol. 97, pp. 10–18, 2013.
- [21] N. Acharya, P. Mahat, and N. Mithulananthan, "An analytical approach for dg allocation in primary distribution network," *Electric Power & Energy Systems*, vol. 28, pp. 669–678, 2006.
- [22] C. Wang and M. Nehrir, "Analytical approaches for optimal placement of distributed generation sources in power systems," *IEEE Transactions on Power Systems*, vol. 19, no. 4, pp. 2068–2076, 2004.
- [23] M. Reza, M. Gibescu, P. H. Schavemaker, W. L. Kling, and L. van der Sluis, "Transient stability impacts of a vertical-to-horizontal transformation of power systems," in *2005 IEEE Russia Power Tech*, pp. 1–6, 2005.
- [24] A. Azmy and I. Erlich, "Impact of distributed generation on the stability of electrical power system," in *IEEE Power Engineering Society General Meeting, 2005*, pp. 1056–1063 Vol. 2, 2005.
- [25] J. Slootweg and W. Kling, "Impacts of distributed generation on power system transient stability," in *IEEE Power Engineering Society Summer Meeting*, vol. 2, pp. 862–867 vol.2, 2002.
- [26] N. Rashidirad, M. Hamzeh, K. Sheshyekani, and E. Afjei, "An effective method for low-frequency oscillations damping in multibus dc microgrids," *IEEE Journal on Emerging and Selected Topics in Circuits and Systems*, vol. 7, no. 3, pp. 403–412, 2017.

- [27] H. Bevrani, T. Ise, and Y. Miura, "Virtual synchronous generators: A survey and new perspectives," *International Journal of Electrical Power Energy Systems*, vol. 54, pp. 244–254, 2014.
- [28] W. Wu, Y. Liu, Y. He, H. S.-H. Chung, M. Liserre, and F. Blaabjerg, "Damping methods for resonances caused by lcl-filter-based current-controlled grid-tied power inverters: An overview," *IEEE Transactions on Industrial Electronics*, vol. 64, no. 9, pp. 7402–7413, 2017.
- [29] O. E. Egbomwan, S. Liu, and H. Chaoui, "Twin delayed deep deterministic policy gradient (td3) based virtual inertia control for inverter-interfacing dgs in microgrids," *IEEE Systems Journal*, vol. 17, no. 2, pp. 2122–2132, 2023.
- [30] S. E. Sati, A. Al-Durra, H. Zeineldin, T. H. El-Fouly, and E. F. El-Saadany, "Adaptive virtual inertia and damping for frequency stability enhancement using a seamless compensator," in *2023 IEEE PES Conference on Innovative Smart Grid Technologies - Middle East (ISGT Middle East)*, pp. 1–5, 2023.
- [31] B. Motling, S. Paul, and S. H. Nee Dey, "Siting and sizing of dg unit to minimize loss in distribution network in the presence of dg generated harmonics," in *2020 International Conference on Emerging Frontiers in Electrical and Electronic Technologies (ICEFEET)*, pp. 1–5, 2020.
- [32] Y. Xu, S. Dong, L. Lin, S. Zhang, and H. Mao, "Optimal siting and sizing of distributed generation considering voltage stability fluctuation," in *2021 IEEE 4th International Electrical and Energy Conference (CIEEC)*, pp. 1–5, 2021.
- [33] M. Valavala, "Optimal placement and sizing of distributed generation for loss minimization using abc optimization," *International Journal of Applied Power Engineering (IJAPE)*, vol. 10, p. 347, 12 2021.
- [34] A. A. A. Aboelsood, A. Zidan, and F. E.-S. Ehab, "Optimal dg allocation in radial distribution systems with high penetration of non-linear loads," *Electric Power Components and Systems Taylor & Francis*, vol. 43, pp. 1487–1497, 2015.
- [35] X. Fang, H. Cui, E. Du, F. Li, and C. Kang, "Characteristics of locational uncertainty marginal price for correlated uncertainties of variable renewable generation and demands," *Applied Energy*, vol. 282, p. 116064, 2021.
- [36] K. Poplavskaya, J. Lago, and L. de Vries, "Effect of market design on strategic bidding behavior: Model-based analysis of european electricity balancing markets," *Applied Energy*, vol. 270, p. 115130, 2020.
- [37] R. Khatami, A. Al-Digs, and Y. C. Chen, "Frequency dynamics-aware real-time marginal pricing of electricity," *Electric Power Systems Research*, vol. 212, p. 108429, 2022.

- [38] J. Stekli, L. Bai, and U. Cali, "Pricing for reactive power and ancillary services in distribution electricity markets," in *2021 IEEE Power Energy Society Innovative Smart Grid Technologies Conference (ISGT)*, pp. 1–5, 2021.
- [39] K. Kauhaniemi and L. Kumpulainen, "Impact of distributed generation on the protection of distribution networks," in *2004 Eighth IEE International Conference on Developments in Power System Protection*, vol. 1, pp. 315–318 Vol.1, 2004.
- [40] M. Doyle, "Reviewing the impacts of distributed generation on distribution system protection," in *IEEE Power Engineering Society Summer Meeting*, vol. 1, pp. 103–105 vol.1, 2002.
- [41] A. Massoud, S. Ahmed, S. J. Finney, and B. Williams, "Inverter-based versus synchronous-based distributed generation; fault current limitation and protection issues," in *2010 IEEE Energy Conversion Congress and Exposition*, pp. 58–63, 2010.
- [42] M. Khederzadeh, H. Javadi, and S. M. A. Mousavi, "Source type impact of distributed generation (dg) on the distribution protection," 2010.
- [43] K. Maki, S. Repo, and P. Jarventausta, "Effect of wind power based distributed generation on protection of distribution network," in *2004 Eighth IEE International Conference on Developments in Power System Protection*, vol. 1, pp. 327–330 Vol.1, 2004.
- [44] R. Ogden and J. Yang, "Impacts of distributed generation on low-voltage distribution network protection," in *2015 50th International Universities Power Engineering Conference (UPEC)*, pp. 1–6, 2015.
- [45] H. Cheung, A. Hamlyn, L. Wang, C. Yang, and R. Cheung, "Investigations of impacts of distributed generations on feeder protections," in *2009 IEEE Power Energy Society General Meeting*, pp. 1–7, 2009.
- [46] P. M. Koumba, A. Ch̃riti, and M. L. Doumbia, "Impacts of distributed generation on the coordination of protective devices in distribution network," in *2015 IEEE 28th Canadian Conference on Electrical and Computer Engineering (CCECE)*, pp. 460–465, 2015.
- [47] T. Mashau, S. Kibaara, S. Chowdhury, and S. P. Chowdhury, "Impact of distributed generation on protection coordination in a radial distribution feeder," in *2011 46th International Universities' Power Engineering Conference (UPEC)*, pp. 1–5, 2011.
- [48] W. El-khattam and T. Sidhu, "Resolving the impact of distributed renewable generation on directional overcurrent relay coordination: a case study," *IET Renewable Power Generation*, 2008.
- [49] Å. Huchel, H. H. Zeineldin, and E. F. El-Saadany, "Protection coordination index enhancement considering multiple dg locations using fcl," *IEEE Transactions on Power Delivery*, vol. 32, no. 1, pp. 344–350, 2017.

- [50] M. Hojjaty, B. Fani, and I. Sadeghkhani, "Intelligent protection coordination restoration strategy for active distribution networks," *IET Generation, Transmission & Distribution*, vol. 16, no. 3, pp. 397–413, 2022.
- [51] A. Hatata, A. Ebeid, and M. El-Saadawi, "Optimal restoration of directional overcurrent protection coordination for meshed distribution system integrated with dgs based on fcls and adaptive relays," *Electric Power Systems Research*, vol. 205, p. 107738, 2022.
- [52] B. Fani, M. Dadkhah, and A. Karami-Horestani, "An adaptive protection coordination scheme against the staircase fault current waveforms in pv dominated distribution systems," *IET Generation, Transmission Distribution*, vol. 12, 02 2018.
- [53] "Ieee standard for interconnection and interoperability of distributed energy resources with associated electric power systems interfaces," *IEEE Std 1547-2018 (Revision of IEEE Std 1547-2003)*, pp. 1–138, 2018.
- [54] "Ieee standard for interconnection and interoperability of inverter-based resources (ibrs) interconnecting with associated transmission electric power systems," *IEEE Std 2800-2022*, pp. 1–180, 2022.
- [55] A. Samadi, R. M. Chabanloo, M. Farrokhifar, and D. Pozo, "Adaptive coordination of overcurrent relays considering setting changes minimization to improve protection system's reliability," in *2020 IEEE PES Innovative Smart Grid Technologies Europe (ISGT-Europe)*, (The Hague, Netherlands), pp. 414–418, 2020.
- [56] L. Huchel and H. Zeineldin, "Planning the coordination of directional overcurrent relays for distribution systems considering dg," *IEEE Transactions on Smart Grid*, vol. 7, pp. 1–1, 2015.
- [57] B. Fani, H. Bisheh, and A. Karami-Horestani, "An offline penetration-free protection scheme for pv-dominated distribution systems," *Electric Power Systems Research*, vol. 157, pp. 1–9, 2018.
- [58] M. Mashayekhi, M. Meskin, and A. Farahbakhsh, "Impact of size and location of distributed generation on overcurrent relays in active distribution networks," in *2017 North American Power Symposium (NAPS)*, pp. 1–6, 2017.
- [59] A. Haddadi, M. Zhao, I. Kocar, U. Karaagac, K. W. Chan, and E. Farantatos, "Impact of inverter-based resources on negative sequence quantities-based protection elements," *IEEE Transactions on Power Delivery*, vol. 36, no. 1, pp. 289–298, 2021.
- [60] K. Jia, Z. Yang, Y. Fang, T. Bi, and M. Sumner, "Influence of inverter-interfaced renewable energy generators on directional relay and an improved scheme," *IEEE Transactions on Power Electronics*, vol. 34, no. 12, pp. 11843–11855, 2019.

- [61] H. Ebrahimi, A. Yazdaninejadi, S. Golshannavaz, and S. Teimourzadeh, "An ens-oriented voltage protection scheme for inverter-based generators in active distribution networks," *IEEE Transactions on Smart Grid*, vol. 13, no. 4, pp. 2639–2649, 2022.
- [62] K. R. B. Belwin J. Brearley, R. Raja Prabu and V. Sankaranarayanan, "Adaptive relay co-ordination scheme for radial microgrid," *International Journal of Ambient Energy*, vol. 43, no. 1, pp. 2180–2193, 2022.
- [63] K. Sedghisigarchi and K. T. Sardari, "An adaptive protection strategy for reliable operation of microgrids," in *2018 IEEE International Energy Conference (ENERGYCON)*, (Limassol, Cyprus), pp. 1–6, 2018.
- [64] W. El-Khattam and T. S. Sidhu, "Restoration of directional overcurrent relay coordination in distributed generation systems utilizing fault current limiter," *IEEE Transactions on Power Delivery*, vol. 23, no. 2, pp. 576–585, 2008.
- [65] G. Tang and M. Iravani, "Application of a fault current limiter to minimize distributed generation impact on coordinated relay protection," in *int. conf. power systems transients, Montreal, QC, Canada*, pp. 19–23, 2005.
- [66] C. Ten and P. Crossley, "Evaluation of rocof relay performances on networks with distributed generation," in *2008 IET 9th International Conference on Developments in Power System Protection (DPSP 2008)*, pp. 523–528, 2008.
- [67] Z. Wang, J. Xiong, and X. Wang, "Investigation of frequency oscillation caused false trips for biomass distributed generation," *IEEE Transactions on Smart Grid*, vol. 10, no. 6, pp. 6092–6101, 2019.
- [68] M. Tasdighi and M. Kezunovic, "Preventing transmission distance relays maloperation under unintended bulk dg tripping using svm-based approach," *Electric Power Systems Research*, vol. 142, pp. 258–267, 2017.
- [69] M. H. Bollen and F. Hassan, *Integration of distributed generation in the power system*, vol. 80. John wiley & sons, 2011.
- [70] A. Hooshyar, M. A. Azzouz, and E. F. El-Saadany, "Distance protection of lines emanating from full-scale converter-interfaced renewable energy power plantsâpart i: Problem statement," *IEEE Transactions on Power Delivery*, vol. 30, no. 4, pp. 1770–1780, 2015.
- [71] Y. Feng, Z. Zhang, Q. Lai, X. Yin, and H. Liu, "Impact of inverter interfaced generators on distance protection," in *2019 4th International Conference on Intelligent Green Building and Smart Grid (IGBSG)*, pp. 512–515, 2019.
- [72] A. Hooshyar and R. Iravani, "A new directional element for microgrid protection," *IEEE Transactions on Smart Grid*, vol. 9, no. 6, pp. 6862–6876, 2018.

- [73] O. Adeosun, M. F. Rahman, E. Shoubaki, V. Cecchi, and M. Manjrekar, "Effect of inverter-interfaced distributed generation on negative sequence directional element using typhoon real-time hardware in the loop (hil)," in *2021 IEEE Applied Power Electronics Conference and Exposition (APEC)*, pp. 2097–2104, 2021.
- [74] F. T. Dai, "Impacts of distributed generation on protection and autoreclosing of distribution networks," in *10th IET International Conference on Developments in Power System Protection (DPSP 2010)*, (Manchester, UK), pp. 1–5, 2010.
- [75] O. Adeosun and V. Cecchi, "Enhancing overcurrent relay coordination to address power system operational and topological changes," *2024 IEEE Texas Power and Energy Conference (TPEC)*, 2024. Manuscript submitted for publication.
- [76] S. Das, S. Santoso, and A. Maitra, "Effects of distributed generators on impedance-based fault location algorithms," in *2014 IEEE PES General Meeting Conference Exposition*, (National Harbor, MD), pp. 1–5, 2014.
- [77] B. D. S. Joshi, P. A. H. Cavalcante, F. C. L. Trindade, and et al., "Analysis of distance-based fault location methods for smart grids with distributed generation," in *IEEE PES ISGT Europe 2013*, (Lyngby, Denmark), pp. 1–5, 2013.
- [78] S. M. Saad, N. E. Naili, and F. A. Mohamed, "Investigating the effect of dg infeed on the effective cover of distance protection scheme in mixed-mv distribution network," *International Journal of Renewable Energy Development*, vol. 7, no. 3, pp. 223–231, 2018.
- [79] Y. Fang, K. Jia, Z. Yang, Y. Li, and T. Bi, "Impact of inverter-interfaced renewable energy generators on distance protection and an improved scheme," *IEEE Transactions on Industrial Electronics*, vol. 66, no. 9, pp. 7078–7088, 2019.
- [80] A. M. Tsimtsios, G. N. Korres, and V. C. Nikolaidis, "A pilot-based distance protection scheme for meshed distribution systems with distributed generation," *International Journal of Electrical Power Energy Systems*, vol. 105, pp. 454–469, 2019.
- [81] Q. Jia, X. Dong, and S. Mirsaeidi, "A traveling-wave-based line protection strategy against single-line-to-ground faults in active distribution networks," *International Journal of Electrical Power Energy Systems*, vol. 107, pp. 403–411, 2019.
- [82] L. Lessa, C. Grilo, A. Moraes, D. Coury, and R. Fernandes, "A travelling wave-based fault locator for radial distribution systems using decision trees to mitigate multiple estimations," *Electric Power Systems Research*, vol. 223, p. 109646, 2023.
- [83] M. Miranbeigi, P. M. Gajare, J. Benzaquen, P. Kandula, and D. Divan, "On the passivity of grid-forming converters â role of virtual impedance,"

in *2022 IEEE Applied Power Electronics Conference and Exposition (APEC)*, pp. 650–656, 2022.

- [84] F. G  thner, O.-M. Midtg  rd, R. Torres-Olguin, and S. D  Arco, “Effect of including transient virtual impedance in droop-controlled microgrids,” in *2018 IEEE International Conference on Environment and Electrical Engineering and 2018 IEEE Industrial and Commercial Power Systems Europe (EEEIC / ICPS Europe)*, pp. 1–6, 2018.
- [85] V. Skiparev, K. Nosrati, A. Tepljakov, E. Petlenkov, Y. Levron, J. Belikov, and J. M. Guerrero, “Virtual inertia control of isolated microgrids using an nn-based vfopid controller,” *IEEE Transactions on Sustainable Energy*, vol. 14, no. 3, pp. 1558–1568, 2023.
- [86] S. Stankovi  , T. Van Cutsem, and L. S  der, “Fault-current injection strategies of inverter-based generation for fast voltage recovery,” *IEEE Transactions on Power Systems*, vol. 37, no. 2, pp. 1543–1553, 2022.
- [87] “Misoperation information data analysis system data reporting instructions.” Effective: January 1, 2021, North American Reliability Corporation.
- [88] O. Adeosun and V. Cecchi, “Investigation of the impact of inverter-based generators on protection schemes,” in *SoutheastCon 2022*, pp. 1–7, 2022.
- [89] Y. Chi, Y. Liu, W. Wang, M. Chen, and H. Dai, “Study on impact of wind power integration on power system,” *Power System Technology*, vol. 03, pp. 77–81, 2007.
- [90] V. Akhmatov, “Analysis of dynamic behavior of electric power systems with large amount of wind power,” 2003.
- [91] J. Mohammadi, S. Afsharnia, S. Vaez-Zadeh, and S. Farhangi, “Improved fault ride through strategy for doubly fed induction generator-based wind turbines under both symmetrical and asymmetrical grid faults,” *Renewable Power Generation IET*, vol. 10, no. 8, pp. 1114–1122, 2016.
- [92] C. Wessels, F. Gebhardt, and F. W. Fuchs, “Fault ride-through of a dfig wind turbine using a dynamic voltage restorer during symmetrical and asymmetrical grid faults,” *IEEE Transactions on Power Electronics*, vol. 26, pp. 807–815, March 2011.
- [93] X. Xie, X. Zhang, X. Zhang, S. Yang, and L. Wang, “Improved ride-through control of dfig during grid voltage swell,” *IEEE Transactions on Industrial Electronics*, vol. 62, pp. 3584–3594, Jun. 2015.
- [94] J. Liang, D. F. Howard, J. A. Restrepo, and R. G. Harley, “Feedforward transient compensation control for dfig wind turbines during both balanced and unbalanced grid disturbances,” *IEEE Transactions on Industry Applications*, vol. 49, pp. 1452–1463, May-June 2013.
- [95] U. Karaagac, J. Mahseredjian, H. Gras, H. Saad, J. Peralta, and L. Belomo, “Simulation models for wind parks with variable speed wind turbines in emtpv,” tech. rep., Polytechnique Montr  al, 2017.

- [96] T. Kauffmann, "Modeling of wind parks for steady state short circuit studies," tech. rep., 2018.
- [97] B. Chen, A. Shrestha, F. A. Ituzaro, and N. Fischer, "Addressing protection challenges associated with type 3 and type 4 wind turbine generators," in *2015 68th Annual Conference for Protective Relay Engineers*, pp. 335–344, 2015.
- [98] E. O. Schweitzer III and J. Roberts, "Distance relay element design," in *19th Annual Western Protective Relay Conference*, (Spokane, WA), October 1992.
- [99] "Virtual hil device - typhoon hil." [Online].
- [100] O. Adeosun and V. Cecchi, "Optimal coordination of directional overcurrent relays using numerical iterative method," in *2023 IEEE Texas Power and Energy Conference (TPEC)*, pp. 1–6, 2023.
- [101] Schweitzer Engineering Laboratories, Inc., *SEL-651R-2 Recloser Control Instruction Manual*, 2012-2022. [Online]. Available: Accessed Jan. 30, 2024.
- [102] J. L. Blackburn and T. J. Domin, *Protective Relaying: Principles and Applications*. Power Engineering, Boca Raton, FL: CRC Press, 3 ed., 2006.
- [103] Y. Wu and Q. Song, "Improved particle swarm optimization algorithm in power system network reconfiguration," *Mathematical Problems in Engineering*, vol. 2021, pp. 1–10, Mar. 2021.
- [104] O. Adeosun and V. Cecchi, "Optimal coordination of directional overcurrent relays using numerical iterative method," pp. 1–6, 2023.
- [105] A. A. El-Fergany and H. M. Hasanien, "Water cycle algorithm for optimal overcurrent relays coordination in electric power systems," *Soft Computing*, 2019.
- [106] M. M. Mansour, S. F. Mekhamer, and N. E. S. El-Kharbawe, "A modified particle swarm optimizer for the coordination of directional overcurrent relays," *IEEE Transactions on Power Delivery*, vol. 22, no. 3, pp. 1400–1410, 2007.
- [107] A. J. Urdaneta, L. G. Perez, and H. Restrepo, "Optimal coordination of directional overcurrent relays considering dynamic changes in the network topology," *IEEE Transactions on Power Delivery*, vol. 12, pp. 1458–1464, Oct. 1997.
- [108] K. A. Saleh and A. Mehrizi-Sani, "Multi-stage protection coordination optimization for distribution systems with topology changes," in *2020 IEEE/PES Transmission and Distribution Conference and Exposition (TD)*, pp. 1–5, 2020.
- [109] F. A. Albasri, A. R. Alroomi, and J. H. Talaq, "Optimal coordination of directional overcurrent relays using biogeography-based optimization

- algorithms,” *IEEE Transactions on Power Delivery*, vol. 30, pp. 1810–1820, Aug. 2015.
- [110] O. Adeosun and V. Cecchi, “Addressing overcurrent relay miscoordination caused by network topology changes during fault isolation,” in *2023 North American Power Symposium (NAPS)*, pp. 1–6, 2023.
 - [111] O. Adeosun and V. Cecchi, “A dynamic approach for co-optimization of dg stability and directional overcurrent relay coordination.” Manuscript Ref. No. EPSR-D-24-0137, submitted to *Electric Power Systems Research Transaction* (under review, revise and resubmit), 2024.
 - [112] “Ieee standard for inverse-time characteristics equations for overcurrent relays,” *IEEE Std C37.112-2018 (Revision of IEEE Std C37.112-1996)*, pp. 1–25, 2019.
 - [113] O. Adeosun and V. Cecchi, “Enhancing overcurrent relay coordination to address power system operational and topological changes,” in *2024 IEEE Texas Power and Energy Conference (TPEC)*, pp. 1–6, 2024.
 - [114] O. Adeosun and V. Cecchi, “Strategic optimization of relay coordination considering power system operation and topology changes,” *IEEE Industry Applications Society Transactions*, 2024. Manuscript submitted for review in March 2024 (Corresponding Author: O. Adeosun, V. Cecchi).
 - [115] J. S. Farkhani, M. Zareein, H. Soroushmehr, and H. Mortazavi, “Protection coordination constraints of distributed generation in transient stability,” in *2019 5th Conference on Knowledge Based Engineering and Innovation (KBEI)*, (Tehran, Iran), pp. 275–280, 2019.
 - [116] A. Narimani and H. Hashemi-Dezaki, “Optimal stability-oriented protection coordination of smart grids directional overcurrent relays based on optimized tripping characteristics in double-inverse model using high-set relay,” *International Journal of Electrical Power & Energy Systems*, vol. 133, p. 107249, 2021.
 - [117] T. S. Aghdam, H. K. Karegar, and H. H. Zeineldin, “Optimal coordination of double-inverse overcurrent relays for stable operation of dgs,” *IEEE Transactions on Industrial Informatics*, vol. 15, pp. 183–192, Jan 2019.
 - [118] A. K. Summers, R. C. Mathews, T. Patel, and M. J. Reno, “Power system protection parameter sensitivity analysis with integrated inverter based resources,” in *2021 IEEE 48th Photovoltaic Specialists Conference (PVSC)*, 2021.
 - [119] V. C. Nikolaidis, E. Papanikolaou, and A. S. Safigianni, “A communication-assisted overcurrent protection scheme for radial distribution systems with distributed generation,” *IEEE Transactions on Smart Grid*, vol. 7, pp. 114–123, Jan 2016.
 - [120] R. M. Chabanloo, M. Safari, and R. G. Roshanagh, “Reducing the scenarios of network topology changes for adaptive coordination of overcurrent

relays using hybrid ga-lp,” *IET Generation, Transmission & Distribution*, vol. 12, no. 21, pp. 5879–5890, 2018.

- [121] M. Ojaghi and V. Mohammadi, “Use of clustering to reduce the number of different setting groups for adaptive coordination of overcurrent relays,” *IEEE Transactions on Power Delivery*, vol. 33, pp. 1204–1212, June 2018.
- [122] F. Pedregosa, G. Varoquaux, A. Gramfort, V. Michel, B. Thirion, O. Grisel, M. Blondel, P. Prettenhofer, R. Weiss, V. Dubourg, J. Vanderplas, A. Passos, D. Cournapeau, M. Brucher, M. Perrot, and E. Duchesnay, “Scikit-learn: Machine learning in python,” *Journal of Machine Learning Research*, vol. 12, pp. 2825–2830, 2011.
- [123] K. Panchal, “Performance metrics in machine learning â part 3: Clustering.” Towards Data Science, June 2020.

APPENDIX A: Chapter 5 Data and Results

This shows the data and results used for the investigation and work in chapter 5

A.1 9-Bus System Data and Results

Table A.1: 9-Bus System: Nominal Current

Relay	Nominal Current (A)	Relay	Nominal Current (A)
F2	210	R2	0
F3	122	R3	0
F4	0	R4	14
F5	0	R5	100
F6	0	R6	150
F7	0	R7	14
F8	0	R8	43
F9	0	R9	175

Table A.2: 9-Bus System: Relay Settings (Time Dial Setting (TDS) and Pickup (I_p)) obtained from Numerical Iteration, GA, and CIW-PSO

Relay	Numerical Iteration		GA		CIW-PSO	
	TDS	I_p	TDS	I_p	TDS	I_p
F1	3.805	247.000	0.102	1436.130	0.348	792.986
F2	2.822	263.000	0.100	1053.974	0.100	1002.565
F3	2.997	152.000	0.103	785.585	0.100	765.203

Continued on next page

Table A.2 – continued from previous page

Relay	Numerical Iteration		GA		CIW-PSO	
	TDS	I_p	TDS	I_p	TDS	I_p
F4	3.701	17.000	0.721	308.485	0.100	605.176
F5	1.319	125.000	0.101	489.095	1.248	121.108
F6	0.100	187.000	0.100	178.468	0.100	180.041
F7	3.806	218.000	0.100	1307.784	0.101	1390.907
F8	3.908	53.000	0.672	407.909	1.848	118.359
F9	1.000	16.000	0.100	223.318	0.100	210.010
R1	0.100	247.000	0.102	252.674	0.100	237.600
R2	0.330	263.000	0.259	262.901	0.168	301.261
R3	1.721	152.000	0.102	476.153	0.100	472.271
R4	6.158	17.000	0.100	635.098	0.100	610.578
R5	5.714	125.000	0.349	541.230	0.100	857.847
R6	6.555	187.000	0.164	1267.251	0.666	620.962
R7	3.728	218.000	0.100	368.675	0.746	420.283
R8	9.304	53.000	1.850	348.761	0.217	920.921
R9	6.510	16.000	0.100	1627.416	0.118	1395.364

Table A.3: 9-Bus System: Relay Settings (Time Dial Setting (TDS) and Pickup (I_p)) obtained from LIW-PSO and EIW-PSO (9-Bus System)

Relay	LIW-PSO		EIW-PSO	
	TDS	I_p	TDS	I_p
F1	0.100	1265.236	0.100	1349.399
F2	0.100	1005.200	0.100	1016.259
Continued on next page				

Table A.3 – continued from previous page

Relay	LIW-PSO		EIW-PSO	
	TDS	I_p	TDS	I_p
F3	0.100	774.584	0.100	774.990
F4	0.594	313.276	0.680	292.366
F5	0.100	489.022	0.100	489.011
F6	0.100	180.000	0.100	180.000
F7	0.100	1469.894	0.100	1310.856
F8	0.100	953.159	0.650	387.590
F9	0.100	210.000	0.100	210.000
R1	0.100	237.603	0.100	237.600
R2	0.252	252.000	0.252	252.000
R3	0.100	471.682	0.100	471.685
R4	0.100	610.173	0.100	610.285
R5	0.100	823.068	0.340	530.783
R6	0.209	1007.378	0.159	1207.787
R7	0.100	351.426	0.100	345.377
R8	0.227	907.114	1.783	332.249
R9	0.100	1395.364	0.100	1510.983

Table A.4: 9-Bus System: Relay Operating Time and CTI obtained from Numerical Iteration Approach

Coordination Pair	Numerical Iteration		
	BR Time (Sec)	PR Time (Sec)	CTI (Sec)
Pair 1	0.82	0.385	0.435
Continued on next page			

Table A.4 – continued from previous page

Coordination Pair	Numerical Iteration		
	BR Time (s)	PR Time (s)	CTI (s)
Pair 2	0.895	0.435	0.46
Pair 3	0.711	0.46	0.251
Pair 4	0.283	0.251	0.032
Pair 5	0.477	0.032	0.445
Pair 6	0.657	0.445	0.212
Pair 7	0.309	0.212	0.097
Pair 8	0.482	0.097	0.385
Pair 9	0.4	0.385	0.015
Pair 10	0.324	0.015	0.309
Pair 11	0.701	0.309	0.392
Pair 12	0.991	0.392	0.599
Pair 13	1.238	0.599	0.639
Pair 14	0.654	0.639	0.015
Pair 15	0.44	0.015	0.425
Pair 16	0.853	0.425	0.428
Pair 17	5.951	0.428	5.523
Total Time	16.186	5.524	10.662

Table A.5: 9-Bus System: Relay Operating Time and CTI obtained from Genetic Algorithm and CIW-PSO

Coordination Pair	GA			CIW-PSO		
	BR Time (s)	PR Time (s)	CTI (s)	BR Time (s)	PR Time (s)	CTI (s)
Pair 1	0.473	0.100	0.374	0.292	0.077	0.215
Pair 2	0.665	0.275	0.390	0.390	0.187	0.202
Pair 3	0.761	0.430	0.331	0.558	0.358	0.200
Pair 4	0.617	0.232	0.385	0.430	0.230	0.200
Pair 5	0.325	0.112	0.213	0.230	0.030	0.200
Pair 6	0.399	0.061	0.339	0.292	0.047	0.245
Pair 7	1.307	0.250	1.057	1.042	0.217	0.825
Pair 8	0.507	0.038	0.468	0.217	0.017	0.200
Pair 9	0.613	0.131	0.482	0.277	0.077	0.200
Pair 10	0.468	0.065	0.404	0.215	0.015	0.200
Pair 11	0.526	0.225	0.301	0.417	0.215	0.202
Pair 12	0.515	0.220	0.295	0.390	0.190	0.200
Pair 13	0.661	0.204	0.457	0.487	0.187	0.300
Pair 14	0.633	0.154	0.480	0.335	0.099	0.236
Pair 15	0.490	0.106	0.384	3.272	0.015	3.257
Pair 16	0.660	0.345	0.315	0.529	0.326	0.203
Pair 17	0.797	0.327	0.470	0.499	0.298	0.201
Total Time	10.418	3.275	7.144	9.872	2.585	7.286

Table A.6: IEEE-33-Bus System: Nominal Current

Relay	Nominal Current (A)	Relay	Nominal Current (A)	Relay	Nominal Current (A)	Relay	Nominal Current (A)
F1	163.87	F21	21.8	R9	10.31	F21B	0
F2	108.47	F22	17.69	R12	19.7	F15B	0
F3	58.73	F25	0	R15	9.07	F9B	0
F6	20.97	F29	46.16	R21	0	F29B	0
F8	13.07	F33	0	R22	0	F3B	46.1
F9	10.31	R3	0	R25	0	F6B	29.72
F12	19.8	R6	0	R29	0		
F15	9.08	R8	14	R33	0		
F12B	0	F8B	0	F2B	50.62		

Table A.7: IEEE 33-Bus System: Relay Settings (Time Dial Setting (TDS) and Pickup (I_p)) obtained from CIW-PSO, LIW-PSO, and EIW-PSO

	CIW-PSO		LIW-PSO		EIW-PSO	
	TDS	Ip (A)	TDS	Ip (A)	TDS	Ip (A)
F1	0.203	1292.415	0.252	1395.556	0.117	1544.123
F2	0.414	1554.294	0.291	1993.332	0.231	1186.638
F3	0.210	1074.041	0.230	897.532	0.160	629.985
F6	0.572	400.141	1.298	93.869	0.289	530.521
F8	0.373	660.736	0.213	668.745	0.101	526.961
F9	1.815	100.507	0.765	23.538	1.133	26.172
F12	0.124	702.866	0.136	485.436	0.100	687.035
F15	1.246	181.960	0.808	211.112	0.803	139.714
F21	0.372	623.374	0.574	430.169	0.538	429.023
F22	0.518	513.196	1.150	193.595	0.401	164.653
F25	0.100	4.066	0.100	1.316	0.100	1.900
F29	0.363	205.012	0.522	409.001	0.869	411.298
F33	0.100	2.789	0.100	5.714	0.100	1.139
R3	0.288	19.611	1.806	10.788	0.846	133.123
R6	0.170	69.594	0.515	36.707	0.885	98.569
R8	0.777	315.899	1.965	147.564	1.161	155.636
R9	0.800	55.033	0.607	39.346	1.081	117.067
R12	1.230	104.899	0.389	309.108	0.609	269.459
R15	0.128	30.018	0.394	53.415	0.748	143.465
R21	0.591	41.384	0.315	41.395	0.890	26.581
R25	0.100	0.411	0.100	3.908	0.100	0.251
R29	0.659	182.191	0.719	121.605	0.543	183.657
R33	0.952	78.418	0.516	81.666	0.516	39.082
F21B	0.100	2.273	0.100	6.158	0.100	0.255
F15B	0.100	4.199	0.100	1.004	0.100	0.549
F9B	0.100	5.501	0.100	0.947	0.100	1.018
F29B	0.100	1.101	0.100	0.592	0.100	0.504
F3B	0.323	678.824	1.160	220.981	0.824	424.633
F6B	0.288	828.637	0.250	759.708	0.106	722.922
F8B	0.100	29.013	0.100	8.765	0.100	1.126
F2B	0.380	891.066	0.357	845.223	0.202	508.289
F12B	0.100	1.914	0.100	2.883	0.100	0.923

Table A.8: IEEE 33-Bus System: Relay Operating Time and CTI obtained from Numerical Iteration Approach

Coordination Pair	BR Time (s)	PR Time (s)	CTI (s)
Pair 1	0.4762308	0.088124	0.3881067
Pair 2	1.9276109	0.0683789	1.8592319
Pair 3	0.4018964	0.0388033	0.3630931
Pair 4	1.2168218	0.4053462	0.8114756
Pair 5	0.7661669	0.1407159	0.625451
Pair 6	0.4235022	0.1873167	0.2361855
Pair 7	0.754029	0.3246092	0.4294198
Pair 8	2.2219923	0.3509788	1.8710135
Pair 9	1.9322385	0.2092733	1.7229652
Pair 10	1.4087139	0.1589097	1.2498042
Pair 11	0.9362765	0.2731555	0.6631211
Pair 12	0.5615539	0.1151514	0.4464025
Pair 13	0.4098425	0.0663843	0.3434582
Pair 14	1.2807593	0.4071932	0.8735661
Pair 15	0.5942773	0.0406317	0.5536456
Pair 16	1.1111904	0.675203	0.4359869
Pair 17	2.4933061	0.176318	2.3169881
Pair 18	0.5282153	0.117494	0.4107218
Pair 19	0.468557	0.035298	0.4332588
Pair 20	0.454688	0.017151	0.4375371
Pair 21	1.7872754	0.016447	1.7708288
Pair 22	0.5497376	0.109288	0.4404492
Pair 23	2.2371199	0.122211	2.1149086
Pair 24	0.967211	0.214502	0.752709
Pair 25	0.6195742	0.005035	0.6145396
Pair 26	0.4970228	0.06269	0.4343326
Pair 27	0.6086462	0.054622	0.5540245
Pair 28	1.0738388	0.080971	0.9928673
Pair 29	0.4419283	0.053751	0.3881775
Pair 30	2.0419128	0.054765	1.9871479
Pair 31	0.6314809	0.118206	0.5132747
Pair 32	0.9854342	0.052367	0.9330677
Pair 33	1.4404598	0.058602	1.3818575
Pair 34	0.4014508	0.034596	0.366855
Pair 35	0.408907	0.0665	0.3424072
Pair 36	0.9522423	0.056477	0.8957652
Total Operating Time (s)	36.01211	5.057466	30.95464

Table A.9: IEEE 33-Bus System: Relay Operating Time and CTI obtained from Genetic Algorithm (GA) and CIW-PSO

Coordination Pair	GA			CIW-PSO		
	BR Time(s)	PR Time(s)	CTI (s)	BR Time(s)	PR Time (s)	CTI (s)
Pair 1	0.647	0.049	0.598	0.287	0.051	0.236
Pair 2	0.339	0.069	0.270	1.904	0.055	1.848
Pair 3	0.523	0.067	0.456	0.430	0.057	0.373
Pair 4	0.463	0.263	0.200	1.012	0.255	0.757
Pair 5	0.980	0.119	0.860	0.799	0.120	0.678
Pair 6	0.823	0.124	0.699	0.303	0.110	0.193
Pair 7	0.292	0.241	0.051	0.673	0.288	0.384
Pair 8	0.685	0.218	0.468	1.592	0.329	1.262
Pair 9	1.417	0.171	1.245	1.448	0.197	1.251
Pair 10	1.685	0.238	1.447	1.029	0.192	0.837
Pair 11	1.171	0.293	0.877	0.719	0.212	0.507
Pair 12	0.655	0.099	0.556	0.446	0.090	0.357
Pair 13	0.415	0.063	0.352	0.466	0.078	0.389
Pair 14	0.735	0.535	0.200	0.885	0.418	0.467
Pair 15	1.175	0.058	1.116	0.441	0.054	0.387
Pair 16	0.654	0.454	0.200	1.328	0.586	0.742
Pair 17	1.303	0.197	1.106	1.479	0.198	1.281
Pair 18	1.689	0.170	1.519	0.503	0.123	0.380
Pair 19	0.594	0.025	0.569	0.304	0.033	0.271
Pair 20	0.379	0.017	0.362	0.380	0.022	0.359
Pair 21	0.399	0.025	0.374	1.337	0.021	1.316
Pair 22	1.279	0.070	1.208	0.404	0.102	0.301
Pair 23	0.551	0.087	0.464	1.549	0.087	1.462
Pair 24	1.460	0.145	1.315	0.707	0.159	0.548
Pair 25	0.682	0.008	0.674	0.499	0.007	0.492
Pair 26	0.585	0.046	0.539	0.505	0.067	0.438
Pair 27	0.473	0.065	0.407	0.569	0.048	0.521
Pair 28	0.513	0.066	0.446	0.903	0.057	0.846
Pair 29	1.001	0.073	0.928	0.265	0.062	0.203
Pair 30	0.511	0.078	0.433	1.842	0.071	1.771
Pair 31	1.580	0.189	1.391	0.589	0.151	0.438
Pair 32	0.579	0.050	0.529	0.967	0.044	0.923
Pair 33	0.825	0.050	0.775	0.997	0.041	0.956
Pair 34	1.268	0.050	1.218	0.365	0.030	0.335
Pair 35	0.287	0.050	0.237	0.374	0.061	0.312
Pair 36	0.491	0.050	0.441	0.757	0.065	0.693
Total Operating Time	29.106	4.575	24.531	29.055	4.541	24.514

Table A.10: IEEE 33-Bus System: Relay Operating Time and CTI obtained from LIW-PSO and EIW-PSO

Coordination Pair	LIW-PSO			EIW-PSO		
	BR Time(s)	PR Time(s)	CTI (s)	BR Time(s)	PR Time (s)	CTI (s)
Pair 1	0.324	0.073	0.251	0.264	0.064	0.200
Pair 2	1.095	0.060	1.035	1.120	0.064	1.056
Pair 3	0.281	0.052	0.230	0.254	0.050	0.204
Pair 4	0.573	0.329	0.244	0.645	0.330	0.315
Pair 5	0.606	0.092	0.515	0.491	0.101	0.390
Pair 6	0.327	0.127	0.200	0.211	0.140	0.071
Pair 7	0.702	0.327	0.376	0.511	0.295	0.216
Pair 8	1.319	0.337	0.982	1.295	0.295	1.000
Pair 9	1.192	0.160	1.032	1.035	0.165	0.870
Pair 10	1.048	0.174	0.874	0.770	0.181	0.589
Pair 11	0.552	0.287	0.265	0.453	0.252	0.201
Pair 12	0.342	0.068	0.274	0.292	0.092	0.200
Pair 13	0.341	0.048	0.293	0.274	0.064	0.210
Pair 14	0.781	0.366	0.414	0.680	0.456	0.224
Pair 15	0.416	0.055	0.361	0.287	0.046	0.241
Pair 16	1.161	0.555	0.606	0.776	0.568	0.208
Pair 17	1.223	0.172	1.051	1.255	0.167	1.088
Pair 18	0.387	0.170	0.217	0.367	0.167	0.200
Pair 19	0.320	0.025	0.295	0.229	0.029	0.200
Pair 20	0.271	0.015	0.257	0.246	0.018	0.228
Pair 21	0.989	0.014	0.975	0.908	0.018	0.890
Pair 22	0.459	0.110	0.349	0.320	0.095	0.225
Pair 23	1.155	0.089	1.066	1.082	0.095	0.987
Pair 24	0.559	0.120	0.439	0.512	0.162	0.350
Pair 25	0.509	0.005	0.504	0.379	0.006	0.373
Pair 26	0.328	0.049	0.279	0.294	0.064	0.230
Pair 27	0.475	0.074	0.401	0.337	0.061	0.276
Pair 28	0.699	0.058	0.641	0.621	0.061	0.560
Pair 29	0.291	0.079	0.212	0.265	0.065	0.200
Pair 30	1.645	0.061	1.584	1.149	0.065	1.084
Pair 31	0.529	0.127	0.402	0.403	0.163	0.240
Pair 32	0.755	0.045	0.710	0.643	0.043	0.600
Pair 33	0.828	0.039	0.789	0.755	0.043	0.712
Pair 34	0.232	0.032	0.200	0.231	0.028	0.202
Pair 35	0.339	0.062	0.277	0.256	0.056	0.200
Pair 36	0.709	0.058	0.651	0.583	0.056	0.526
Total Operating Time	23.766	4.513	19.253	20.193	4.628	15.565

APPENDIX B: Chapter 6 Data and Results

This shows the data and results used for the investigation and work in chapter 6

B.1 IEEE 8-Bus Data and Results

Table B.1: IEEE 8-Bus System: Relay Operating Time from the Three Formulation Approach

Relays	Traditional Formulation $T_{pr}(Sec)$	Modified traditional Formulation $T_{pr}(Sec)$	Proposed Formulation $T_{pr}(Sec)$
R1	0.0773	0.0691	0.0117
R2	0.0942	0.3522	0.2195
R3	0.1162	0.4005	0.0686
R4	0.1455	0.2260	0.0258
R5	0.0753	0.0360	0.1232
R6	0.1091	0.2317	0.1790
R7	0.0348	0.0782	0.1130
R8	0.1394	0.0072	0.0014
R9	0.0791	0.0424	0.0652
R10	0.0032	0.1261	0.0011
R11	0.0778	0.0010	0.0431
R12	0.1601	0.0031	0.1342
R13	0.0602	0.1332	0.0597
R14	0.0342	0.3776	0.1577
Total operating time	1.2065	2.0844	1.2034

B.2 IEEE 33-Bus Data and Results

Table B.2: Modified IEEE 33-Bus Relay: Fault Current Characteristics Considering Adjacent Breaker Status

Pair	Closed Adjacent breaker		Opened Adjacent breaker	
	Primary Fault Current (A)	Backup Fault Current (A)	Primary Fault Current (A)	Backup Fault Current (A)
1	70578.13	70578.13	70590.13	70590.13
2	70578.13	265	70590.13	304
3	454	250	1076.5	366
4	454	207	1076.5	724
5	11267	10986	11600.5	11555.45
6	11267	384	11600.5	666.3
7	725	727	1413	6290
8	725	727	1413	790
9	3406	2603.75	3640	2665
10	3406	822.76	3640	990
11	1197.32	813.02	1462	844
12	1197.32	285.89	1462	620.4
13	3096	1064	3399.9	1272.2
14	3096	2048.52	3399.9	2144.61
15	675.81	398.22	1151	711.26
16	675.81	283.2	1151	446.9
17	2235	439.34	2680	689
18	2235	1805.68	2680	1928.1
19	664.17	26.31	1295	549.4
Continued on next page				

Table B.2 – continued from previous page

Pair	Closed Adjacent breaker		Opened Adjacent breaker	
	Primary Fault Current (A)	Backup Fault Current (A)	Primary Fault Current (A)	Backup Fault Current (A)
20	664.17	658.92	1295	749.2
21	2020.19	1067.56	2294	1336
22	2020.19	974.1	2294	1004
23	502.27	76.09	972	630
24	502.27	432.1	953	352.07
25	1601.97	680.03	1713	718
26	1601.97	925.12	1713	992
27	649.7	567.88	1600	1428
28	11602	696.64	11758	881
29	11602	10986.08	11758	11759.92
30	383	386	1012	1018
31	1941	1950	2115	2123
32	1585	972	2030	1375
33	1585	441	2030	576
34	3772	2603.63	4044.11	2945
35	3772	1196.44	4044.11	1334.7
36	824	718.75	1201	839
37	824	102	1201	320.4
38	3005	1569	3140	1593
39	3005	1228.23	3140	1333
40	549	384	713	5740
Continued on next page				

Table B.2 – continued from previous page

Pair	Closed Adjacent breaker		Opened Adjacent breaker	
	Primary Fault Current (A)	Backup Fault Current (A)	Primary Fault Current (A)	Backup Fault Current (A)
41	1322.37	681	1678.97	989
42	1322.37	648.3	1678.97	697
43	925.21	1026	1324	903.68
44	925.21	398.22	1324	422.8
45	70878	70578.27	71122	70578
46	70878	321	71122	710
47	169.61	169.61	999.2	297
48	169.61	169.61	999.2	593
49	3315	2408.17	3870	2421
50	3315	968.54	3870	1191
51	490	283.99	896	627
52	490	215.3	896	282.2
53	3230	2408.17	3405	2435
54	3230	491	3405	781
55	969	1184.99	3038	2085
56	969	285.89	3038	949.4

Table B.3: Modified IEEE 33-Bus Relay: Coordination Time Interval from the Three Formulation Approach

Pair	Traditional Formulation CTI (Sec)	Modified Traditional Formulation CTI (Sec)	Proposed Formulation CTI (Sec)
1	0.194	0.297	0.251
2	0.152	0.564	0.213
3	0.110	0.483	0.202
4	0.183	0.537	0.215
5	0.160	0.430	0.24
6	0.201	0.447	0.202
7	0.139	0.330	0.2
8	0.141	0.487	0.2
9	0.235	0.363	0.242
10	0.192	0.499	0.21
11	0.135	0.227	0.2
12	0.123	0.304	0.2
13	0.134	0.470	0.21
14	0.187	0.354	0.24
15	0.141	0.380	0.22
16	0.151	0.341	0.21
17	0.196	0.356	0.2
18	0.193	0.618	0.26
19	0.156	0.253	0.201
20	0.196	0.378	0.204
Continued on next page			

Table B.3 – continued from previous page

Pair	Traditional Formulation CTI (Sec)	Modified Traditional Formulation CTI (Sec)	Proposed Formulation CTI (Sec)
21	0.199	0.474	0.235
22	0.168	0.510	0.23
23	0.131	0.254	0.221
24	0.184	0.316	0.21
25	0.139	0.255	0.218
26	0.190	0.247	0.221
27	0.159	0.320	0.2
28	0.173	0.252	0.2
29	0.172	0.283	0.25
30	0.125	0.371	0.2
31	0.129	0.408	0.2
32	0.226	0.594	0.23
33	0.182	0.327	0.207
34	0.189	0.284	0.25
35	0.192	0.615	0.238
36	0.189	0.363	0.221
37	0.206	0.235	0.21
38	0.143	0.371	0.217
39	0.162	0.312	0.206
40	0.145	0.543	0.2
41	0.217	0.465	0.291
Continued on next page			

Table B.3 – continued from previous page

Pair	Traditional Formulation CTI (Sec)	Modified Traditional Formulation CTI (Sec)	Proposed Formulation CTI (Sec)
42	0.140	0.429	0.214
43	0.185	0.329	0.223
44	0.147	0.214	0.203
45	0.261	0.266	0.264
46	0.144	0.285	0.219
47	0.147	0.499	0.201
48	0.159	0.231	0.2081
49	0.212	0.326	0.243
50	0.203	0.414	0.212
51	0.217	0.371	0.246
52	0.218	0.357	0.221
53	0.242	0.534	0.245
54	0.196	0.484	0.208
55	0.154	0.425	0.243
56	0.203	0.568	0.271
Total CTI	9.771	21.647	12.3961

Table B.4: Modified IEEE 33-Bus Relay: Relay Operating Time from the Three Formulation Approach

Relays	Traditional Formulation $T_{pr}(Sec)$	Modified traditional Formulation $T_{pr}(Sec)$	Proposed Formulation $T_{pr}(Sec)$
F2	0.087	0.088	0.045
F3	0.158	0.158	0.166
F6	0.040	0.088	0.033
F8	0.300	0.305	0.291
F9	0.093	0.093	0.099
F12	0.028	0.102	0.027
F15	0.314	0.395	0.324
F21	0.236	0.373	0.314
F22	0.215	0.278	0.183
F25	0.009	0.009	0.008
F29	0.120	0.120	0.039
F33	0.312	0.324	0.299
R3	0.042	0.082	0.023
R6	0.083	0.241	0.160
R8	0.013	0.013	0.005
R9	0.014	0.051	0.023
R12	0.234	0.245	0.163
R15	0.197	0.201	0.116
R21	0.034	0.034	0.061
R25	0.105	0.230	0.146
R29	0.108	0.158	0.052
R33	0.047	0.208	0.149
F21B	0.238	0.353	0.299
F15B	0.083	0.114	0.016
F9B	0.063	0.160	0.115
F29B	0.266	0.381	0.206
F3B	0.077	0.245	0.197
F6B	0.044	0.046	0.097
F8B	0.078	0.241	0.204
F2B	0.006	0.013	0.076
F12B	0.249	0.344	0.237
Total Operating Time	3.894	5.696	4.175

APPENDIX C: Chapter 7 Data and Results

This shows the data and results used for the investigation and work in chapter 7

Table C.1: IEEE 14-bus system: Total Operating Time of Each Clustering Approach

Relay	Operating Time (Sec)		
	Approach 1	Approach 2	Approach 3
R1_2	1.43	1.32	1.78
R1_5	3	2.87	3.15
R2_1	4.42	4.76	4.29
R2_5	2.24	2.12	2.34
R2_4	1.91	1.83	2.1
R2_3	2.28	2.29	2.4
R5_1	0.38	0.32	0.58
R5_2	0.86	0.7	0.98
R5_4	2.91	2.73	2.9
R5_6	1.47	1.41	1.56
R3_2	0.65	0.68	0.85
R3_4	0.62	0.61	0.83
R4_2	0.68	0.67	1.11
R4_3	0.87	0.67	1.15
R4_5	1.27	1.1	1.43
R4_7	0.83	0.76	0.93
R4_9	1.04	0.95	1.01
R7_4	1.52	1.16	1.62
Continued on next page			

Table C.1 – continued from previous page

Relay	Operating Time (Sec)		
	Approach 1	Approach 2	Approach 3
R7_8	0.73	0.57	0.86
R7_9	0.86	0.76	0.98
R6_5	0.79	0.73	1.08
R6_11	0.66	0.6	0.84
R6_12	0.35	0.23	0.45
R6_13	0.37	0.29	0.48
R9_4	0.36	0.2	0.4
R9_7	1.25	1.19	1.43
R9_10	0.3	0.25	0.51
R9_14	0.44	0.39	0.6
R10_9	0.95	0.91	1.05
R10_11	0.34	0.21	0.53
R11_6	0.46	0.4	0.66
R11_10	0.85	0.7	0.86
R14_9	0.71	0.58	0.97
R14_13	0.57	0.41	0.55
R12_6	0.47	0.35	0.52
R12_13	0.28	0.19	0.29
R13_12	0.35	0.31	0.38
R13_14	0.32	0.22	0.45
R13_6	0.85	0.74	0.97
Total Operating Time	41.51	37.91	46.85

Table C.2: IEEE 33-bus system: Total Operating Time of Each Clustering

Relay	Clustering Approach 1 (Sec)	Clustering Approach 2 (Sec)	Clustering Approach 3 (Sec)
F2	1.58	1.39	1.41
F3	1.3	1.52	1.52
F6	1.83	1.74	2.86
F8	2.18	1.65	1.92
F9	1.7	1.12	1.64
F12	2.38	2.49	1.7
F15	2.02	2.31	2.2
F21	1.34	1.49	1.9
F22	3.63	2.92	2.14
F25	2.3	1.86	2.95
F29	1.51	1.29	1.69
F33	1.63	1.98	1.69
R3	2.79	1.93	1.78
R6	2.13	1.63	1.69
R8	3.01	2.41	2.48
R9	2.5	3.41	3.54
R12	3.72	2.12	3.59
R15	3.44	1.92	2.32
R21	1.29	1.31	2.9
R25	2.71	3.12	4.96
R29	1.84	1.76	2.19
R33	1.99	1.99	1.61
F21B	1.92	1.78	2.03
F15B	1.34	1.75	2.22
F9B	1.49	1.65	1.62
F29B	1.63	1.59	1.55
F3B	1.71	1.62	1.34
F6B	1.61	1.87	1.39
F8B	1.24	1.01	1.44
F2B	1.09	1.56	1.29
F12B	1.75	2.19	2.54
Total Operating Time	62.6	58.37	66.11